NTNU – Trondheim
Norwegian University of
Science and Technology

Impact Loads on Circular Cylinders

Espen Larsen

Marine Technology
Submission date: June 2013
Supervisor: Sverre Steen, IMT

Norwegian University of Science and Technology
Department of Marine Technology

Abstract

In the past, testing of water impact problems such as breaking waves impacting on risers, lowering of subsea structures through the splash zone and free-fall lifeboat performance has been carried out either by model tests or simplified methods such as empirical formulas and potential flow calculations. The simplified methods generally give reasonable results for simple geometries such as wedges or two-dimensional cylinders. Model tests are required when more complex structures are to be analyzed, increasing the cost and time spent significantly. In addition, scale effects may also alter the results.

Recent advances in computer technology and computational fluid dynamics (CFD) have made it possible to simulate many of the problems that earlier only could be studied using model tests. This allows for more tests being performed at a lower cost compared to model tests and with higher accuracy than simplified methods. In addition, the CFD simulations are normally performed in full scale, avoiding scale effects.

This thesis explores the possibility of simulating water entry problems using the CD-adapco CFD-software STAR-CCM+ with focus on circular cylinders. The reason for choosing this shape is that it is a simple geometry while still being a realistic problem, since this is the most widely used shape for structural members in the offshore industry. Also, for numerical methods the initial phase of impact of a cylinder is numerically difficult to solve, because of the almost flat surface on the cylinder bottom. This means that a method solving water impact of cylinders correctly is believed to also simulate water entry of other geometries satisfactory.

Two-dimensional simulations have been performed for constant velocity and free-falling cylinders. Good agreement is found between the CFD results and empirical lines by Campbell and Weynberg (1980). The results for free-falling cylinders show fairly good agreement with experimental data by Greenhow and Lin (1983), nonlinear boundary element method results by Sun (2007), and CFD simulations by Zhu (2006).

Three-dimensional simulations have been performed to analyze the water impact of a cylinder with 8° impact angle assuming constant velocity. The results are compared to experiments performed by Campbell and Weynberg (1980) and strip theory calculations. Good agreement is found between the methods.

Sammendrag

Frem til nå har beregning av slagaktige påkjenninger som fremkommer ved for eksempel brytende bølger som treffer stigerør, nedsenkning av undervannsinnstalasjoner gjennom havoverflaten og når fritt-fall livbåter treffer vannoverflaten vært basert på enten modelltester eller forenklede metoder slik som empiriske formler og numeriske modeller basert på potensialteori. Disse forenklede metodene gir oftest gode resultater for enkle geometrier slik som kiler og todimensjonale sylindere, mens for mer komplekse konstruksjoner må man benytte modelltester for å få pålitelige resultater. Dette medfører en betydelig økning i kostnadene, og i tillegg kan resultatene være påvirket av ukjente skaleringseffekter, siden fullskala testing vanligvis ikke er mulig å gjennomføre.

Den senere tiden har utviklingen innen datateknikk og *computational fluid dynamics* (CFD) gjort det mulig å simulere mange av problemene som tidligere bare kunne studeres ved hjelp av modelltesting. Dette gjør det mulig å gjennomføre beregningene til en lavere kostnad og på kortere tid enn modelltester, og med høyere nøyaktighet enn de forenklede metodene nevnt ovenfor. I tillegg har CFD fordelen av at man kan gjøre simuleringer i fullskala, og dermed utelukke skaleringseffekter.

Denne oppgaven undersøker mulighetene til å simulere en sylinder som treffer en fri overflate med høy hastighet ved hjelp av CFD-programmet STAR-CCM+ utviklet av CD-adapco. Grunnen til at den sylindriske formen er valgt er at dette er en enkel geometri, som likevel er svært relevant siden dette er den mest brukte geometrien i offshore-industrien. I tillegg er den første fasen etter sylinderen treffer vannflaten vanskelig å simulere for alle numeriske metoder siden sylinderen er tilnærmet flat på bunnen. Dette medfører at en metode som viser seg å gi gode resultater for en sylinder også forventes å kunne benyttes for andre geometrier.

Todimensjonale simuleringer har blitt utført for både konstant hastighet og sylinder som faller fritt, og resultatene stemmer bra med en veletablert emprisisk formel presentert av Campbell and Weynberg (1980). Resultatene for sylinder i fritt fall stemmer relativt bra overens med numeriske resultater presentert av Zhu (2006) og Sun (2007) og eksperimentelle data av Greenhow and Lin (1983)..

Tredimensjonale simuleringer har blitt gjennomført for en sylinder som treffer vannflaten med en vinkel på 8° og konstant hastighet. Resultatene er sammenlignet med resultater publisert av Campbell and Weynberg (1980), og samsvarer bra med både eksperimentelle data og stripeteori.

NTNU Trondheim
Norwegian University of Science and Technology
Faculty of Engineering Science and Technology
Department of MarineTechnology

M.Sc. thesis 2013

for

Espen Larsen

Impact loads on circular cylinders

Offshore structures are often composed of circular cylinders, in addition comes risers and pipelines. When such structures are lowered through the water surface, or are located close to a wavy ocean surface, impact loads might occur. It is in some cases important to be able to quantify those loads. The aim of the master thesis is to explore the potential of CFD with VOF-type free surface treatment to predict impact loads on circular cylinders.
The following topics should be covered in the thesis:

1. Do a literature survey to establish state of knowledge regarding impact loads on circular cylinders.
2. Based on the literature search, establish a benchmark data set for impact loads on a circular 2-D section.
3. Use Star CCM+ or equivalent software to compute the impact loads on the circular section, and compare with the benchmark data. Improve the calculation until satisfactory agreement is found. Perform grid convergence studies and similar standard quality checks of the CFD model.

From this stage, the thesis might follow different roads, either to explore hydroelastic effects, or to consider 3-D shapes, such a cylinder impacting on a flat free surface with a small angle, or waves hitting a circular cylinder fixed slightly above the calm water level.

The candidate should in his report give a personal contribution to the solution of the problem formulated in this text. All assumptions and conclusions must be supported by mathematical models and/or references to physical effects in a logical manner.
The candidate should apply all available sources to find relevant literature and information on the actual problem.

The report should be well organised and give a clear presentation of the work and all conclusions. It is important that the text is well written and that tables and figures are used to support the verbal presentation. The report should be complete, but still as short as possible.

The final report must contain this text, an acknowledgement, summary, main body, conclusions, suggestions for further work, symbol list, references and appendices. All figures, tables and equations must be identified by numbers. References should be given by author and year in the text, and presented alphabetically in the reference list. The report must be submitted in two copies unless otherwise has been agreed with the supervisor.

The supervisor may require that the candidate should give a written plan that describes the progress of the work after having received this text. The plan may contain a table of content for the report and also assumed use of computer resources.

From the report it should be possible to identify the work carried out by the candidate and what has been found in the available literature. It is important to give references to the original source for theories and experimental results.

The report must be signed by the candidate, include this text, appear as a paperback, and - if needed - have a separate enclosure (binder, diskette or CD-ROM) with additional material.

Supervisor : Professor Sverre Steen
Start : 14.01.2013
Deadline : 10.06.2013

Trondheim, 10.01.2013

Sverre Steen
Supervisor

Acknowledgments

This thesis is the result of the individual work performed during the spring semester 2013 for fulfillment of the degree Master of Science, Marine Technology, with specialization in marine hydrodynamics. The work has been performed at the Norwegian University of Science and Technology (NTNU), Department of Marine Technology, with Professor Sverre Steen as supervisor.

I would like to thank my supervisor Professor Sverre Steen for both inspiring me and keeping on the topic. I would also like to thank Professor Odd M. Faltinsen for sharing of his knowledge about water impact loads. I also acknowledge the help from Professor Bjørnar Pettersen, who arranged access to the Vilje HPC cluster at NTNU.

Next, I would like to thank Michael Glockenmeier at CD-adapco for providing license to STAR-CCM+ and granting me online training in the software. Also Dr. Charalampos "Babis" Tsimis at CD-adapco deserves a thank you for many valuable discussions regarding the use of STAR-CCM+ and the model setup.

Last, but not least, I would like to thank my fellow students for all the good memories and valuable discussions during my years at NTNU, and my family for always supporting me in the choices I make.

Espen Larsen

Trondheim, June 4, 2013

Contents

List of Figures

List of Tables

List of Symbols

Δx	Grid spacing in x-direction
Δy	Grid spacing in y-direction
Δz	Grid spacing in z-direction
Δt	Time step size
$\mathbf{b}$	Body forces vector (per unit mass)
$\mathbf{n}$	Surface normal vector
$\mathbf{v}$	Velocity vector
α	Volume fraction scalar
Γ	Diffusivity coefficient
ϕ	Velocity potential
ρ	Fluid density
ζ	Free surface elevation
C	Speed of sound in water
$c(t)$	Half-width of equivalent plate
C_p	Pressure coefficient
C_s	Slamming coefficient
$C_{S,B}$	Buoyancy contribution to slamming coefficient
$C_{s\theta}$	Inclined slamming coefficient
F_3	Vertical hydrodynamic force
F_N	Froude number
h	Non-dimensional submergence
p	Pressure
p_{ac}	Acoustic pressure

R	Radius of cylinder
T	Temperature
t	Time variable
t_*	Duration of phase with supersonic velocities
V	Vertical velocity of cylinder
b_ϕ	Sink/source strength
G	Grid flux due to mesh motion
L	Length of cylinder

List of Abbreviations

CFD	Computational fluid dynamics
CFL	Courant–Friedrich–Levi
CIP	Constrained Interpolation Profile
CV	Control volume
DBFI	Dynamic fluid-body interaction
DNS	Direct Numerical Simulation
FD	Finite Difference
FE	Finite Element
FVM	Finite Volume Method
HB	Half buoyant
HPC	High performance computing
HRIC	High-Resolution Interface Capturing
LES	Large Eddy Simulation
MDRT	Mesh Displacement in Real Time
NB	Neutrally buoyant
NTNU	Norwegian University of Science and Technology
PDE	Partial differential equation
RANS	Reynolds Averaged Navier–Stokes
SIMPLE	Semi-Implicit Method for Pressure-Linked Equations
SPH	Smoothed Particle Hydrodynamics
UD	Upwind Differencing
VOF	Volume-of-Fluid

1 Introduction and Motivation

With the rapid decrease in cost of computational power combined with more efficient numerical codes, Computational Fluid Dynamics (CFD) has gone from being a specialized tool for the aviation industry to a widely used tool in many industries. The use of CFD to calculate hydrodynamic loads on offshore installations, ships, and other bodies in the ocean is increasing rapidly at the moment, resulting in shorter lead times and more opportunities for testing during design compared to model tests. In addition to allowing for more tests to be performed at a lower cost than model testing, scale effects are normally avoided in CFD simulations.

The water impact problem is of large interest in the offshore and ship design industries, and many have studied the slamming loads on ship hulls, impact loads for free-fall lifeboats etc. Common for these analyses is the need for an accurate prediction of loads of a relatively short duration, typically less than 0.1 s. Although of short duration, these loads have resulted in structural damage on structures ranging from heave compensator systems for drilling risers (Sten, 2012) to free-fall lifeboats (Johannessen, 2012), and the more well-known problem of bow and stern damage on ships due to slamming. The loads are also of great interest when it comes to installation of structures such as subsea templates, during the phase when the structure is lowered through the water surface.

Traditionally, these loads have been calculated based on strip theory and simple equations. However, the methods in use at the moment are not always suitable for the given problem, especially if the geometry is complex or the water flow is not governed by potential theory. One example of this is the violent behavior of breaking waves impacting on an array of riser guide tubes. Also, most numerical and traditional methods are only validated for wedges, whereas cylinders are the most commonly used structural members in the offshore industry.

The most widely used solution method for water impact loads on circular cylinders at the moment is an empirical formula combined with strip theory. (DNV, 2010). The main drawback of this formula is that it is based on two-dimensional impact on a flat free surface, neglecting three-dimensional (3D) effects. This is believed to result in too high load values, especially for steep waves interacting with vertical cylinders (Larsen, 2012).

This thesis explores the possibility of using the CFD-software STAR-CCM+ developed by CD-adapco for calculating water impact loads as discussed above. Johannessen (2012) showed good agreement with theory for the case of wedges impacting on a flat free surface. His work is of great practical interest for free-

fall lifeboats where the governing geometrical shape for the impact is a wedge. However, it is believed that the use of CFD to calculate loads on circular members is of more practical interest to the offshore industry. In addition, circular cylinders can often be considered the ultimate test for water impact testing, as the angle between the cylinder surface and water surface changes with time. During the initial phase, when the angle is small this causes problems due to singularities, rapidly increasing wetted surface and large pressure peaks.

For wedges several validated methods that are easier to apply than CFD are available, but the methods available for circular cylinders are considered less accurate, especially for complex structures. It is believed that if STAR-CCM+ provides good results on this test case, the water impact of more complex structures can be simulated with good accuracy.

In chapter 2, a review is given over traditional methods of water impact calculation, both analytical and numerical techniques are discussed. A review of experimental work on the area and difficulties regarding experimental testing is given in chapter 3 before an introduction to CFD is presented in chapter 4. The general principles of CFD are treated before the more specialized topics for STAR-CCM+ are discussed.

The constant velocity impact of a two-dimensional (2D) circular cylinder on a flat free surface is simulated in chapter 5 where the process of determining a correct model setup has been discussed. Choice of domain size, mesh, time steps, numerical parameters, and differences between laminar and turbulent flow model is discussed. Simulations have been performed on relatively coarse mesh applicable for the industry, and also very fine mesh which is more of academic interest due to the high computational cost.

Based on the results from chapter 5, free fall drop test of two different cylinders have been simulated in chapter 6. The results are compared to experimental results and other numerical methods.

Chapter 7 covers a three-dimensional (3D) analysis of a circular cylinder impacting at an angle with constant velocity. Results are compared to experimental results by Campbell and Weynberg (1980) and strip theory.

It is assumed that the reader possess some basic understanding of fluid dynamics but specialized knowledge is not required.

2 Analytical and numerical methods

Water impact loads have for many years been of great interest to engineers and scientists, and much knowledge has been gained since the pioneering work of von Karman (1929), who investigated loads on seaplane floats shaped as wedges during water entry.

Traditionally, wedges have been more studied than circular cylinders. The main reason for this is that it is more difficult to determine impact loads on circular cylinders compared to wedges. The main difficulty is that the cylinder has zero deadrise angle at the instant of water impact, with increasing deadrise angle as submergence increases. The result is that it is very difficult to obtain reliable results for validation, compared to when wedges are used. In addition, the flat bottom of the cylinder introduces a numerical singularity for numerical methods. The result is that numerical methods are normally only applicable for a deadrise angle $> 4°$, and should therefore not be used for the initial phase of impact for a cylinder.

Although wedges are not the focus of this thesis, basic knowledge of water impact of wedge shaped bodies is important, as these are the starting point for most methods for circular cylinders. It has been a general trend that theories first have been developed for 2D wedges, then extended to 2D and 3D arbitrary shapes. Some information about water entry of wedges is therefore included, to gain a full understanding of the theories available.

A complete review of all proposed methods is beyond the scope of this thesis, but an introduction to the most common models is presented in this chapter. Common for all methods presented is that compressibility effects, gravity, and air pockets are neglected. Also, all the mentioned methods have been applied for circular cylinders, with mixed results.

2.1 Coefficients

Before starting to compare different impact load calculation methods, some coefficients have to be defined. First we define the slamming coefficient, which is the non-dimensional impact force;

$$C_s(t) = \frac{F_3(t)}{\rho V^2 R} \tag{2.1}$$

Here F_3 is the vertical hydrodynamic force, ρ the water density, V the relative velocity between the cylinder water surface and R is the radius of the cylinder.

This slamming coefficient is based on the hypothesis that the slamming load is proportional to the diameter of the cylinder, the velocity squared and the density of water. This assumption has been proven to be a good fit, see e.g. Hagiwara and Yuhara (1976). For studying the pressure on the body surface, the pressure coefficient, C_p can be used:

$$C_p(x,t) = \frac{p(x,t)}{0.5\rho V^2} \tag{2.2}$$

Where $p(x,t)$ is the pressure at position x and time t.

2.2 Von Karman and Wagner

The pioneering work by von Karman (1929) was based on the important assumption that the momentum of the water/body system is conserved. This means that the force can be calculated based on the change in added mass of the body. Calculation of added mass depends heavily on the free surface and body boundary conditions, and accurate values were not available. Von Karman therefore used the high-frequency limit for a flat plate of width $2c(t)$, where $c(t)$ is the distance from the center-line of the wedge to the intersection line with the free surface, assumed to be at the undisturbed free surface.

This flat-plate simplification is believed to be a good approximation when the submergence is infinitesimally small, i.e. $t \ll 1$.

Although von Karman's solution only provided a rough estimate for the water impact loads, his theory is considered the starting point for impact load calculations, and has later been extended and refined by several authors.Wagner (1932) continued the work by von Karman, and took into account the uprise of water along the side of the body, resulting in a larger half-width of the plate for the added mass estimation than calculated by von Karman.

The von Karman method has later been proven by other theories and experiments to give too low impact load coefficients for both wedges and cylinders. The Wagner method, on the other hand, is believed to give too large load predictions.

Although von Karman and Wagner based their theories on 2D wedges, the theories are also applicable to circular cross-sections for a small submergence. For a circular cylinder, a simple geometric consideration will show that the half-width for von Karman's method is:

$$x^2 + (R - Vt)^2 = c^2 + (R - Vt)^2 = R^2 \rightarrow c(t) = \sqrt{2VtR - (Vt)^2} \tag{2.3}$$

For the Wagner method, the instantaneous free surface elevation η_b has to be taken into account, which for constant V gives $c(t) \approx \sqrt{VtR}$ (Larsen, 2012). This means that $c(t)$ is larger for the Wagner method than the von Karman method by approximately a factor $\sqrt{2}$ for small t. The impact force is then found by integrating the pressure over the wetted surface, using a linearized Bernoulli equation, where the velocity-squared term and hydrostatic pressure is neglected:

$$p \approx -\rho \frac{\partial \phi}{\partial t} = \rho V \frac{c}{\sqrt{c(t)^2 - x^2}} \frac{dc}{dt} \tag{2.4}$$

It can be shown (Larsen, 2012) that the initial slamming coefficients are:

Method	$C_{s,initial}$
von Karman	π
Wagner	2π

Table 2.1: Initial slamming coefficients for von Karman and Wagner methods

For the von Karman and Wagner approaches, we have

$$C_p(t) = \frac{p(t)}{0.5\rho V^2} \cong \frac{c}{2V\sqrt{c^2 - x^2}} \frac{dc}{dt} \tag{2.5}$$

and inserting the plate width from Wagner's method yields

$$C_p(t) = \frac{4}{\sqrt{4(Vt/R) - (x/R)^2}} \quad \text{for } |x| < c(t) = 2\sqrt{VtR} \tag{2.6}$$

We see that the pressure coefficient $C_p \rightarrow \infty$ for $x \rightarrow c(t) = 2\sqrt{VtR}$ This is because the potential flow solution associated with with the Wagner method does not include the flow detail developing a jet in the spray-root zone.

The Wagner model is as mentioned above only applicable for a very short time after impact ($t \ll 1$), but Campbell et al. (1977) integrated the pressure distribution from the Wagner model over a plate, and derived the following expression for the slamming coefficient for varying cylinder submergence:

$$C_s = \frac{2\pi}{1 + 1.5Vt/R} \tag{2.7}$$

It should be noted that the accuracy of this slamming coefficient is considered low.

2.3 Generalized Wagner

The generalized Wagner approach is an important group of semi-analytical impact models, where only the free surface boundary condition is linearized, whereas the exact body boundary condition is satisfied (i.e. no flat-plate approximation). The full nonlinear Bernoulli equation is used and the main improvement of this method compared to the original Wagner method is that it allows for larger deadrise angles. Generalized Wagner was first developed for wedges, and later extended to include cylinders and other shapes.

Zhao et al. (1996) used this approach in a numerical solution of the problem using the boundary element method (BEM) solving Green's second identity for each time step. Pile-up of water is treated the same way as by Wagner (1932), and the main difference from the Wagner approach is that the body boundary condition is exact at each time instant. The dynamic free surface boundary condition is $\phi = 0$ on $z = \zeta(t)$, where ϕ is the velocity potential and $\zeta(t)$ is a horizontal line at the same height as the intersection point, see figure 2.1. Once the velocity potential is known, the pressure on the body surface can be calculated using the Bernoulli equation. Special care has to be taken close to $x = c(t)$ as the method will estimate negative and unbounded pressure, since the velocity is infinite here. Zhao et al. (1996) solved this by setting the pressure in regions with negative pressure equal to the atmospheric pressure. Later, this model has been extended to arbitrary three-dimensional bodies by Faltinsen and Chezhian (2005), who studied the water impact of a three-dimensional cylinder with spherical end sections using this method.

Mei et al. (1999) modified the method by Zhao to analytically estimate slamming forces on various bodies using conformal mapping of the flow domain onto a half-plane. The results by Mei et al. (1999) differs from those of Zhao et al.

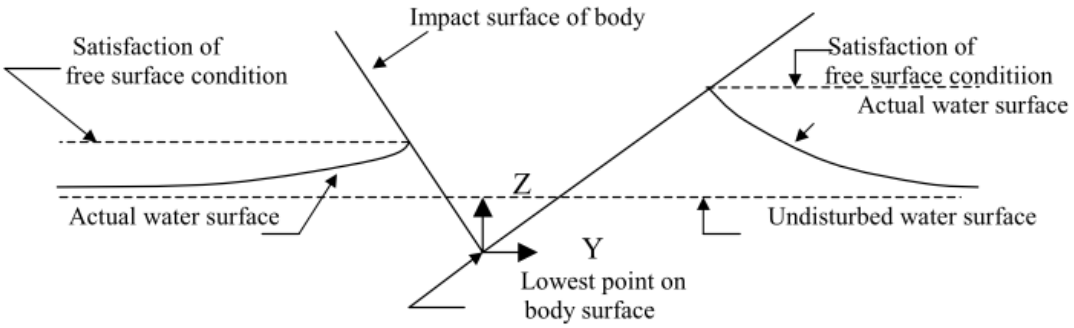

Figure 2.1: How the elevation of the surface due to impact is represented in the generalized Wagner solution. Here illustrated using a wedge, but also valid for circular cross sections (MARINTEK, 2004)

(1996) by predicting lower impact force for wedges with deadrise angle less than 20°. This is believed to be due to the fact that Mei et al. (1999) integrated the pressure over the entire wetted surface, including the region of negative pressure without further treatment of this area. It should be noted that the method by Mei et al. (1999) is developed for wedges and the applicability to cylinders is not known.

Another approach was presented by Vorus (1996), who imposed a nonlinear boundary condition on the initial level of the water surface and linearized the body boundary condition. As for the method by Zhao et al. (1996), the nonlinear Bernoulli equation is used for pressure calculations on the body. The three-phase intersection points between air, body and water is determined based on the assumption that the hydrodynamic pressure in these points have to be equal to the atmospheric pressure.

Slam2d The MARINTEK-software Slam2d is an example of practical use of the Generalized Wagner method, and is based on the generalized Wagner approach as presented by Zhao et al. (1996). Slam2d can perform calculations on 2D geometries with time-varying relative vertical, horizontal and rotational velocities between the section and the water surface. The program has the following limitations:

- Horizontal and rotational velocities are assumed small compared to vertical velocity.
- It is not recommended to use the program for sections where the local dead-

rise angle is less than 3°. For cylinders, this means that the program should not be used for the initial phase of impact, hence the simulation should be started with an initial submergence.

- The local deadrise angle should be less than 79° for all elements. The section(s) geometry is modified automatically by the software to meet this requirement.

The body is divided into 50 elements for the BEM solution regardless of the size and shape.

In addition to total force in horizontal and vertical direction, moment, average pressure, pressure coefficients on user-defined panels and pressure distribution on the entire section can be found. Figure 2.2 shows an example of the time-varying pressure on three panels on a cylindrical section.

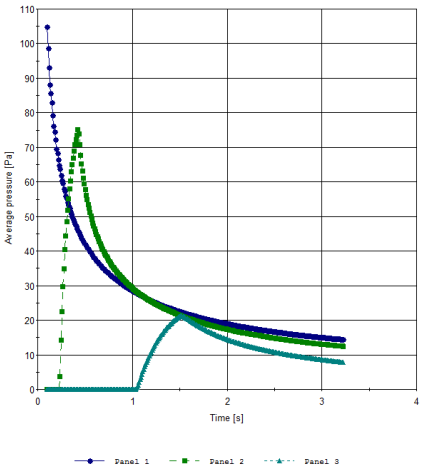

Figure 2.2: Example of time-varying average pressure on three panels on cylindrical section calculated by Slam2D (R=1, $\Delta t = 0.01s$, $V = 0.1m/s$)

2.4 Asymptotic Models

Logvinovich (1969) presented an important example of a series of models based on the idea of improving the Wagner solution by adding some extra terms in the velocity potential in order to make the flow velocity close to $x = c(t)$ finite. These models are known as asymptotic methods, as the extra velocity terms are determined from a local asymptotic analysis close to $x = c(t)$. Logvinovich also argued that the nonlinear Bernoulli equation should be used, but only in the areas

where the equation gives positive pressure. The model has been shown (Korobkin, 2004) to provide a good fit to experimental results by Arman and Cointe (1987) for a circular cylinder for submergence $Vt/R < 0.2$. Equation (2.8) defines the slamming coefficient for this method for a circular cylinder.

$$C_s = 2\pi[1 - \frac{1}{\pi}\sqrt{Vt/R}(1 + \ln(\frac{4}{\sqrt{Vt/R}})] \tag{2.8}$$

It should be noted that the Logvinovich model should only be used for small deadrise angles, hence it is only valid for the initial phase of impact.

Arman and Cointe (1987) presented another important asymptotic model, in which the total impact force for a cylinder differs from the classical Wagner solution by addition of an corrective term, leading to an approximate second order solution. This method is also designed for use during the initial phase of impact. The slamming coefficient for a circular cylinder using this model is:

$$C_s = 2\pi - \sqrt{Vt/R}[10/3 + 2\log(2) - 2\log(Vt/R)] \tag{2.9}$$

2.5 Nonlinear Boundary Element Methods

Zhao and Faltinsen (1993) presented a nonlinear boundary element method (BEM) for two-dimensional symmetric and asymmetric bodies, respectively. The method was verified by comparison to similarity- and asymptotic solutions for two-dimensional wedges (Zhao and Faltinsen, 1993) and also by comparing numerical results to drop tests of a wedge and a bow flare section. The model was later extended by Zhao et al. (1996) to include flow separation and by Faltinsen and Chezhian (2005) to allow 3D bodies.

A nonlinear boundary element method was also applied by Sun (2007), studying strongly nonlinear wave-body interaction problems, including water entry of a circular cylinder. It should be noted that the BEM is not valid for the initial phase of impact where the local deadrise angle is small, and in this phase Sun (2007) used the Wagner method. The numerical results were compared to experimental results by Greenhow and Lin (1983) with good agreement.

2.6 Constrained Interpolation Profile - CIP

Zhu (2006) applied a two-dimensional Constrained Interpolation Profile (CIP) type CFD method for simulating water entry of cylinders with free vertical motion. Two cylinders with different mass density were analyzed to resemble experiments performed by Greenhow and Lin (1983).

Fairly good agreement was shown between the simulations and model tests, except for one point where the experimental data is clearly larger than the numerical results. However, Greenhow and Lin (1983) put a question mark next to this point in their publication. The free surface deformation is also compared to photographs by Greenhow and Lin (1983) and shows good agreement. It should be mentioned that Zhu (2006) also studied water entry with constant velocity and water exit for both constant velocity and constant force, all with good agreement to experimental data.

2.7 Benchmark for simulations in STAR-CCM+

In this chapter, various methods used for calculating water entry loads on circular cylinders have been discussed, from the basic methods by von Karman and Wagner to advanced CFD simulations by Zhu. Several of the methods have severe limitations, such as the von Karman, Wagner and asymptotic methods (Logvinovich method etc.) being only applicable during the initial phase and BEMs *not* being valid during this initial phase.

The only method presented that is valid for all phases of water entry are the CFD calculations by Zhu (2006). In addition, the results by Sun (2007) are valid by combining the Wagner approach with a BEM, but this is considered less accurate than the results by Zhu (2006). Both of these methods show good agreement with experiments by Greenhow and Lin (1983) presented in chapter 3.

This does not by any means indicate that these methods are perfectly correct, but they are considered the most accurate data available, and combined with experimental data this is believed to form a good benchmark for the CFD simulations to be performed in this thesis.

3 Experimental results

For most theories within hydrodynamics, model testing is needed for validation. In water impact problems, the forces can be found by measuring the force directly, integrating the pressure on the surface of the body, or calculated based on the deceleration of a free falling object during impact. The most widely studied validation case is drop test onto an initially flat free surface.

Many difficulties are encountered when testing water impact of cylinders and other blunt bodies, such as short duration of maximum pressure and force, hydroelastic effects and vibrations of sensors. It has also been proven difficult to perform experiments without influence of either variable velocity or vibrations from the test rig.

Despite of the difficulties in testing water impact of a cylinder, experiments have been performed as a part of several projects during the last 50 years. The motivation is easy to see; a method that proves to be in good agreement with a cylinder is of great interest to the offshore industry because the cylinder is the most widely used structural member in the splash zone for e.g. platform legs.The cylindrical shape is also often used as a representative geometry for ship sections where slamming occurs, such as the bow- and stern areas. Also, a method with good agreement for cylinders is assumed to be valid for other shapes too, whereas a method that is developed and proved for wedges does not necessarily model water impact of cylinders and other shapes well.

3.1 Experiments by Hagiwara and Yuhara (1976)

Hagiwara and Yuhara (1976) studied the water impact of three-dimensional semi-cylindrical bow models in scale 1:3. The tests were carried out for various impact angles: 0°, 5° and 15°, and the model, weighing 10 tons, was dropped from different heights, resulting in impact velocities up to 10 m/s. Pressure was recorded using a total of 9 diaphragm pressure transducers distributed both in radial and in longitudinal direction of the cylindrical shape.

The maximum pressures for 5° and 15° impact angle are very close to the line indicating a pressure coefficient (C_p) of 160 and 44.4, respectively. The results for 0° impact on the other hand show significant scatter. Hagiwara and Yuhara (1976) suggests an initial pressure coefficient of 400 for this case, but the results tend to give a lower pressure coefficient for higher velocities (see figure 3.1). This is believed to be because the pressure for higher velocities is very close to the acoustic pressure, where $p_{ac} = \rho CV$ defines the maximum possible pressure due to compressibility of water. Hagiwara and Yuhara (1976) only considered the local pressure, and no values for the global force or the slamming coefficient are presented. It should also be noted that the measured pressure is the averaged pressure over the transducer (10 mm diameter), indicating that the peak pressure may be somewhat higher.

3.2 Experiments by Sollied (1976)

Faltinsen et al. (1977) presented result by Sollied (1976), who studied horizontal cylinders of diameter 0.275 m, 0.30 m and 0.35 m forced with constant velocity through an initially calm surface using an hydraulic ram positioned over the water surface. The tests indicate a peak slamming coefficients in the range of 4.1 to 6.8 with an average value of 5.3. Faltinsen et al. (1977) states that the uncertainty in the experiments is at least ±10%.

3.3 Experiments by Arhan and Deleuil (1978)

Arhan and Deleuil (1978) presented the results of systematic testing of circular cylinders with diameters 20 cm, 40 cm and 60 cm, and impact velocity in the range 1.40 m/s to 3.88 m/s. A total of 185 drops were performed. Each cylinder was equipped with 5 flush mounted diaphragm pressure sensors with (5.7 mm diameter) and piezoelectric accelerometers. The pressure on the cylinder surface

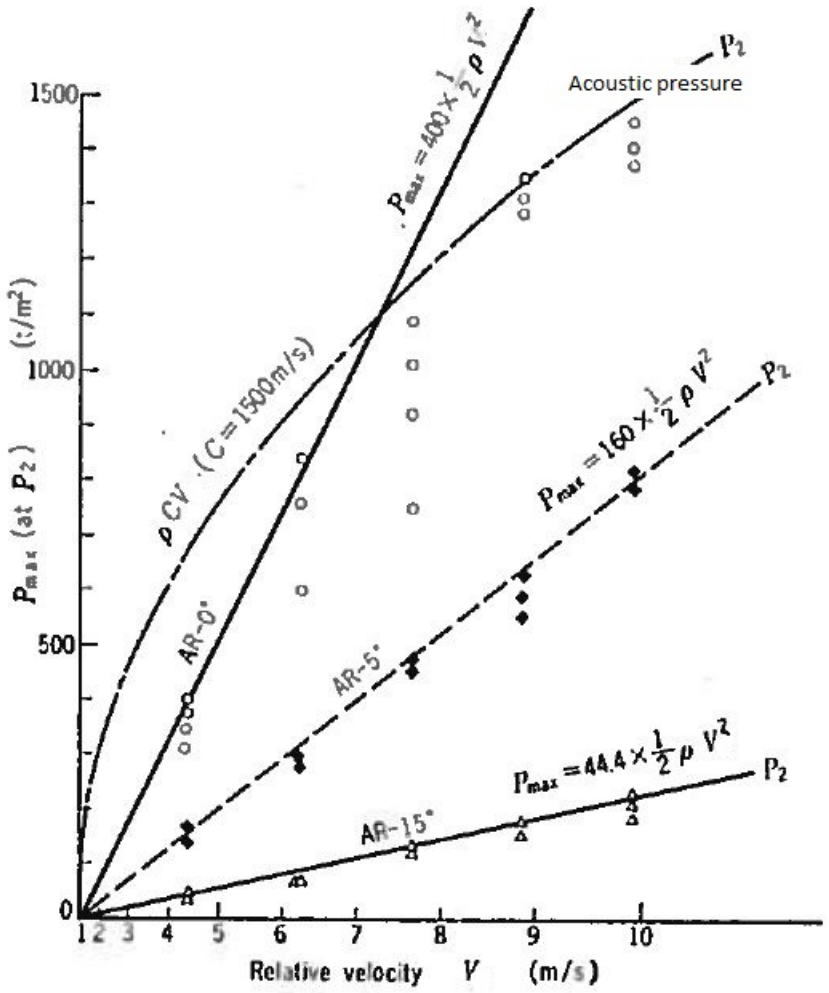

Figure 3.1: Relation between maximum impact pressure p_{max} and relative velocity V_0. AR-0° = 0° impact angle, AR-5° = 5° impact angle. (Hagiwara and Yuhara, 1976)

along with accelerations were recorded and these data were used to estimate the impact forces. Maximum slamming coefficient ranged from 2.40 to 6.90 and the values presented show a relatively large spread for the pressure measurements.

The pressure record for transducers located at 0°, 3° and 6° show that the pressure rise is smoother for the transducer at 0°. Arhan and Deleuil (1978) interprets this as a proof of existence of an air cushion, increasing the pressure at the sensor before it hits the water surface. The data show significant scatter, and the standard deviation of the peak pressure is approximately 30% for the tests.

In general, one should be able to estimate the impact force based on the record from the accelerometer and a simple momentum balance of the system. Arhan and Deleuil (1978) were not able to determine the impact force this way due to vibrations in the accelerometer, and the impact force was instead estimated by assuming a linear variation of the impact force from maximum at the time of impact to zero when half-radius submergence is achieved and conservation of momentum. The velocity is also assumed to be constant during this stage of impact. Although presented as a good model by the authors, it is reasonable to question the validity of this model. A linear variation of the slamming force seems to be a very rough estimate, and may be far from the reality.

3.4 Experiments by Campbell and Weynberg (1980)

Campbell and Weynberg (1980) presented the most cited experiments when it comes to impact loads on circular cylinders. They tested for Froude numbers F_N 1.9 to 5.6 and Reynolds number 0.8 to $4.4 * 10^5$. No correlation was found between varying these parameters and the scatter observed in the recorded data. Both horizontal impact and impact with at an angle (up to 8°) were tested.

Six pressure transducers were distributed in the circumferential direction, at $0°, 6°, 12°, 18°, 24°$ and 30°. The results from these transducer were used to estimate pressure coefficients C_p on the body during impact. A force transducer was also located in the connection between the cylinder and the test rig, measuring the impact force on the cylinder. The data record from this force transducer was used to estimate the slamming coefficient, C_s. The velocity was measured using a velocity transducer on the test rig.

Although small pressure transducers[3.1] were used, Campbell and Weynberg (1980) reported that they were too large to sufficiently resolve the pressure field

[3.1] No quantitative information on the size of the transducers has been found

close to the spray root. The maximum pressure is therfore estimated based on the mean pressure on the transducer once fully wetted.The initial rise of pressure under the cylinder reported by Arhan and Deleuil (1978) is also visible in the tests by Campbell and Weynberg (1980).

Problems with vibration of the test rig were experienced during the testing, with a dominant oscillation at approximately 550 Hz.These known vibrations were filtered from the results. The impact force record for the initial phase of impact was according to Campbell and Weynberg (1980) difficult to use for determining the slamming coefficient. However, integrating the data from the pressure transducers gave results all within the scatter of the force measurements. From the plots in Campbell and Weynberg (1980), the standard deviation is estimated to $\pm 10\%$ for the pressure transducer at the bottom of the cylinder for $Vt/D \geq 0.005$ and less for sensors off the centerline. No quantitative information on the scatter of the force record has been found.

Campbell and Weynberg (1980) fitted a hyperbolic curve with a linear correction to the combination of force record and integrated pressure, resulting in the following slamming coefficient for horizontal impact:

$$C_s = \frac{5.15}{1 + 9.5\mathrm{Vt/R}} + 0.275\mathrm{Vt/R} \tag{3.1}$$

This formula is not corrected for buoyancy and the maximum possible contribution of buoyancy to the vertical force was estimated by Campbell and Weynberg (1980) to be 0.54 for the tests performed with the lowest Froude number. Increasing the Froude number decreases the importance of buoyancy.

The force and pressure measurements for inclined impact show less scatter than the horizontal impact, and the equation above was by Campbell and Weynberg (1980) compared to the data from inclined cylinder using a strip theory approach. The measured results for inclined cylinder are considered more accurate, and the strip theory approach using equation (3.1) compare well with the measurements.

The maximum inclined slamming coefficient $C_{s\theta,\max} = \frac{F_3}{\rho V^2 RL}$ are presented in table 3.1. F_3 is the vertical hydrodynamic force on the cylinder and L is the length of the cylinder.

3.5 Experiments by Greenhow & Lin (1983)

Greenhow and Lin (1983) studied the free surface deformations caused by a cylin-

Impact angle	Max $C_{s\theta}$ from force measurements	Max $C_{s\theta}$ from strip theory
0°	5.15	5.15
1°	2.60	2.55
2°	1.90	1.85
4°	1.30	1.35
6°	1.00	1.15
8°	0.95	1.05

Table 3.1: Maximum slamming coefficients by Campbell and Weynberg (1980)

der dropped into calm water. A half buoyant and a neutrally buoyant cylinder are used in the experiments, where half buoyant means that the weight of the cylinder equals half the buoyancy force on a totally submerged cylinder. The weight of the neutrally buoyant equals the buoyancy force for fully submerged cylinder and the radius of each cylinder is 5.5 cm. The free surface deformation after impact is captured by high-speed cameras, and the penetration depth of the cylinders is plotted as a function of time.

This is a fairly simple, yet effective experiment, with less possible sources of errors compared to other experiments. It should be mentioned that one of the data points presented are questioned by Greenhow and Lin (1983) because the data clearly deviates from the other results.

3.6 Experiments by Miao (1989)

Miao (1989) presented a series of experiments on horizontal impact of cylinders onto a flat free surface at velocities between 0.3 m/s and 2.66 m/s. A cylinder with diameter 0.5 m was used for the pressure measurements, whereas the diameter was 0.125 m for the cylinder used for force measurements.

The time varying pressure was recorded using five flush mounted pressure transducers (diameter 3.56 mm) located at $0°, 2.5°, 5°, 7.5°$ and $10°$. Pressures were recorded for angles up to 30° by rotating the cylinder in 10° increments and repeating the tests. Miao (1989) reported that *"The instrumentation performed entirely satisfactorily, yielding excellent data on the time histories of pressure, phase and displacement"*.

The scatter in the peak pressure was reported to be low, but no numbers are presented. The air cushion effect observed by Arhan and Deleuil (1978) and

Campbell and Weynberg (1980) was also found by Miao (1989) for the transducer located at the centerline of the cylinder. The measured pressure after the peak shows a decay with a superimposed oscillation of the order of 5 kHz, which is believed to be caused by vibration of the transducers (Miao, 1989). From the graphs, the results from Miao (1989) seem to have less oscillations than those presented in Campbell and Weynberg (1980), however, also Miao experienced scatter for the results during the initial phase. This scatter was reported to be up to 10%. The slamming coefficient was found to be independent of impact velocity, except for the time before the peak value, due to the air cushion. The slamming coefficient from integration of pressure during the initial phase of water impact is plotted in figure 3.2, and we see that the slamming coefficient has a maximum value of $C_s \approx 11$. For submergence $Vt/R > 0.01$ the slamming coefficient is less than 6. It should be noted that the duration of the phase where $Vt/R < 0.01$ is short (0.00027 s to 0.00072 s for the tested velocities) and that dynamic amplification may have occurred for the pressure measurements during this stage.

The velocities were estimated from the displacement record. Based on this, integration of the pressure measurements, and the force record, Miao (1989) presented the following curve for the slamming coefficient:

$$C_s = 6.1e^{-6.2Vt/R} + 0.4 \tag{3.2}$$

Plotting the slamming coefficients from the pressure distribution versus the slamming coefficients from a selection of the methods above show that the peak slamming coefficient from pressure integration is two to four times higher than the other methods, and the decay is steeper. Also note how the equation 3.2 gives a lower peak force and slower decay than his data during this initial phase. It should be mentioned that the experiments by Miao were performed at lower Froude number than those by Campbell and Weynberg (1980). This means that the effect of buoyancy is more important in the results by Miao. The maximum possible buoyancy effect is by Campbell and Weynberg (1980) estimated to be $C_{S,B} \approx \pi/F_N^2$ for Vt/R≤ 1 . Also, equation 3.2 was presented with focus on the later stages of water impact, and when this line is combined with a buoyancy correction it does show relatively good agreement with a force record presented by Miao (1989).

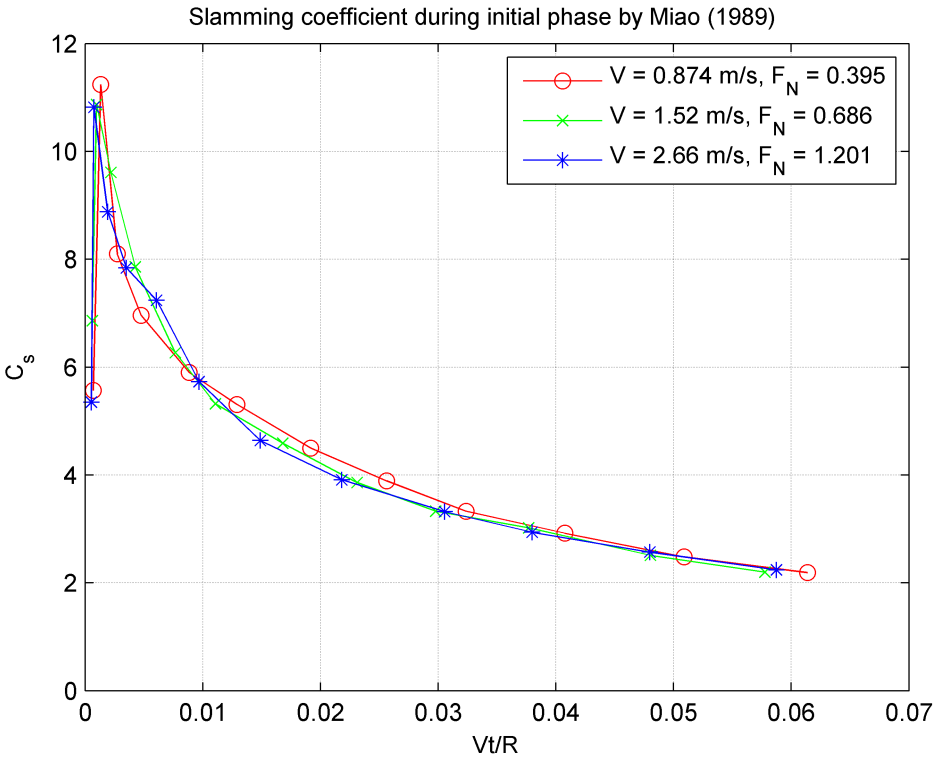

Figure 3.2: Slamming coefficient during the initial phase of water impact from Miao (1989) tables 5-7 to 5-9

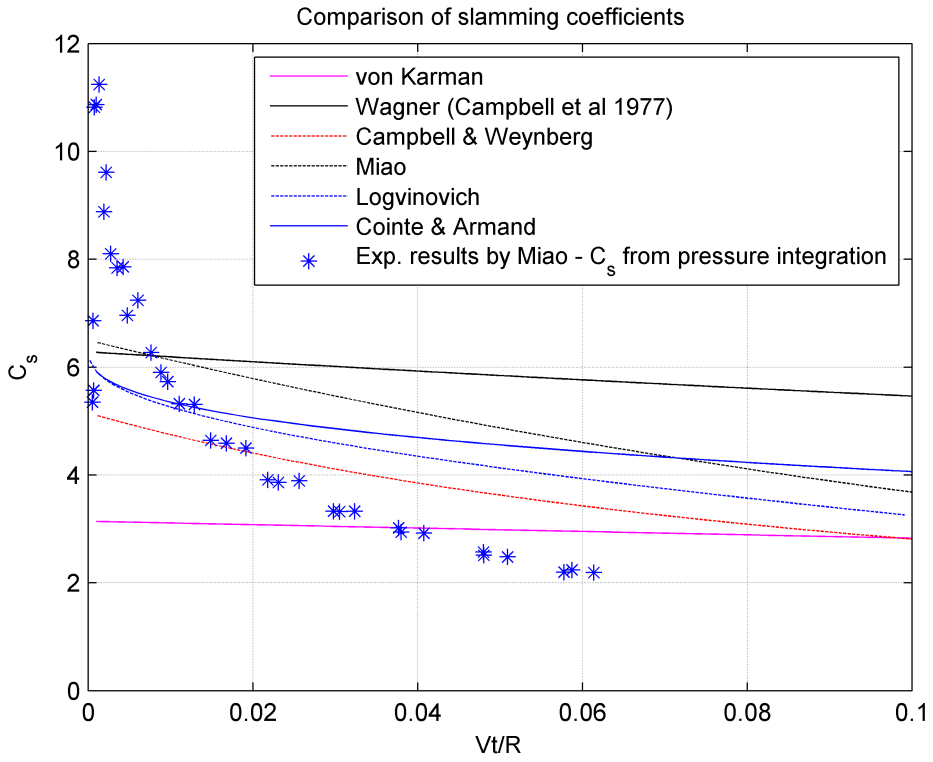

Figure 3.3: Slamming coefficient during the initial phase of water impact from Miao (1989) tables 5-7 to 5-9 plotted vs other methods

3.7 Discussion and establishment of benchmark

As above mentioned, the duration of pressure peaks is small, meaning that the data sampling rate must be high.Van Nuffel et al. (2011) studied the water impact of a rigid cylindrical body with impact speed of 3.4 m/s for different sampling rates. Following the tests, it was recommended that a sampling rate of minimum 200 kHz should be used, as this gives less than 1% error compared to data measured at 100 MHz. Re-sampling the 100 MHz data to 25 kHz showed a reduction in peak pressure of 24%. Although this is assumed to reduce the peak pressure in the measurements for all above discussed experiments, the practical importance of this is small since the duration of the pressure peak exceeding the measure value is extremely short (maximum 1/sampling rate). During testing one should also investigate the effect of vibration of the sensor.

The maximum pressure measured is also dependent on the size of the sensor, as the output will be the average pressure over the sensor. Faltinsen and Chezhian (2005) estimated that for a sensor with diameter=4 mm, the theoretical peak pressure is maximum 11% higher than the space average pressure. The mounting of the pressure gauge is also important, as is the temperature of the sensor (Van Nuffel et al., 2011).

Considering this, none of the above experiments can be assumed show the entire truth about impact loads or impact pressure. However, the results by Campbell and Weynberg (1980) seems to be the most widely used and accepted data for slamming problems. The slamming coefficient they presented has been widely accepted in the industry, and is recommended by e.g. DNV (2010). The results presented by Campbell and Weynberg (1980) are also the most complete series of data available for comparison and will therefore be used for comparison between CFD and experimental results.

In addition, the experiments by Greenhow and Lin (1983) have simplicity as a big advantage, and their results will be used as a benchmark for free fall simulations in STAR-CCM+. Their results are considered the most accurate of experiments presented in this chapter, and the photographs available allows for comparison of not only the slamming force, but also free surface deformation.

4 Computational Fluid Dynamics (CFD)

The science of fluid dynamics for Newtonian fluids have been continuously developed since the time of Newton, and the governing equations for such fluids, the Navier–Stokes equations have been known since the 1840s. For some cases of very low Reynolds numbers with no eddies and simple geometries, these equations have an explicit solution. For higher Reynolds numbers and/or more complicated geometries, no explicit solution has been found.

The science of Computational Fluid Dynamics, or CFD for short, started in the 1970s and at first CFD was used to study simple cases based on potential flow. In the beginning of the 1980s the solution of 2D, and later 3D Euler equations became feasible. Just a few years later, the solution of viscous flows governed by the Navier–Stokes equations were calculated. Together with viscous flows came the difficulties of modeling turbulence, which still is an area under development. The leading edge turbulence modeling today is the Direct Numerical Simulation (DNS), and this is also the most computationally demanding method. Several other methods exist, such as Large Eddy Simulation (LES) and Reynolds Averaged Navier–Stokes (RANS). Due to its computational efficiency, RANS is the most widely used turbulence model in the marine industry.

Following the development of numerical solution methods, increase of computer power and reduced cost of memory, CFD has become increasingly popular. However, it should be emphasized that CFD is a less mature technology than for example finite element methods in solid mechanics, as there are still many open questions, such as turbulence modeling. The trend in offshore industries is that more and more CFD analyses are performed, to reduce the need for model testing. In addition to marine industries, CFD is being widely used in meteorology, car design, biology, oil recovery, civil engineering, biology and many other areas.

Many CFD methods exists, such as Smoothed Particle Hydrodynamics (SPH), Constrained Interpolation Profile (CIP), Finite Element (FE) and Finite Volume Method (FVM). This chapter aims to give an introduction to the use of FVM based CFD for the water impact problem. It should be noted that this chapter is only a brief overview of the topic, and deduction of equations such as the Navier–Stokes equations are not given. Section 4.1 presents the general principles behind CFD, before the use of STAR-CCM+ is presented in section 4.2.

4.1 A General CFD process

This section presents the general principles behind CFD. In general, the following physical principles are the basis of the entire field of fluid dynamics (adapted from Ransau (2008)):

1. Conservation of mass
2. Conservation of energy
3. Newton's second law

Based on these three principles, the continuity –, Euler/Navier–Stokes and energy equations can be established.

Conservation of mass	$\rightarrow$	Continuity equation
Conservation of energy	$\rightarrow$	Energy equation
Newton's second law	$\rightarrow$	Euler/Navier-Stokes equations

By solving the above equations the following macroscopic quantities are obtained:

- The velocities: $\mathbf{v} = [u(x, y, z, t), v(x, y, z, t), w(x, y, z, t)]^T$
- The pressure distribution: $p(x, y, z, t)$
- The density distribution $\rho(x, y, z, t)$
- The temperature distribution $T(x, y, z, t)$

Although CFD can solve a large variety of problems within many fields of study, a general procedure may be established, which explains the work flow for CFD regardless of software and problem at hand. Ransau (2008) summarizes this procedure in the following seven steps:

1. Study the physical flow
   $\rightarrow$ identify main flow phenomena
2. Construct a mathematical model:
   $\rightarrow$ analyze the partial differential equations
   $\rightarrow$ define the (physical) boundary conditions

3. Formulate the numerical problem:
   → construct a mesh
   → choose a time differencing scheme
   → choose a space differencing scheme
   → chose initial conditions
   → choose the (numerical) boundary condition
   → solve difference equations (check for stability and consistency)

4. Implement in a computer code
   → structured programming, environment

5. Run code and obtain solution
   → computer system

6. Analyze and interpret results
   → flow visualization

7. Draw conclusions
   → answer practical problems

4.1.1 Discretization and mesh

The first stage of performing CFD is to transform the governing partial differential equations (PDEs) above into a system of algebraic equations that can be solved by computers.This transformation is known as discretization and a number of discretization methods are available. A brief introduction to discretization is given in this section, whereas the choice of discretization scheme for the water impact problem is discussed in section 5.5.

For most CFD codes, the fluid domain is divided into small elements. The system of such small elements is normally called grid or mesh. In this thesis, a finite volume method (FVM) is applied, hence the small elements are control volumes (CVs). Once the mesh has been generated, the discretization type defines how the governing PDEs are approximated using first-, second-, or higher-order approximations. The choice of discretization generally affects the accuracy of the results and also the stability of the solution. For more information, the reader is referred to a CFD textbook, such as Fletcher (1991)[4.1] or Ferziger and Perič (2003).

[4.1] Volume 2 of the same series may also be of interest

4.1.2 Solvers

In order to solve the algebraic equations established above, a numerical solver has to be chosen. The solver is activated once per iteration for steady-state simulations or once per time-step for transient simulations. Many solvers are available, the difference between them usually being different time- and space differencing scheme. In general, two types of solvers exist; direct solvers and iterative solvers:

Direct solvers For a direct solver, the solution of a linear set of equations can be solved within a "finite" period of time, using e.g. *Gauss elimination*, a *Thomas algorithm* or a *direct Poisson solver*. More information about these solvers can be found in e.g. Fletcher (1991). Direct solvers are in general very robust as long as the precision is good enough for the problem. However, direct methods have several disadvantages, mainly connected to efficiency, as the memory and computing time increase quickly as the problems get larger. They are also inherently difficult to parallelize compared to iterative solver and the computational cost of the direct methods for 3D PDEs grows with the square of the number of equations. (Thies and Wubs, 2011)

Iterative solvers Iterative solvers perform a finite number of iterations to yield an approximate solution, successively modifying an initial guess so that the solution is systematically approached. The accuracy is increased with increasing number of iterations, unless there are numerical difficulties (see section 4.1.3). It should be noted that iterative solvers are generally less robust than direct solvers, especially for certain combinations of equations (mainly from the discretization of mixed parabolic/hyperbolic PDEs).

4.1.3 Convergence, consistency and stability

It is to be expected that the procedure of transforming the governing PDEs into a system of algebraic equations will introduce errors, depending on the discretization. The discretization can be linear or of higher order, but schemes based on higher order discretization often have severe restrictions to ensure stability. In general, the errors depend on the approximations made and the size of the mesh. The goodness of the scheme also depends on the severity of the gradients of the variables such as pressure and velocity.

To ensure that the correct solution is obtained, the following conditions should be satisfied:

Convergence A solution to the algebraic equations is said to be convergent if the solution approaches the exact solution of the partial differential equations as the mesh spacing tends to zero. The error between the solution of the algebraic equation and the PDEs at a node j at time t_n is called the solution error, denoted e_j^n. Convergence of real flows are usually impossible to demonstrate theoretically, but performing analyses on successively refined meshes will normally indicate whether the solution converges or not.

Consistency Consistency means that the system of algebraic equations generated by the discretization process is equivalent to the PDEs at each mesh point as the mesh spacing tends to zero i.e. $\Delta t, \Delta x, \Delta y, \Delta z \to 0$. Consistency is necessary if the approximate solution is to converge to the exact solution, however, it is not a sufficient condition. In order to achieve convergence, the method must also be stable.

Consistency can be tested by inserting the exact solution (if available) into the algebraic equations, and performing a Taylor series expansion of all nodal values about a single point. The resulting expression should then be made up of the original PDEs if the method is consistent.

Stability Given that consistency is satisfied, stability is a necessary and sufficient condition for convergence. Figure 4.1 illustrates the relationship between convergence, consistency and stability. If the method is stable, this means that any errors such as round-off errors introduced at any stage in the computation should decay instead of increase with increasing time/iterations. For an unstable method an error will cause unnatural oscillations with large amplitude or indefinitely growth.

Stability can be tested using e.g. the *matrix method* or the *von Neumann* method. More information on these methods can be found in Fletcher (1991), pages 80-88. The Courant–Friedrich–Levi (CFL) condition (CFL number ≤ 1) indicates the stability of the method. For explicit solvers, the CFL number should preferably be less than 1. Implicit solves are more stable, hence larger CFL-numbers can be allowed. In STAR-CCM+ the CFL number is referred to as the *Convective Courant Number*.

$$\mathrm{CFL} = u_i \frac{\Delta t}{\Delta x_i} \tag{4.1}$$

Here u_i is the velocity in direction x_i. Δx_i is the spatial mesh size in direction x_i and Δt is the time step.

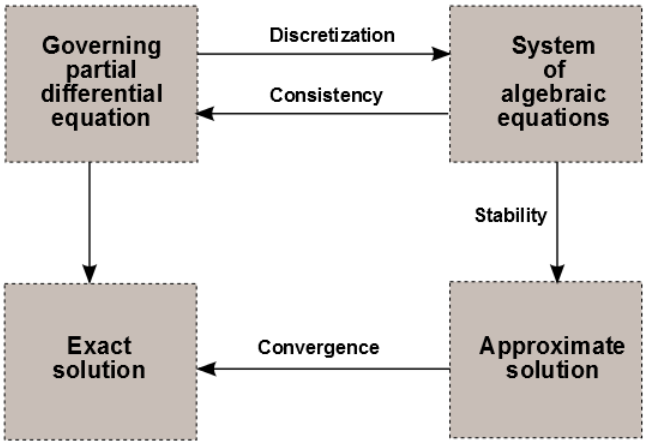

Figure 4.1: Conceptual relationship between consistency, stability and convergence. (Adapted from Fletcher (1991))

Conservation In addition to the requirements above, conservation should also be considered. Since the equations to be solved are conservation equations, this is an important requirement, and all fluid properties should be conserved in the solution procedure. If conservation of the properties are met, the only error one may observe is inaccurate distribution of the fluid properties within the fluid domain in the solution. If conservation not is satisfied, mass, energy, or other properties can be globally altered. Johannessen (2012) stated that conservation is normally not a problem for finite volume methods up to the machine error.

Solution accuracy The above discussion of convergence, consistency and stability has been focusing on the behavior of the solution on a mesh in the limit $\Delta t, \Delta x, \Delta y, \Delta z \to 0$. In reality, the mesh size is finite, hence the corresponding accuracy of such a mesh is of great interest. An important technique for assessing the accuracy is to obtain solutions on successively refined grids and analyzing the behavior of the solution on different grids. In addition, the effects of refining the time step size should be considered. Also, the reality of boundary conditions should be assessed, to make sure that they are correct. An important example here is the distance to any walls and other domain boundaries.

4.2 STAR-CCM+

STAR-CCM+ applies a Finite Volume Method (FVM), which is a *local method*. Other examples of local methods are Finite Element (FE) and Finite Difference (FD). For these methods, a grid of discrete points is distributed throughout the computational domain, in both time and space. The number of grid points required for an accurate solution typically depends on the dimensionality, geometry and the severity of the gradients of the dependent variables. Section 4.2.1 below summarizes the governing PDEs, the discretization, and free surface treatment in STAR-CCM+, and is based on Mørch et al. (2008). The main focus here is on a turbulent flow, but most of the theory is also applicable to laminar (disregard turbulence parts below) and inviscid (disregard turbulence and viscous terms in the equations) simulations.

4.2.1 Governing PDEs and discretization

In the FV method, the mesh points are control volumes (CVs) and the governing equations are surface and volume integrals together with time and space derivatives, as compared to the differential form equations in the FE method. The flow is assumed to be governed by the Reynolds-Averaged Navier–Stokes (RANS) equations, with turbulence included in a eddy-viscosity model (k-ϵ or k-ω). These governing equations on integral form are then approximated over each CV by applying the divergence theorem, converting the volume integrals to surface integrals. For a RANS type simulation, three momentum components and two turbulence properties have to be solved:

Mass conservation:

$$\frac{\mathrm{d}}{\mathrm{d}t}\int_V \rho \mathrm{d}V + \int_S \rho(\mathbf{v}-\mathbf{v}_b)\cdot\mathbf{n}\mathrm{d}S = 0 \tag{4.2}$$

Momentum conservation:

$$\frac{\mathrm{d}}{\mathrm{d}t}\int_V \rho\mathbf{v}\mathrm{d}V + \int_S \rho\mathbf{v}(\mathbf{v}-\mathbf{v}_b)\cdot\mathbf{n}\mathrm{d}S = \int_S (\mathrm{T}-p\mathrm{I})\cdot\mathbf{n}\mathrm{d}S + \int_V \rho\mathbf{b}\mathrm{d}V \tag{4.3}$$

Generic transport equation for scalar quantities:

$$\frac{\mathrm{d}}{\mathrm{d}t}\int_V \rho\phi\mathrm{d}V + \int_S \rho\phi(\mathbf{v}-\mathbf{v}_b)\cdot\mathbf{n}\mathrm{d}S = \int_S \Gamma\nabla\phi\cdot\mathbf{n}\mathrm{d}S + \int_V \rho b_\phi \mathrm{d}V \tag{4.4}$$

Space conservation law:

$$\frac{\mathrm{d}}{\mathrm{d}t}\int_V \mathrm{dV} - \int_S \mathbf{v}_b \cdot \mathbf{n}\mathrm{d}S = 0 \tag{4.5}$$

In these equations, ρ is the fluid density, $\mathbf{v}$ the fluid velocity vector and $\mathbf{v}_b$ is the velocity of the CV surface; $\mathbf{n}$ is the unit vector normal to the CV surface with area S and volume V. T is the stress tensor expressed in terms of velocity gradients and eddy viscosity, p is the pressure, I is the unit tensor, ϕ stands for the scalar variable (k, ϵ or ω), Γ is the diffusivity coefficient, $\mathbf{b}$ is the vector of body forces per unit mass and b_ϕ represents sources or sinks of ϕ.

These equations are then combined with the appropriate boundary conditions and initial conditions.

Free surface treatment The problem in this thesis includes both water and air, and the free surface between them.To include this free surface in the model, a Volume-of-Fluid (VOF) approach is applied, where the fluids are considered immiscible components of a single fluid. VOF is a simple, yet effective multiphase model that can be used for any number of phases, where the interface shape is not constrained, changes in topology are handled automatically, and the mass of each fluid component is conserved. The spatial distribution of each phase is defined using a variable scalar called the volume fraction, α:

$$\alpha_i = \frac{V_i}{V_{tot}} \tag{4.6}$$

where α_i is the volume fraction of fluid i in the cell. In a problem with only two phases, we can simplify this by only defining one volume fraction:

$$\alpha = \frac{V_1}{V_{tot}} \tag{4.7}$$

This volume fraction determines the properties in each cell, i.e. density ρ and viscosity μ for each cell is determined as follows:

$$\rho = \rho_1\alpha + \rho_2(1-\alpha) \tag{4.8a}$$

$$\mu = \mu_1\alpha + \mu_2(1-\alpha) \tag{4.8b}$$

where ρ_1 and μ_1 is density and viscosity of fluid 1 (e.g. water), and ρ_2 and μ_2 the same for fluid 2 (e.g. air). Both fluids can be compressible or incompressible.

The volume fraction is also used to account for the free surface and its arbitrary deformation by including a new equation in addition equations (4.2) - (4.5):

$$\frac{\mathrm{d}}{\mathrm{d}t}\int_V \alpha d\mathrm{V} + \int_S \alpha(\mathbf{v}-\mathbf{v}_b)\cdot\mathbf{n}\mathrm{d}S = 0 \tag{4.9}$$

The volume fraction α is an active scalar, i.e. it has influence on the velocity field.

4.2.2 High-Resolution Interface Capturing (HRIC) scheme

An important aspect when it comes to free surface treatment is that the phases of the mixture (in this case water and air) are separated by a sharp interface, which would be best represented by a *Heavyside step function*. This means that a normal higher-order discretization scheme will not perform well in this area. STAR-CCM+ therefore uses a High-Resolution Interface Capturing (HRIC) scheme specifically made for modeling the convective transport of immiscible fluid components and tracking the sharp free surface. The HRIC scheme is only used for low CFL numbers, by default CFL<0.5. A mix between HRIC and Upwind Differencing (UD) is used for 0.5<CFL<1 and UD is used for CFL>1, meaning that to ensure the sharpest possible free surface, the CFL number should be <0.5 in the vicinity of the free surface. The UD scheme introduces a dissipative error that is stabilizing, but has the effect of "smearing" discontinuities, especially those that are not aligned with the grid lines.The reason for blending the two schemes for 0.5< CFL<1 is to increase stability and robustness. By decreasing the lower limit of blending, one can introduce the mixed scheme at a lower CFL number to increase stability if convergence is difficult to obtain. This will, however, reduce the sharpness of the free surface. The "smearing" effect of high CFL numbers is illustrated in figure 4.2.

A first- or second-order UD scheme can be selected, where the second-order scheme is more accurate and has less dissipation than first order. The reduce of dissipation may result in poorer convergence properties than first order, but this is generally an acceptable trade-off. The dissipation introduced by the UD scheme however, does mean that the results from a free surface simulation with high CFL numbers should be questioned. More information about the HRIC and UD schemes can be found in CD-adapco (2012).

The HRIC scheme also includes a correction to account for the orientation of the interface relative to the cell face orientation, to reduce the tendency of the free

surface to align with the grid.

4.2.3 Solver

In this thesis, a segregated flow model is applied. This is a model for solving the flow equations in a uncoupled manner, linking the momentum and continuity equations with a predictor-corrector approach. The solver is based on a Semi-Implicit Method for Pressure-Linked Equations (SIMPLE) type algorithm, originally presented by Patankar and Spalding (1972). More information about the SIMPLE-algorithm can be found in Ferziger and Perič (2003). CD-adapco (2012) summarizes the algorithm in the following 12 steps:

1. Set the boundary conditions.
2. Compute the reconstruction gradients of velocity and pressure.
3. Compute the velocity and pressure gradients.
4. Solve the discretized momentum equation to produce the intermediate velocity field, $\mathbf{v}^*$
5. Compute the uncorrected mass fluxes at faces $\dot{m}_f^*$
6. Solve the pressure correction equation to produce cell values of the pressure correction p'
7. Update the pressure field: $p^{n+1} = p^n + \omega p'$
   where ω is the under-relaxation factor.
8. Update the boundary pressure corrections p'_b
9. Correct the face mass fluxes: $\dot{m}_f^{n+1} = \dot{m}_f^* + \dot{m}'_f$
10. Correct the cell velocities: $\mathbf{v}^{n+1} = \mathbf{v}^* - \frac{V \Delta p'}{\mathbf{a}_p^v}$
    where $\Delta p'$ is the gradient of the pressure corrections, $\mathbf{a}_p^v$ is the vector of central coefficients for the discretized linear system representing the velocity equation and V is the cell volume.
11. Update density due to pressure changes.
12. Free all temporary storage.

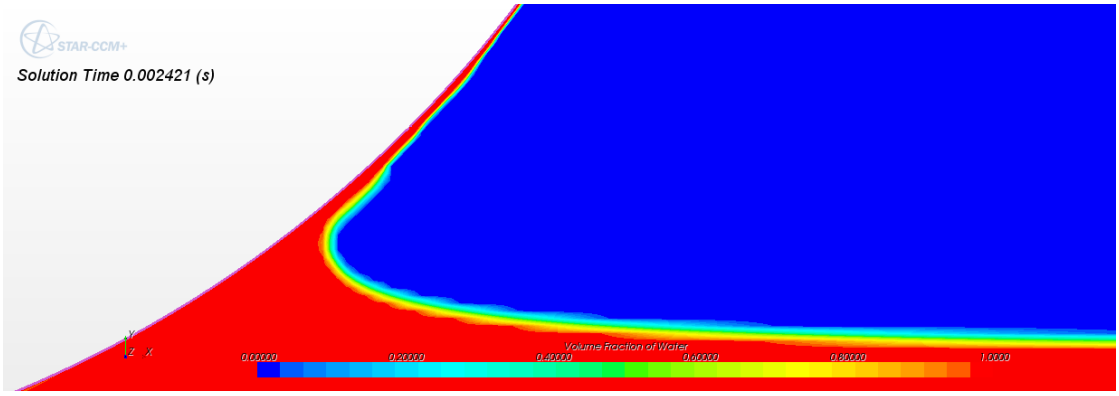

(a) Initial free surface in spray root

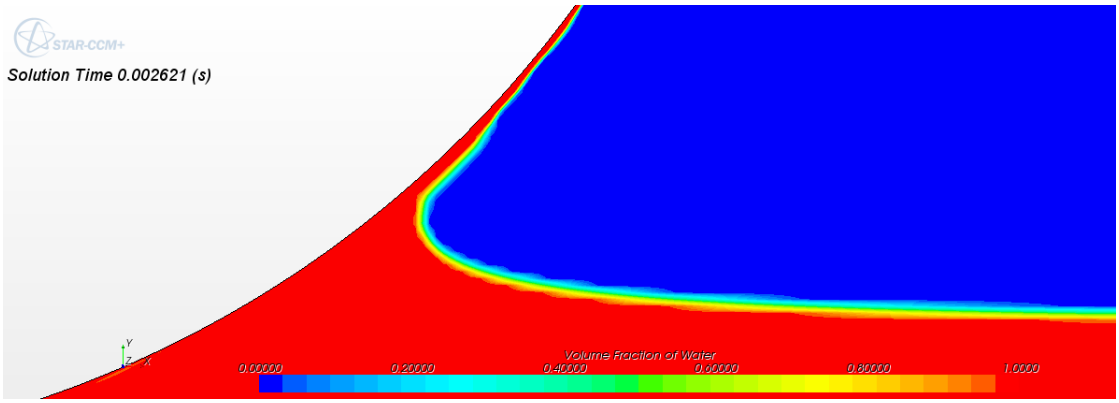

(b) Time step $\Delta t = 10^{-6}$. $CFL_{free\ surface} \approx 0.1$. The free surface is still sharp after 0.0002 s (200 time steps)

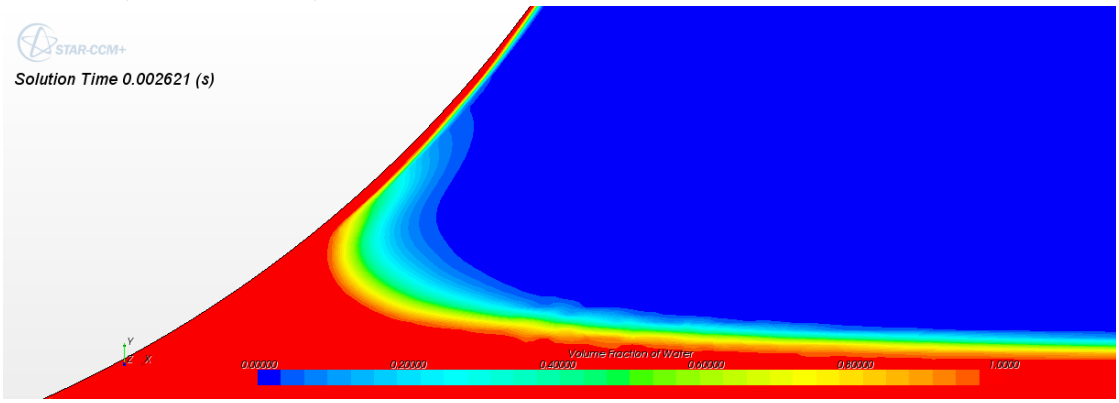

(c) The smearing effect of higher CFL number is clearly visible after only 0.0002 s (2 time steps). $\Delta t = 10^{-}4$ s, $CFL_{free\ surface} \approx 10$

Figure 4.2: Smearing effect on the free surface due to high CFL numbers. 0.5 mm prism layer and 0.0625 mm trimmer mesh size.The simulation up to t=0.002421 s is performed using time step size $\Delta t = 10^{-6}$ s.

A flow chart of the calculation procedure including a floating body is illustrated in figure 4.3.The segregated flow solver is applicable for incompressible and mildly compressible flows.

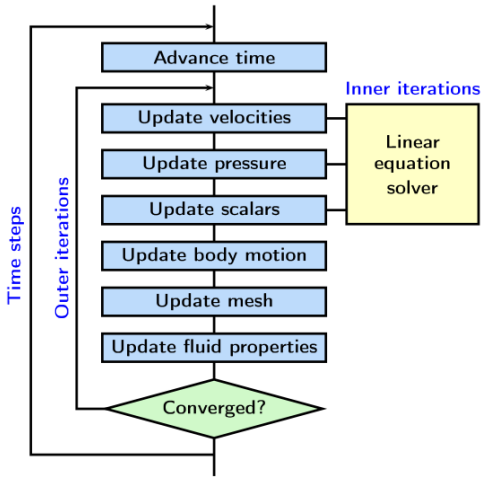

Figure 4.3: Flow chart of the iterative solution method for a coupled simulation of fluid flow and flow-induced motion of a floating body. (Mørch et al., 2008)

To ensure convergence, a certain number of iterations have to be performed. The number of iterations needed can be found by studying the residuals, which represents the degree to which the discretized model is not satisfied. For a problem with a free surface, the most important residual is the residual for water and air at the free surface. The number of outer iterations is in STAR-CCM+ set manually, with a default value of 5 iterations for each time step. The number of inner iterations in the linear equation solver is automatically chosen, and depends on several factors, such as time step size and under-relaxation factors chosen. A typical number of inner iterations for a transient VOF problem with all CFL<1 is 2-5.

4.2.4 Workflow

As for all CFD software, a certain workflow should be followed. This workflow consists of modeling and defining the problem, solving it, and later analyze the results. The workflow for STAR-CCM+ is illustrated in figure 4.4 below. This section will present a recommended workflow for a VOF type CFD analysis in STAR-CCM+

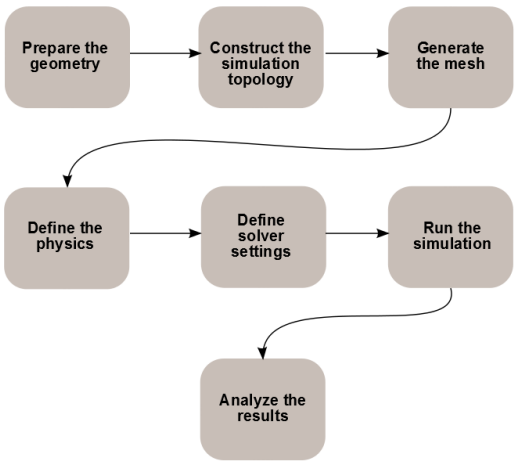

Figure 4.4: STAR-CCM+ workflow overview

Geometry The first part of the workflow consists of modeling the geometry that will be used. This geometry can be imported from CAD software such as SolidWorks and Rhino3D, or it can be created in the integrated 3D-CAD module in STAR-CCM+. The 3D-CAD module allows for creating parts from scratch, and can also be used for modifying imported CAD models

Simulation topology Before applying physics and solving the problem at hand, the computational model must be defined in terms of regions and boundaries. Regions are volume domains that are completely surrounded by boundaries, see figure 4.5.

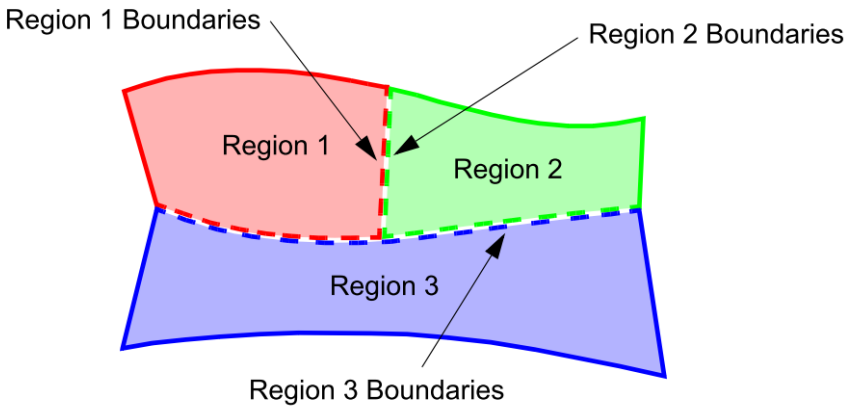

Figure 4.5: Definition of regions and boundaries in STAR-CCM+ (CD-adapco, 2012)

The mapping between the geometrical definitions of the problem and the computational definitions is known as the simulation topology. When defining the simulation topology, geometry parts are assigned to regions and part surfaces are assigned to boundaries. This mapping process has to be completed before any meshing can be performed. The regions will also later be used in the definition of physics for the model by defining region types.

The following region types exist in STAR-CCM+:

- Fluid region
- Solid region
- Porous region

Boundaries are surfaces that surround and define a region, and many boundary properties exists in STAR-CCM+. The boundaries relevant for water impact simulations are:

- Pressure outlet: A flow outlet boundary at which the pressure is specified.
- Symmetry plane: An imaginary plane of symmetry in the simulation. The solution obtained with a symmetry plane is the same as if the mesh were mirrored about this plane.
- Wall: An impermeable surface that can have a slip- or no-slip condition.
- Velocity inlet: A boundary where the flow velocity is known.

Mesh Once the simulation topology is defined, the computational domain should be divided into control volumes. Meshing is in STAR-CCM+ performed in two steps; first surface meshing and then volume meshing.

Surface mesh Two surface meshing models are provided with STAR-CCM+; the *surface remesher* is provided for geometries that have been imported from CAD models or that are created in 3D-CAD. This meshing model must always be used. The other meshing model is the *surface wrapper* which can be used to extract fluid volumes, simplify complex assemblies or provide a closed surface over a poor quality CAD model. The *surface wrapper* can also be used to simplify CAD models that have more details than needed for the simulation. In cases where the *surface*

wrapper is utilized, the *surface remesher* has to be has to applied on the model after the surface wrapper to provide a high-quality starting surface for the volume mesh.

Volume mesh Once finished with the surface mesher, the volume mesh is the next step. Several volume meshing models are provided, the main models being (CD-adapco, 2012):

- **Tetrahedral mesher:** The fastest meshing model, and uses the least amount of memory for a given number of cells. This mesh is normally used to provide an efficient and simple solution for complex meshing problems.
- **Polyhedral mesher:** Suited for complex, multiregion geometries
- **Trimmer:** Uses a predominantly hexahedral mesh, is efficient at filling large volumes, and uses less memory per cell than the polyhedral mesh.
- **Thin mesher:** For thin geometries such as solid plates.
- **Advancing Layer Mesher:** Generates a layer of prismatic cells around the surfaces of regions and fills the remaining void with polyhedral cells.

In general, the choice of mesh is dependent on several factors such as desired solution accuracy, amount of memory available, whether the mesh is single- or multi-region, quality of the starting surface mesh and size/shape of the geometry. According to Johannessen (2012), the trimmer mesh is expected to provide the best results when working with multiphase flow and free surface due to its ability to describe a smooth free surface.

In addition to the volume mesh models mentioned above, several additional features can be added, such as the prism layer model which produces prismatic cell layers near the wall boundaries. The prism layer model is recommended in the shear layer, especially for turbulent flows and when viscous effects are important. These elements are highly stretched (high aspect ratio), hence the number of elements can be reduced compared to other mesh types. For more information on these additional models, see CD-adapco (2012).

Mesh quality If the mesh is of low quality, this can negatively impact the accuracy and efficiency of the solution, or make the simulation crash. Examples of low quality or invalid mesh can be negative or zero volume cells (normally due

to incorrect face orientation), unclosed cells[4.2], disadvantageous aspect ratios or extreme volume ratio between neighboring cells. Whether a mesh is valid or not depends on the physics of the simulation and choice of solver. The stability of the solution is affected by the mesh, hence the appropriate choice of under-relaxation factors and CFL number specifications are dependent on the mesh. Several mesh validity checks are provided with STAR-CCM+, and it is recommended that the mesh is controlled before simulations are started.

Physics and solver settings STAR-CCM+ contains a wide range of physics models. This allows the software to simulate both single- and multiphase fluid flow, turbulence, aeroacoustics, solid stress, turbulence, heat transfer and related phenomena by selecting a *physics continuum*. Essentially, the model selected defines the primary variables in the simulation, such as pressure, temperature and velocity, and the applicable mathematical formulation needed for the solution. The model activated determines whether the the continuum comprises a solid, fluid or gas, whether it is transient or stationary in time, whether it is two- or three-dimensional etc. Certain models also require other models to be activated. An example of this is that if a fluid model is activated, this model needs a flow model, which again needs a viscous model. If this viscous model is turbulent, a turbulence model must be selected.

A simulation may have multiple physics continua, but a single mesh region can only be associated with one. The region types (fluid, solid or porous) and boundary conditions are defined as a part of the physics settings. Initial conditions such as initial velocity and pressure are also defined here.

Time models STAR-CCM+ provides three time models:

- Steady
- Implicit unsteady
- Explicit unsteady

The primary function of the time model choice is to control the time-stepping in the solver. Only the implicit unsteady model can be used in combination with the segregated flow model. This is according to Johannessen (2012) due to the fact that the VOF model is unable to solve the pressures and velocity components in a coupled manner.

[4.2] Unclosed cells refers to cells missing a face or where the outward normals are not consistent

Motion models For models including a body moving relative to the fluid reference frame, different categories of motion can be chosen i STAR-CCM+. These choices can be divided into three broad categories:

- **Mesh Displacement in Real Time (MDRT)**: Methods involving displacements of mesh vertices in real time. This category is to be used with a transient analysis. Within this category several methods are available
  - Rigid motion (Rotation and/or translation, for motion of an entire region)
  - Morphing (deforming mesh)
  - Dynamic Fluid Body Interaction (DFBI)
  - Solid Displacement (mesh updated based on solid deformations due to stress)
  - User-Defined Vertex Motion (displacement or velocity set by the user for every vertex)
- **Moving Reference Frame in Steady-State (MRFSS)**: Used when converting an unsteady motion to steady-state by imposing a moving reference frame on a static mesh. Can be used for simulating rigid rotation and/or translation.
- **Harmonic Balance Flutter**: Used for analysis of turbines with blade vibration.

Solver settings and post processing After the motion model has been defined, the time steps and stopping criteria should also be defined, as well as underrelaxation factors and other solver settings. These settings are typically chosen based on previous experience or residuals and convergence studies. The residual for water and air is the most important residual when simulating free surface flows, and it is normally recommended that the residual drops in the order of 10^2 for each time step. However, a drop in the order of 10^1 has been shown to give a converging solution (Kopperstad, 2011).

The field functions[4.3] can be analyzed during the computation or after completion. This can be done by creating reports, plotting data sets and/or visualizing the solution data. Different scenes can also be defined before the simulation is

[4.3]Field functions provides the user with the possibility of monitoring and storing raw-data from the calculations

started or during the simulation, in which the flow pattern, pressure and other results can be viewed real time during simulation. However, it should be noted that open scenes will slow down the computation.

5 Constant velocity water entry of 2D circular cylinder

Using CFD to simulate 3D flows and complex geometries is still relatively time consuming. Even with the increase in computational power seen for personal computers over the last decade, computer clusters are still required for complex 3D simulations. 2D problems on the other hand, are much faster. With this in mind many 3D problems can be simulated in 2D without significant errors. This the case for a long horizontal cylinder impacting on a flat free surface, where the end effects are assumed to be negligible

In this chapter, water entry of 2D circular cylinder with radius $R = 10$ cm is studied using STAR-CCM+. The vertical velocity of the cylinder is V=5.0 m/s giving a Froude number $F_N = 3.57$. This velocity and Froude number has been chosen based on the experiments presented in chapter 3, with focus on the experiments by Campbell and Weynberg (1980).

Domain, mesh and time step size studies are performed using a laminar flow model, based on recommendations by Johannessen (2012). Motion is modeled using the *Mesh Displacement in Real Time (MDRT)* model described in section 4.2.4 with rigid body motion of the cylinder and the mesh while the water surface is retained at a globally fixed position. The effect of laminar versus turbulent flow model is studied in section 5.6. Water impact simulations using an inviscid flow model is treated in section 5.7.

The most important parameter for a cylinder impacting on a free surface is the vertical hydrodynamic force on the cylinder, also known as the slamming load. This force is in the following represented by the non-dimensional slamming coefficient, C_s as presented in section 2.1. Due to uncertainties in the experiments performed for similar problems, no 100% accurate data are available for comparison. The convergence studies of the CFD simulation are therefore first considered, before comparing the CFD results to experimental data.

5.1 Domain size

One of the important challenges when performing CFD simulations is to decide on an appropriate domain size. For the simulations in this chapter, the domain is shaped as a box limited by symmetry planes at the vertical sides, velocity inlet at the bottom and a pressure outlet at the top. It is important that all boundaries (except the symmetry plane at the cylinder center) are sufficiently far from the cylinder to avoid any unwanted effects of these boundaries. Four different domain sizes have been tested.

The physics models selected for the domain size analyses are shown in figure 5.1.

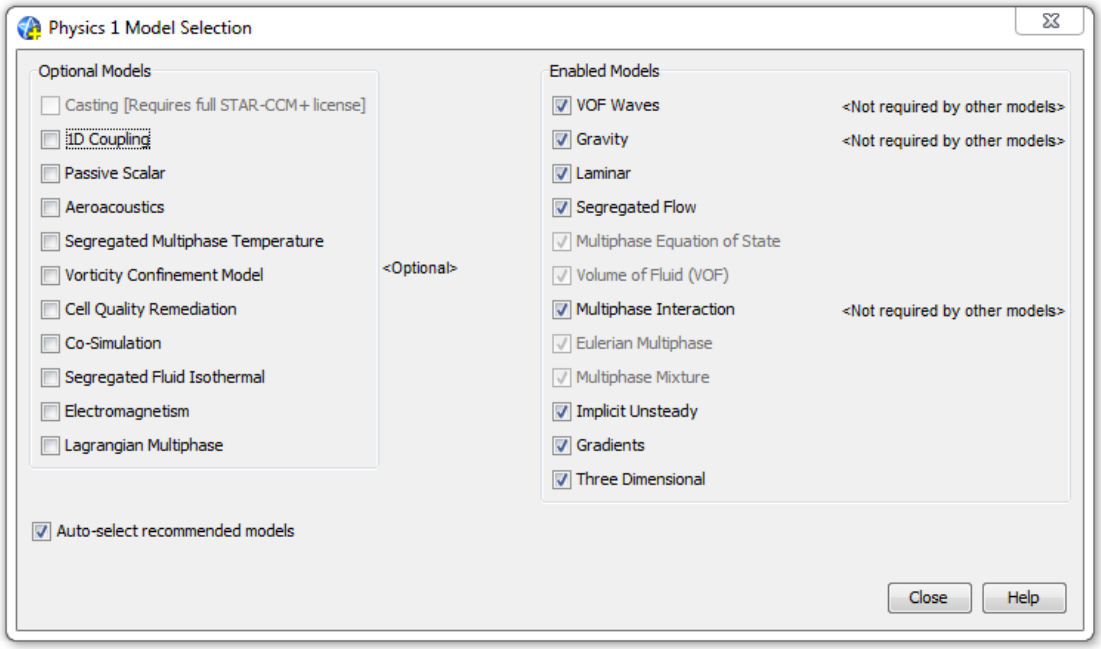

Figure 5.1: Physics model selection for domain size analysis

STAR-CCM+ is primarily made for 3D simulations. 2D simulations can be performed but the geometry and mesh must be made in three dimensions and then transformed. Once the mesh has been transformed to 2D, no changes can be made to it. Most 2D problems in STAR-CCM+ are therefore simulated using a narrow domain with symmetry planes on each side instead. By choosing a thickness of the same order as the mesh element size, one or two elements can be used in the third dimension to ensure as low computational cost as possible.

A trimmer mesh has been applied to the domain, with maximum cell size 10

mm x 10 mm far away from the cylinder. Close to the cylinder, the cell size is 0.625 mm x 0.625 mm. The boundary layer close to the cylinder is modeled using the *Prism Layer Mesher* with 0.5 mm thickness and 8 elements in the radial direction. The trimmer mesh size close to the boundary layer should be of same order of magnitude as the outer prism element to ensure convergence and realistic flow patterns. The mesh close to the cylinder is illustrated in figure 5.2. Small elements are required on the cylinder surface to accurately calculate the velocities and pressure in this area. See section 5.2 for a study on the effect of mesh size on the vertical force.

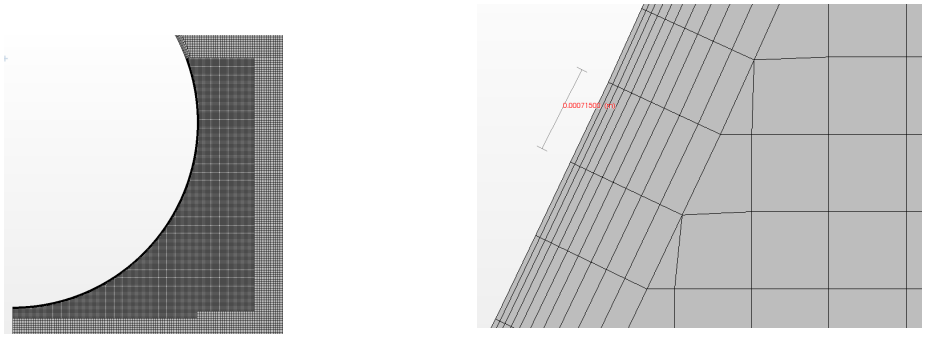

(a) Overview

(b) Mesh close to the cylinder for domain size testing

Figure 5.2: Inner domain mesh

Varying time steps have been used in the simulations to reduce the computational time. The first phase of impact requires small time steps due to the rapid propagation of the spray root and as submergence increases, the time step can be increased without reducing the accuracy of the solution. The time steps have been chosen so that the CFL number is less than 1 everywhere in the domain and less than 0.5 on the free surface. The time steps used are shown in table 5.1.

Submergence interval	Time interval [s]	Time step size [s]
0.0<Vt/R<0.025	0.0<t<0.001	$5 * 10^{-7}$
0.025<Vt/R<0.125	0.001<t<0.0025	$1 * 10^{-6}$
0.125<Vt/R<0.5	0.0025<t<0.01	$2 * 10^{-6}$
0.5<Vt/R<1	0.01<t<0.02	$5 * 10^{-6}$

Table 5.1: Time steps for domain size simulations

The total number of time steps in each simulation is 9 250.

Figures 5.4 and 5.5 show that the smallest domain over-predicts the vertical pressure and force, compared to the larger domains. The differences between

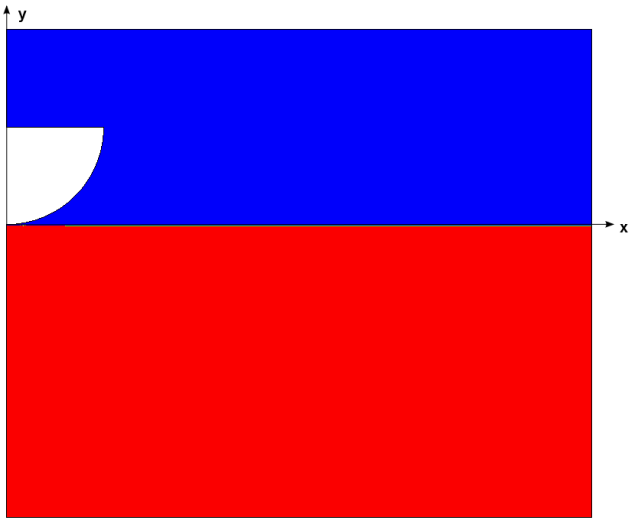

Figure 5.3: Domain with coordinate system

Domain	x_{min} [m]	x_{max} [m]	y_{min} [m]	y_{max} [m]	Tot. number of cells	CPU time per step [s]
D1	0	0.4	-0.4	0.4	57 610	3.0
D2	0	0.8	-0.8	0.6	65 960	3.7
D3	0	1.2	-1.2	0.8	79 493	4.0
D4	0	1.5	-1.5	1.0	92 614	4.2

Table 5.2: The four different domains used in the domain size analysis.

Prism layer thickness	0.5 [mm]
Number of prism layer elements	8
Prism layer stretching	1.2
Trimmer mesh size close to cylinder	0.625[mm]

Table 5.3: The mesh used in the for domain size analysis

Domain	$P_{\text{max, cylinder}}$ [Pa]
D1	29 425
D2	24 141
D3	23 210
D4	23 042

Table 5.4: Maximum pressure on the cylinder surface at $Vt/R = 1$ for different domain sizes

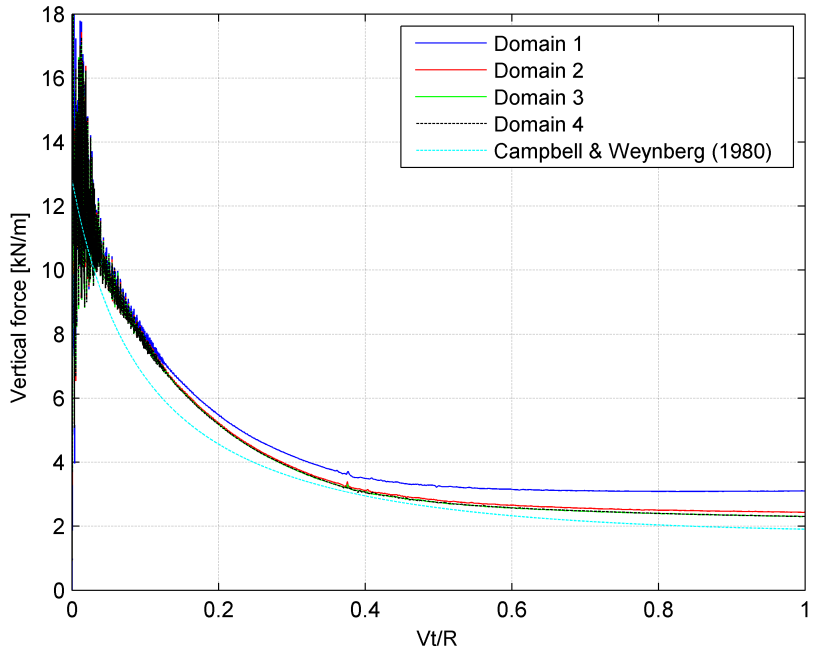

Figure 5.4: Vertical force on cylinder for various domain sizes.

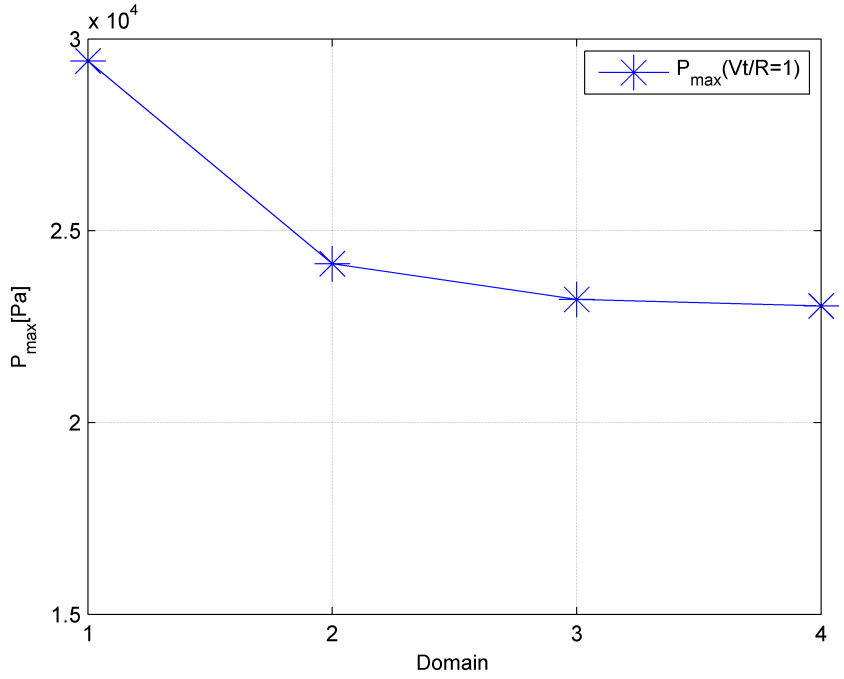

Figure 5.5: Maximum pressure on cylinder versus domain size at Vt/R=1

domains 2, 3 and 4 are small. The appropriate domain size also depends on the submergence interval to be studied, since the difference increases with increased submergence. For most problems, Domain 2 is considered sufficient, especially when small submergence is to be studied. However, the CPU time increase from Domain 2 to Domain 3 is relatively small (about 8%), and domain 3 has therefore been used for the analyses in the next sections to eliminate domain boundary effects.

The fluctuations seen at the initial phase of impact in figures 5.4 and 5.6 are caused by a pressure peak in the spray root that covers a smaller area than the mesh size. The vertical force acting on the cylinder is calculated based on the pressure at the interfaces between grid cells. When this pressure peak coincides with a cell boundary this means that the pressure is multiplied by a too large area, whereas when the pressure peak is located inside a cell, this pressure peak is not properly resolved. The magnitude of these force peaks are smaller for a finer mesh, as the pressure peak then is multiplied by a smaller area. The period of the fluctuations are also smaller for a finer mesh due to the decreased distance between cell interfaces.

5.2 Mesh size

When conducting CFD simulations, the next step after determining domain size is to find a mesh where all significant contributions to the simulations are included. In water impact simulations, especially the pressure peak in the spray root is important for the results, and this pressure peak occurs over a small area, implying that a very fine mesh should be used. However, the mesh size is also dependent on the accuracy needed and time available for the simulation.

For free surface problems, it is favorable to have small CFL numbers on the free surface, as the HRIC method described in section 4.2.1 is used for CFL$<$0.5 and a mix between HRIC and UD is used for 0.5$<$CFL$<$1. It is therefore recommended to keep CFL$<$0.5 for all cells on the free surface. Also, a lower CFL number normally improves convergence, and may reduce the necessary number of iterations for each time step.

In the mesh size analysis, time steps have been chosen so that the CFL number is less than 1 everywhere in the domain and maximum 0.5 on the free surface. Dependence on time step size is studied in section 5.3.

To identify the different test cases, they have been named as follows; TxPyy, where x is the trimmer mesh number (see table 5.5) and yy is the number of

elements in the radial direction of the prism layer.

5.2.1 Trimmer mesh

Four different trimmer mesh sizes have been tested. The area close to the cylinder is for all simulations modeled using a 2 mm thick prism layer with 25 elements in the radial direction. For mesh T1, the area close to the cylinder is composed of the same elements as the T2 mesh, with a coarser mesh further from the cylinder. More information about the mesh is given in table 5.5.

Case	Number of cells	Trimmer cell size [mm]	Number of time steps
T1P25	46 062	1.25000mm	13 600
T2P25	89 574	0.62500mm	13 600
T3P25	211 764	0.31250mm	27 200
T4P25	886 578	0.15625mm	76 000

Table 5.5: The four different mesh sizes used in the trimmer mesh size analysis. Naming convention: TxPyy where x is the trimmer mesh size identifier and yy is the number of elements in radial direction in the prism layer

Submergence interval	Time interval	T1P25 & T2P25 Δt [s]	T3P25 Δt [s]	T4P25 Δt [s]
0.0<Vt/R<0.2	0.0<t<0.004	$5 * 10^{-7}$	$2.5 * 10^{-7}$	$1 * 10^{-7}$
0.2<Vt/R<0.3	0.004<t<0.006	$1 * 10^{-6}$	$5 * 10^{-7}$	$2.5 * 10^{-7}$
0.3<Vt/R<0.5	0.006<t<0.01	$2.5 * 10^{-6}$	$1 * 10^{-6}$	$5 * 10^{-7}$
0.5<Vt/R<1	0.01<t<0.02	$5 * 10^{-6}$	$2.5 * 10^{-6}$	$5 * 10^{-7}$

Table 5.6: Time steps for trimmer mesh size analyses

The slamming coefficient for all mesh sizes has been calculated based on the total vertical force (pressure+viscous) from STAR-CCM+. Figure 5.6 shows the slamming coefficient for the initial phase of impact, where the force fluctuations due to the mesh as discussed in section 5.1 are clearly visible.

It is believed that a more realistic force record is found by filtering out the fluctuations using a sliding average function. In figure 5.7 the graphs have been smoothed using the moving average MATLAB function *smooth*. This function smooths the data using a moving average filter as described in Appendix A.

Figures 5.6 to 5.8 show that the different mesh sizes give almost the same results. The largest difference in calculated slamming coefficients is found during

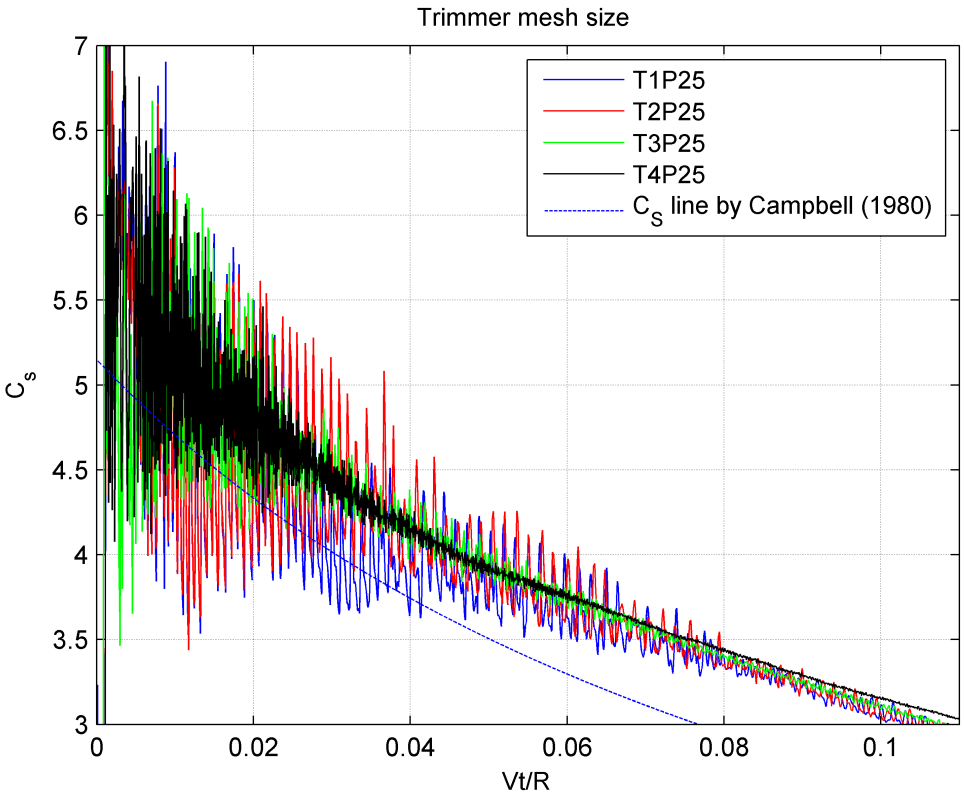

Figure 5.6: Slamming coefficient for different mesh sizes during initial phase of impact. (Laminar flow model.)

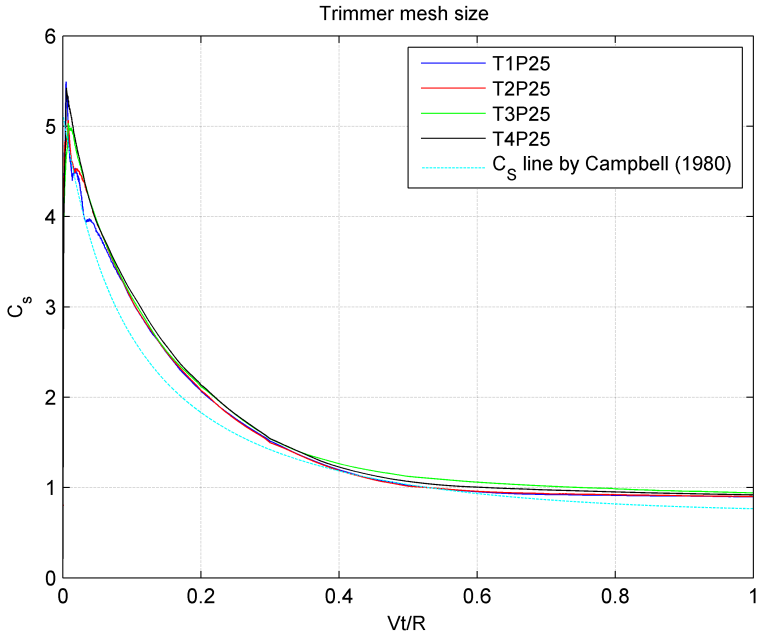

Figure 5.7: Slamming coefficient for different mesh sizes. Laminar flow model. Smoothed plot.

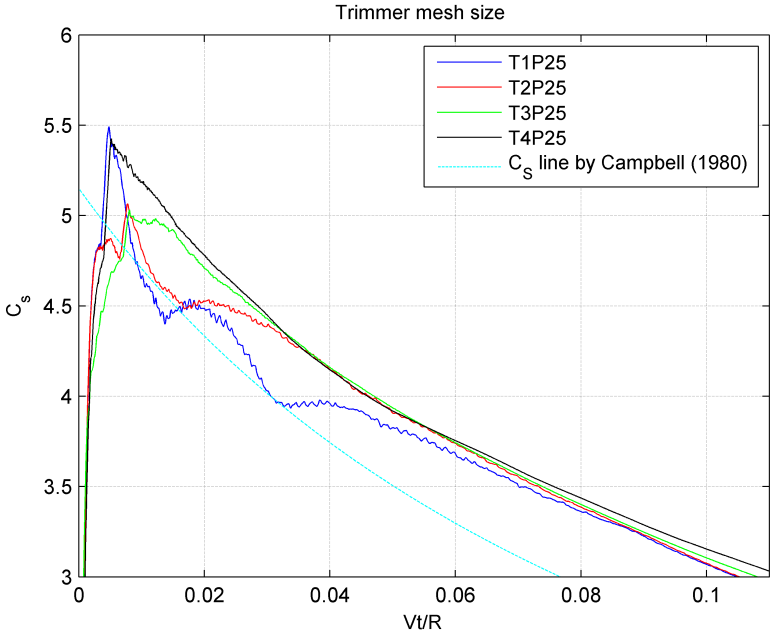

Figure 5.8: Slamming coefficient for different mesh sizes during initial phase of impact. Laminar flow model. Smoothed plot.

the initial phase ($Vt/R < 0.05$), where a finer mesh has been found to give a higher slamming coefficient (except for a peak in the T1P25 force record at $Vt/R = 0.006$, see figure 5.8). Whether this is caused by the mesh size of the reduced time step for the finer mesh if studied in section 5.3. For deeper submergence the results indicate that a relatively coarse mesh may be used. The plot shows that the C_s value from STAR-CCM+ lies above the value calculated from the line by Campbell and Weynberg (1980) for all submergences.

5.2.2 Prism layer size

A prism layer of 2 mm thickness has been tested with various number of elements using a T2 trimmer mesh outside the prism layer. The stretching factor is 1.2 for all tests, i.e. the thickness of one element in the prism layer is 1.2 times the thickness of the next element towards the cylinder.

Case	Number of cells	Number of prism layer elements	Thickness of inner layer [mm]	Thickness of outer layer [mm]
T2P15	82 534	15	0.02777	0.35645
T2P20	86 054	20	0.01071	0.34225
T2P25	89 574	25	0.00424	0.33685
T2P30	93 094	30	0.00169	0.33474

Table 5.7: The four different meshes used in prism layer analysis

The prism layer mesh is important for obtaining correct results. It has been found that especially the water separation and jet formation are highly dependent on the mesh close to the cylinder, and a potentially important flow feature may therefore be ignored if an inappropriate mesh is used in this area. The flow pattern close to the cylinder should therefore be thoroughly inspected for each mesh and physics setup to ensure that these features are properly modeled.

The slamming coefficients for different prism layers are plotted in figure 5.9, showing a clear convergence as the number of elements in the prism layer is increased, with the difference between 25 and 30 layers being negligible.

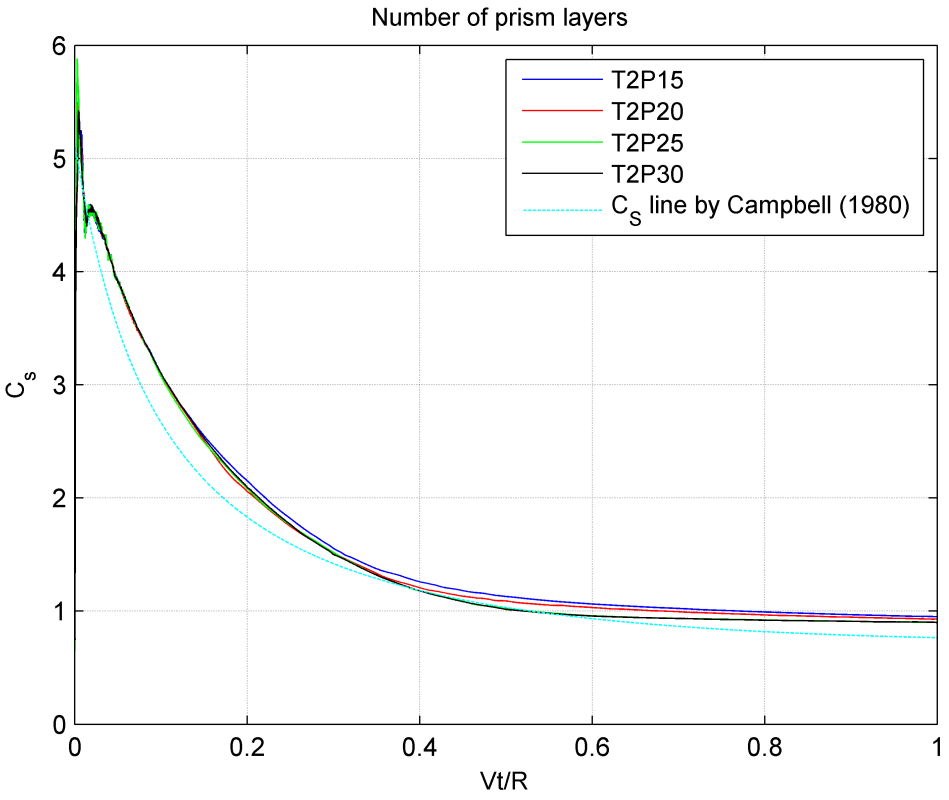

Figure 5.9: Slamming coefficient for different mesh sizes. Laminar flow model. Smoothed plot.

5.3 Time step size

As discussed earlier, the maximum allowable time step is dependent on the mesh size. In this section, the effect of changing time step size has been investigated for a selection of meshes from section 5.2.1.

Explicit codes are prone to instability for CFL numbers greater than one. Implicit codes, as used in this thesis are less susceptible for higher CFL number, hence smaller grid size and/or longer time steps may be used. The maximum CFL number allowed is also dependent on the choices made during setup of the analysis, such as discretization scheme and the under-relaxation factors.

For the solver settings used in this chapter, it is recommended to ensure that the CFL number is less than 0.5 on the free surface to ensure a sharp interface, and 1 everywhere else (Tsimis, 2013). Therefore, instead of just monitoring the maximum CFL number in the entire domain, also the position of the maximum CFL number should be considered if the maximum time step size is to be found.

It has been found that the maximum CFL number normally is located in the elements between the prism layer and the trimmer mesh where there are small triangular elements. These elements are smaller than normal cells to connect the prism layer mesh to the trimmer mesh. Whether higher CFL should be allowed in this area must be determined from case to case. One example is shown in figure 5.10 where the free surface in the spray root area is plotted together with the CFL number for each cell. The maximum CFL number is found in the triangular elements, which in this case only contains air and are located several elements from the free surface, hence larger CFL numbers may be allowed without reducing accuracy.

It is often preferred to use a constant time step size during the entire simulation, as changing the time step must be done manually by stopping the simulation and changing the time step. For the water impact problem, small time steps are needed during the initial phase, whereas larger time steps may be used later in the simulation. Conducting simulations with constant time steps small enough for the initial increases the computational time significantly compared to variable time steps. Meshes T2P25, T3P25, and T4P25 have been analyzed with constant time steps using the same naming convention as in section 5.2, with the addition of a time step size tag.[5.1] See table 5.8.

The slamming coefficient for each test is plotted in figures 5.11 and 5.12 as a function of non-dimensional submergence. Some differences are seen for the

[5.1] FDT=fixed Δt, the number following FDT is the time step size

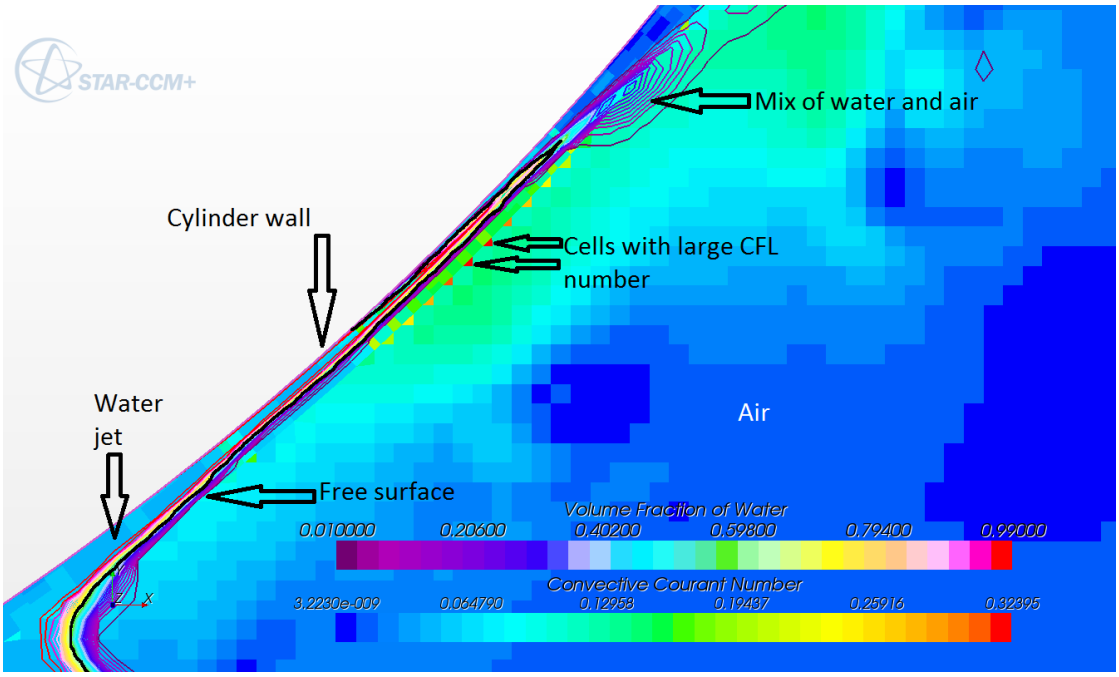

Figure 5.10: CFL number in cells close to the cylinder surface plotted with isolines of the VOF function defining the volume fraction of water. Mesh: T2P25, $\Delta t = 10^{-6}s$. The red triangles indicates the cells where the CFL number is large. In this case the cells are not on the free surface, hence a CFL number >0.5 can be allowed.

Case	$\Delta t[s]$
T2P25-FDT5e-7	$5.0 * 10^{-7}$
T2P25-FDT2.5e-7	$2.5 * 10^{-7}$
T2P25-FDT1e-7	$1.0 * 10^{-7}$
T2P25-FDT5e-8	$5.0 * 10^{-8}$
T3P25-FDT2.5e-7	$2.5 * 10^{-7}$
T3P25-FDT1e-7	$1.0 * 10^{-7}$
T3P25-FDT5e-8	$5.0 * 10^{-8}$
T4P25-FDT1e-7	$1.0 * 10^{-7}$
T4P25-FDT5e-8	$5.0 * 10^{-8}$

Table 5.8: Time steps for time step analyses and naming convention

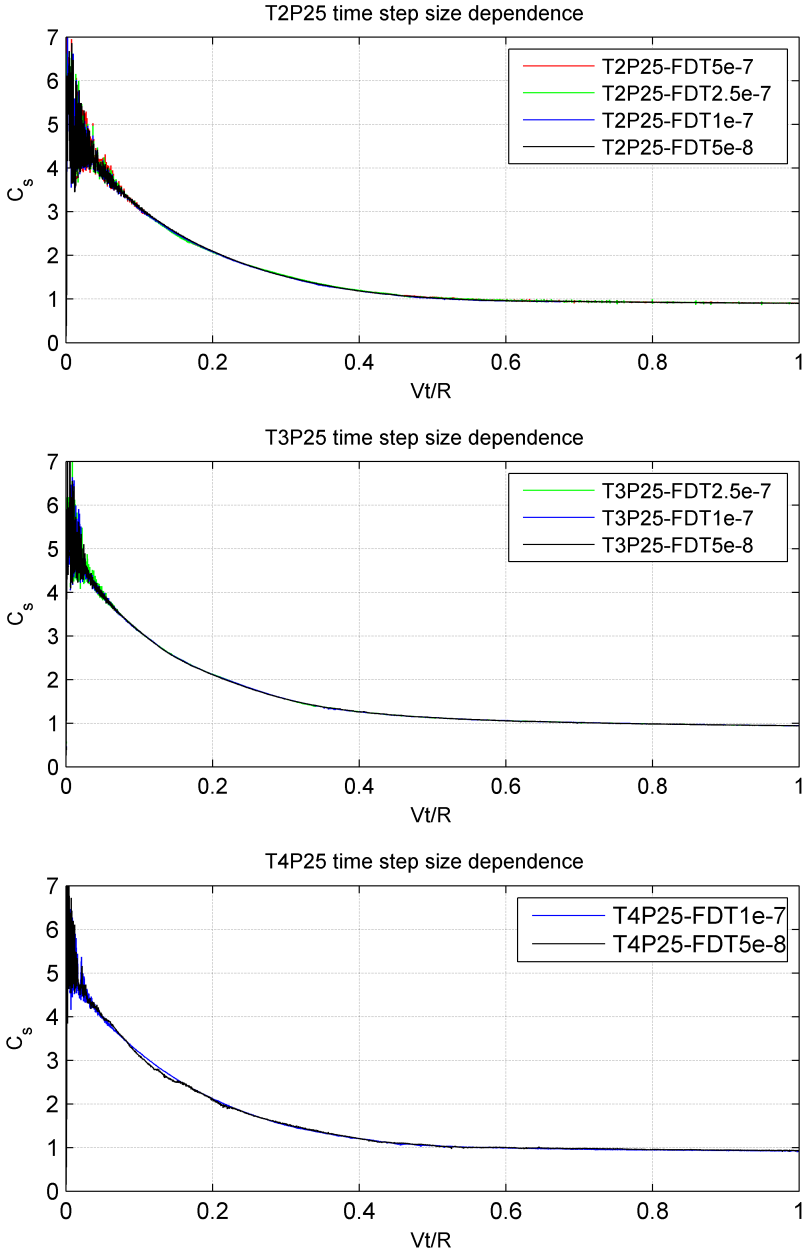

Figure 5.11: Slamming coefficient as a function of submergence for various mesh sizes and time steps

largest time steps for mesh T2P25 and T3P25, but except for this initial phase, the slamming coefficient is considered independent of time step size.

The plots indicate that the differences seen in figure 5.8 are not caused by the time step size. To further investigate this, additional analyses have been performed where the simulation is started at $Vt/R = 0.005$ above the free surface to include the rise of the slamming load. The slamming coefficient for various time step sizes is shown in figure 5.13 where it can be seen that the rise-time increases with mesh size. This difference is caused by the fact that the free surface is not sharply defined in a VOF type simulation, and with a larger mesh (T2P25 and T3P25 versus T4P25), the cell layer where the fluid properties is a mix between water and air is thicker. The non-dimensional thickness of this layer is thickness$/R = 0.006250$ for mesh T3P25 and thickness$/R = 0.003125$ for mesh T4P25. The highest peak value for the slamming coefficient is found at the moment where the bottom of the cylinder is located at the bottom of the free surface cell. These spikes are of very short duration, thus the practical interest of these is small.

Studying the averaged slamming coefficient for $0.00 < Vt/R < 0.03$ in figure 5.14 shows that the dependence on time step size is small. Zhu (2006) studied the same problem using a CIP based code, and did not achieve convergence for the very initial phase, but she did obtain convergence for the averaged C_s. This average is close to the results presented in figure 5.14. The non-convergent behavior is not found in CIP simulations by Vestbøstad (2009), nor in the present computations. As expected, the force fluctuations caused by the meshing have larger amplitude for coarser mesh, and applying a floating average with span width Vt/R=0.001 shows that the difference between the different time steps is small (see figure 5.12)

Comparing the results from figures 5.11 to 5.14, it may be postulated that the accuracy of the solution is mostly independent on time step size as long as maximum CFL is less than 0.5 in the free surface area and 1 everywhere else. If the initial phase is of special interest, smaller time step should be used, and the free surface should be as sharply defined as possible. This may be obtained by using smaller elements than those used in mesh T2P25 and T3P25 in the area just under the center of the cylinder.

Figure 5.12 indicates that the T3P25 mesh with time step size $\Delta t = 1 * 10^{-7}$ s provides a converged solution, which is close to the results for both smaller time steps (i.e. $\Delta t = 5 * 10^{-8}$ s) and finer mesh (i.e. mesh T4P25). After the initial phase, i.e. for $Vt/R > 0.05$, the time step can be increased to $\Delta t = 2.5 * 10^{-7}$ s without decreasing accuracy.

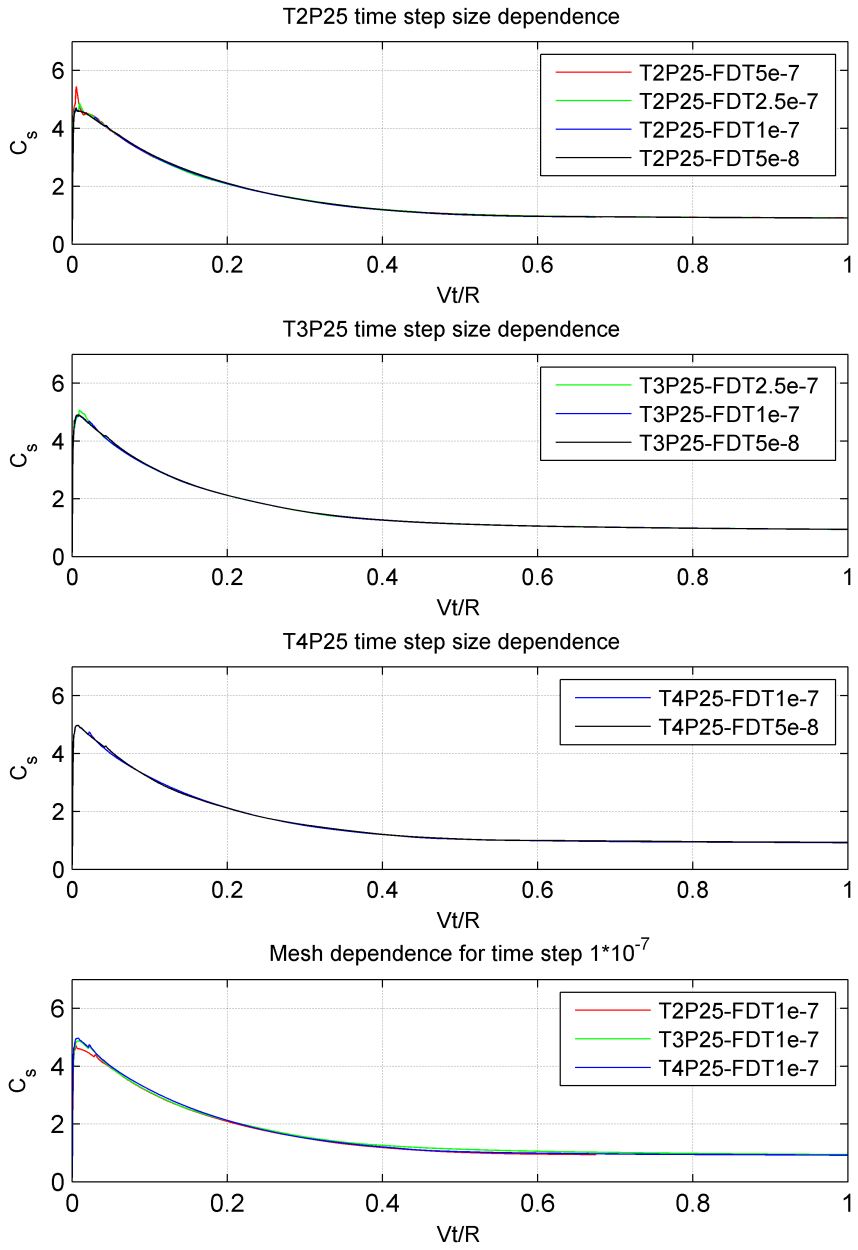

Figure 5.12: Slamming coefficient as a function of submergence for various mesh sizes and time steps. Smoothed using a span width Vt/R=0.001

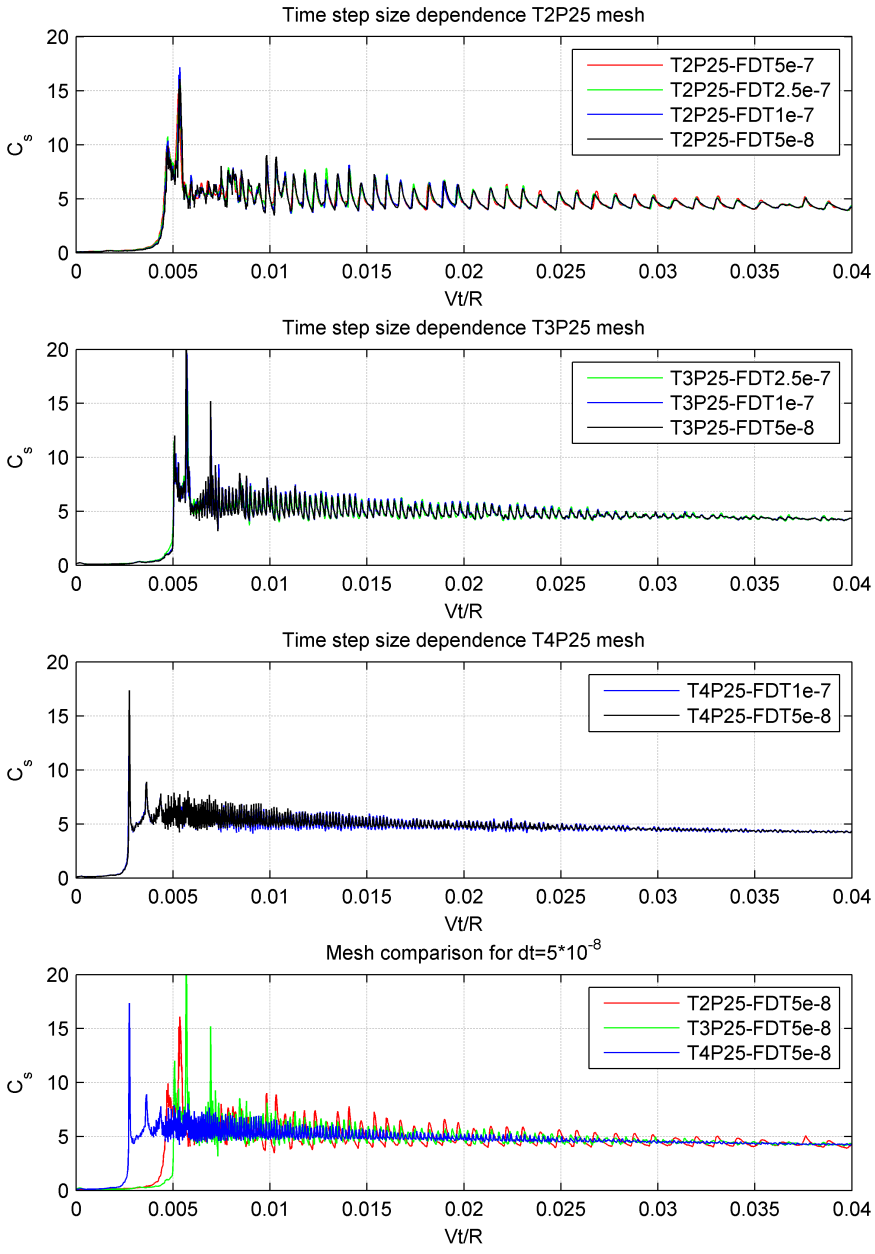

Figure 5.13: Slamming coefficient for initial phase of impact.

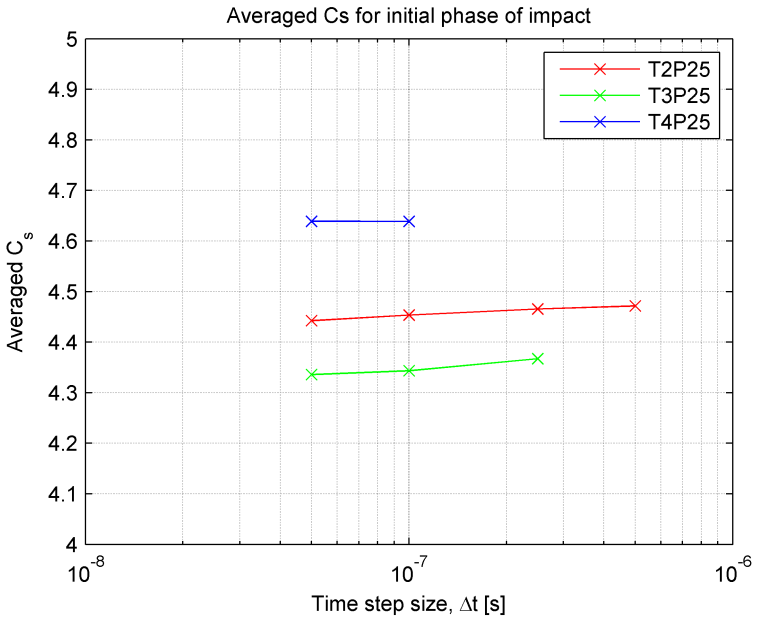

Figure 5.14: Averaged initial slamming coefficient for 0<Vt/R<0.03 as a function of time step size. The sharper free surface for mesh T4P25 causes the force peak to appear earlier, thus increasing the averaged Cs.

5.4 Mesh size from a practical point of view

The above simulations have been focusing on how to obtain the highest accuracy possible, without much concern on computational cost. The reader may already have noticed that several of the mesh and time step values above are not practical for use in the industry, where one usually will accept a certain level of errors if the computational cost is reduced. As an example, the computational cost for mesh T4P25 is more than 100 times the cost of using mesh T1P25. Expanding this into 3D further increases this difference. This is not only caused by the increased number of cells, but also the required reduction of the time step size. Knowing that a simulation with the T4P25 mesh takes several days to compute on a high performance computing (HPC) cluster, this mesh is clearly of little interest for the industry. For a complex 3D simulation the use of this mesh is beyond reach for all practical purposes.

Aiming at finding a more efficient mesh for engineering practice, it has been found that a modification of mesh T1P25 perform satisfactory for most practical cases. In this new mesh the number of prism layers is reduced to one on the upper half, and the 0.625 mm trimmer cells close to the prism layer has been replaced by 1.25mm cells.

The domain size has also been reduced to the D2 domain from section 5.1. These changes reduce the number of elements from 46 062 to 30 428. In addition to the reduction of computational cost by the decrease in number of cells, larger time steps may be used while still having the same CFL numbers due to the increased size of each cell.

This new mesh is called T0P15.

The calculated slamming coefficient for this mesh is compared to the results for meshes T2P25 and T4P25 in figure 5.15 and shows good agreement for $Vt/R > 0.05$. During the initial phase, a dip is found in the force record the coarse mesh types. This is caused by the meshing just under the center of the cylinder and that the free surface is not sharply defined in VOF simulations. A refinement of the mesh in this area reduces this dip.

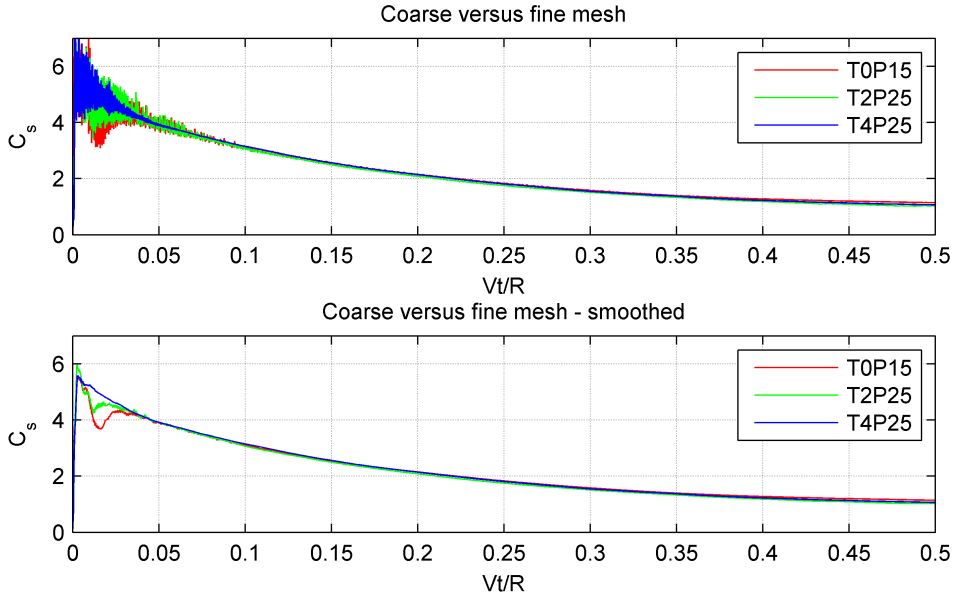

Figure 5.15: Slamming coefficient as a function of non-dimensional submergence for mesh T0P15, T2P25 and T4P25. The dip in C_s during the initial phase is caused by the meshing just under the center of the cylinder and that the free surface is not sharply defined in VOF simulations

For the T0P15 mesh, a time step size of $1 * 10^{-6}$ s has been found appropriate. With this time step size, the simulation takes about 2h15min on a regular PC with four cores running at 3.7GHz. To reduce computational cost further, the time step may be increased for $t > 0.005$ s. By monitoring the CFL number and changing the time step size accordingly during the simulation, the total time of performing

one simulation may be reduced to just over one hour.

5.5 Discretization and numerical parameters

Before CFD simulations are performed, many choices have to be taken. With the solution domain divided into a finite number of control volumes, the type of discretization defines how the integral form of the governing equations are transformed to a set of linear algebraic equation. For the implicit solver used in this thesis, STAR-CCM+ offers first- and second-order discretization schemes. The effect of choosing different schemes have been investigated for the T3P25 mesh. This section presents some basic information about these choices, for further information the reader is referred to CD-adapco (2012), from which the information in this section is adapted.

For illustrative purposes, the transport of a simple scalar, ϕ, is used (as opposed to a tensor or vector). The transport of this scalar is represented by the *generic transport equation for scalar quantities* (equation 4.4), which may be discretized as follows on a cell-centered control volume:

$$\frac{d}{dt}(\rho\phi V) + \sum_f [\rho\phi(\mathbf{v}\cdot\mathbf{n}S - G)]_f = \sum_f (\Gamma\nabla\phi\cdot\mathbf{n})S_f + (\rho b_\phi V) \tag{5.1}$$

In this equation, G is the grid flux due to mesh motion and f is each face of the control volume, $\mathbf{n}$ is the surface normal and $\mathbf{v}$ is the velocity vector. Γ is the diffusivity coefficient, $\mathbf{b}$ is the vector of body forces per unit mass and b_ϕ represents sources or sinks of ϕ. From left to right, the terms are the transient term, the convective flux, the diffusive flux and the volumetric source term.

5.5.1 Temporal discretization

STAR-CCM+ offers two different temporal discretization options for the transient term of the transport equation for the implicit unsteady solver used in this thesis: first- and second-order.

First-order scheme The first-order scheme is also known as Euler implicit, and discretizes the unsteady term by using the solution calculated at the present time step together with the previous time step:

$$\frac{d}{dt}(\rho\phi V) = \frac{(\rho\phi)_{n+1} - (\rho\phi)_n}{\Delta t} V \tag{5.2}$$

where $n+1$ indicates the present time step and n is the previous time step.

Second-order scheme The second-order scheme discretizes the unsteady term based on the solution at the present time, together with the solution at two previous levels:

$$\frac{d}{dt}(\rho\phi V) = \frac{3(\rho\phi)_{n+1} - 4(\rho\phi)_n + (\rho\phi)_{n-1}}{2\Delta t}V \tag{5.3}$$

This second-order scheme is normally more accurate than the first order scheme, but is more time consuming and less stable (the CFL number to should be less than 0.5 everywhere in the domain due to stability restrictions). For the first step of a simulation, first order discretization is always used since only two time steps are available.

5.5.2 Convection scheme

The convection term in equation 5.1 is discretized as follows:

$$[\rho\phi(\mathbf{v}\cdot\mathbf{n}S - G)]_f = (\dot{m}\phi)_f \tag{5.4}$$

where $\dot{m}_f$ is the mass flow over cell face f. Several schemes are commonly used for discretizing this equation, and two are available for the user of STAR-CCM+ to choose from; first- and second-order upwind:

First-Order Upwind For this scheme, the convective flux is calculated as:

$$(\dot{m}\phi)_f = \begin{cases} \dot{m}_f\phi_0 & \text{for } \dot{m}_f \geq 0 \\ \dot{m}_f\phi_1 & \text{for } \dot{m}_f < 0 \end{cases} \tag{5.5}$$

Where ϕ_0 and ϕ_1 are the scalar values in cell 0 and 1, respectively. This scheme introduces a dissipative error which stabilizes the solution, but has the negative effect of "smearing" discontinuities, such as the free surface. Normally this scheme is used if a solution using the second-order scheme is unobtainable.

Second-Order Upwind The difference between the first- and second-order upwind scheme is that for the second order, ϕ_0 and ϕ_1 in equation 5.5 are replaced by the value of the scalar on the cell face, calculated using linear interpolation from the cells on either side of the face. The advantage of this scheme over the first-order scheme is that is more accurate, and also provides sharper discontinuities.

The convection scheme is to be chosen two places in the STAR-CCM+ physics settings, both under the *Segregated flow*[5.2] node and in the *Volume of Fluid (VOF)* node, the first defining the convection discretization to be used for the segregated flow solver, and the latter is used for convection of the volume fraction scalar α defining the properties of the fluid in each cell as discussed in section 4.2.1.

Testing have shown that using first order-discretization for the VOF solver introduces a significant smearing of the free surface, even at very low CFL numbers. The order of the segregated flow solver and the temporal discretization does not have any effect on this smearing. (See figure 5.16). By using first-order discretization for the segregated flow solver and a second order VOF model this smearing is reduced.

5.5.3 Other numerical parameters

The under-relaxation factors governs the extent to which the newly computed solution in each iteration supplants the old solution, and are chosen independently for pressure and velocities during the setup of the analysis. The factors are always between 0 and 1 and choosing a factor close to 0 gives a solution of the next iteration that is governed by the previous iteration, whereas for a factor close to 1, the solution of next iteration will be governed by the computed value in the present iteration. For more information about these factors, the reader is referred to CD-adapco (2012).

The number of iterations defines how many iterations that are performed by the solver for each time step, and must be carefully chosen. If the number of iterations is too low, the solution will not converge. If the number is too high, this will result in the simulation taking more time than necessary.

By testing various under-relaxation factors and number of iterations, it has been found that 5 inner iterations per time step, together with under-relaxation factors of 0.8 and 0.2 for the velocity and pressure, respectively, provided an efficient solution for most cases. However, more inner iterations and lower under-relaxation factors were needed in some simulations.

[5.2]The segregated flow model solves the flow equations (one for each velocity component and one for pressure) in an uncoupled manner

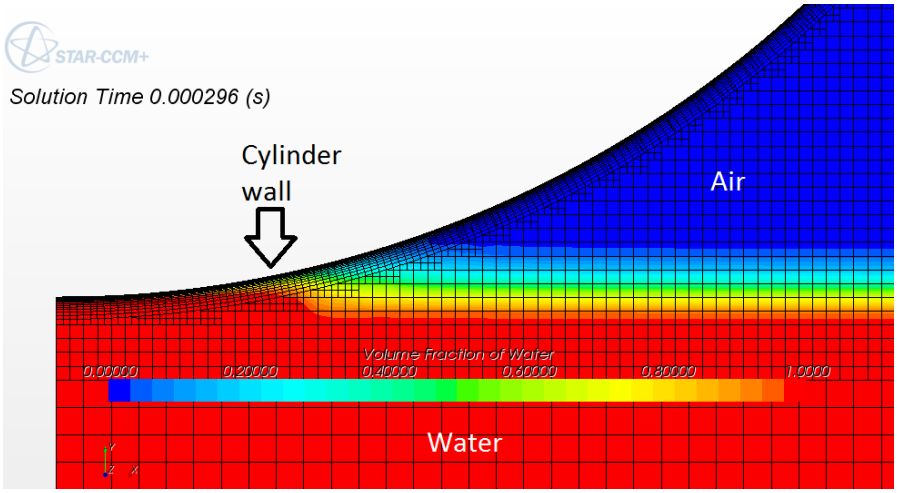

(a) Simulation using first order convection discretization for both segregated flow and VOF combined with first order temporal discretization

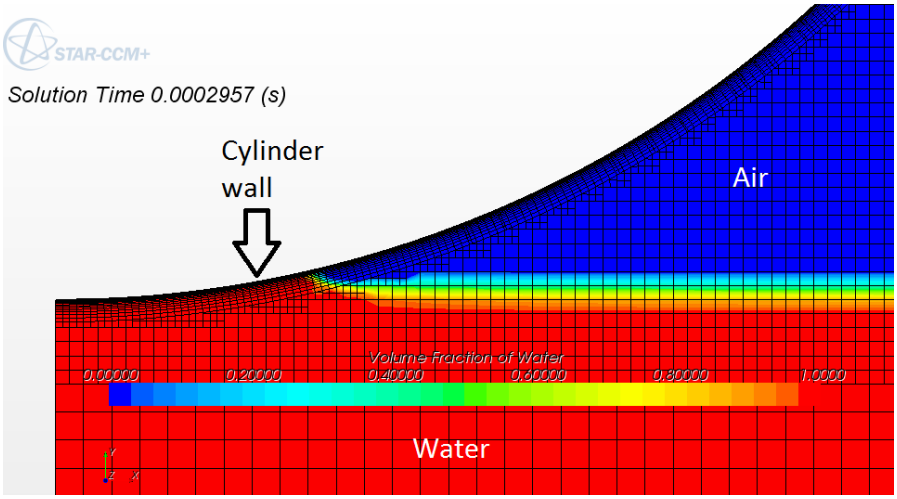

(b) Simulation using first-order convection discretization for segregated flow, second-order for the VOF solver, and first-order temporal discretization

Figure 5.16: Illustrations showing the smearing effect on the free surface for first order convection scheme used for the VOF formulation

5.5.4 Results

Performing the same simulation using different schemes showed little difference, as long as the jet is formed and the free surface is found sharp in the visual observation. Choosing second-order temporal discretization and/or second order segregated flow solver reduced the stability of the solution. In most cases this could be solved by increasing number of inner iterations and decreasing under-relaxation factors. For mesh T3P25, convergence was not achieved at certain time steps for the case with second order segregated flow solver even with increased number of inner iteration and decreased under-relaxation factors. The slamming coefficients for a selection of different schemes are given in figure 5.17 for both of the analyzed meshes, where these unconverged time steps can be seen as the spikes at $Vt/R > 0.4$.

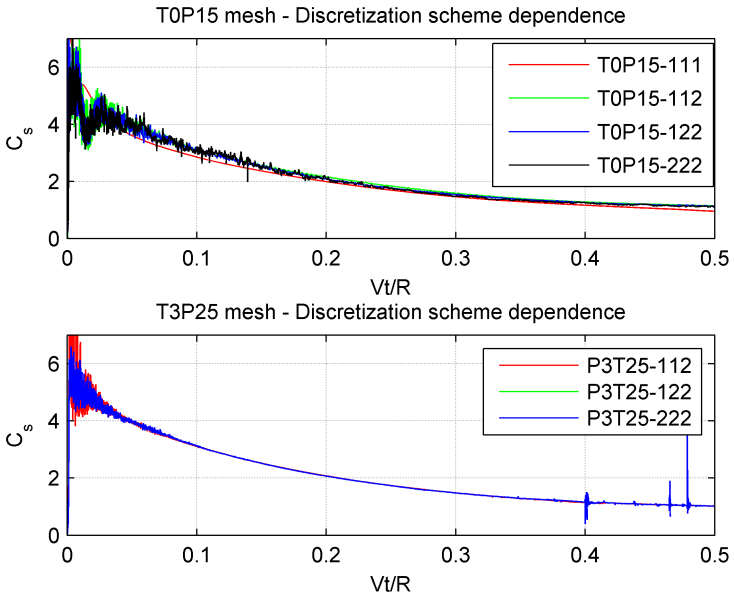

Figure 5.17: Slamming coefficient as a function of submergence Vt/R for various mesh sizes and discretization schemes. Naming convention: mesh-xyz, x=order of segregated flow scheme, y=order of temporal discretization scheme, z=order of VOF solver scheme

The first-order scheme for the segreated flow solver, first-order temporal scheme and second-order VOF treatment is considered most suitable for the problems in this thesis as summarized in table 5.9.

	Parameter	Value
Physics - Segregated Flow	Convection	1st Order
Physics - Volume of Fluid	Convection	2nd Order
Solver - Implicit Unsteady	Temporal Discretization	1st Order
Solver - Segregated Flow	Velocity Under-Relaxation Factor	0.8
	Pressure Under-Relaxation Factor	0.2
Solver - Segregated VOF	Under-Relaxation Factor	0.9
Stopping Criteria	Maximum Inner Iterations	5

Table 5.9: Recommendations for discretization settings and numerical parameters.

5.6 Turbulent versus laminar flow model

When studying fluid dynamics one needs to determine the type of flow. STAR-CCM+ provides the user with turbulent, laminar and inviscid flow models, and based on the work by Johannessen (2012), a laminar flow model was chosen in the above sections. During the water impact, the downward velocity of the cylinder is 5 m/s, implying a Reynolds number of approximately 10^6, which means that the effects of turbulence should be investigated.

An analysis has been performed to determine the effect of choosing a turbulent compared to a laminar flow model. A shear driven two-layer $k - \epsilon$ RANS turbulence model of second order is used, combined with the "Two-Layer All y+ Wall Treatment" model.[5.3] The reader is referred to CD-adapco (2012) pages 3127-3407 for more information regarding turbulence modeling in STAR-CCM+.

Discretization Both the T0P15 and T3P25 meshes have been analyzed, and as for the laminar flow analyses presented above, the effect of discretization order should be investigated. Figure 5.18 compares the vertical force and maximum pressure on the cylinder for first- and second-order discretization for the turbulent simulations using mesh T3P25. The same results as for laminar flow are found for the turbulent flow model; decreased stability for second-order convection and little change in calculated slamming coefficient. Differences in vertical force and maximum pressure for the two discretization methods are considered negligible for all practical applications, hence first-order temporal and segregated flow convection schemes may be used for the turbulent flow model, combined with a second-order VOF solver.

[5.3] y+ is the non-dimensional wall distance and determines the assumptions used for the turbulence model close to the body

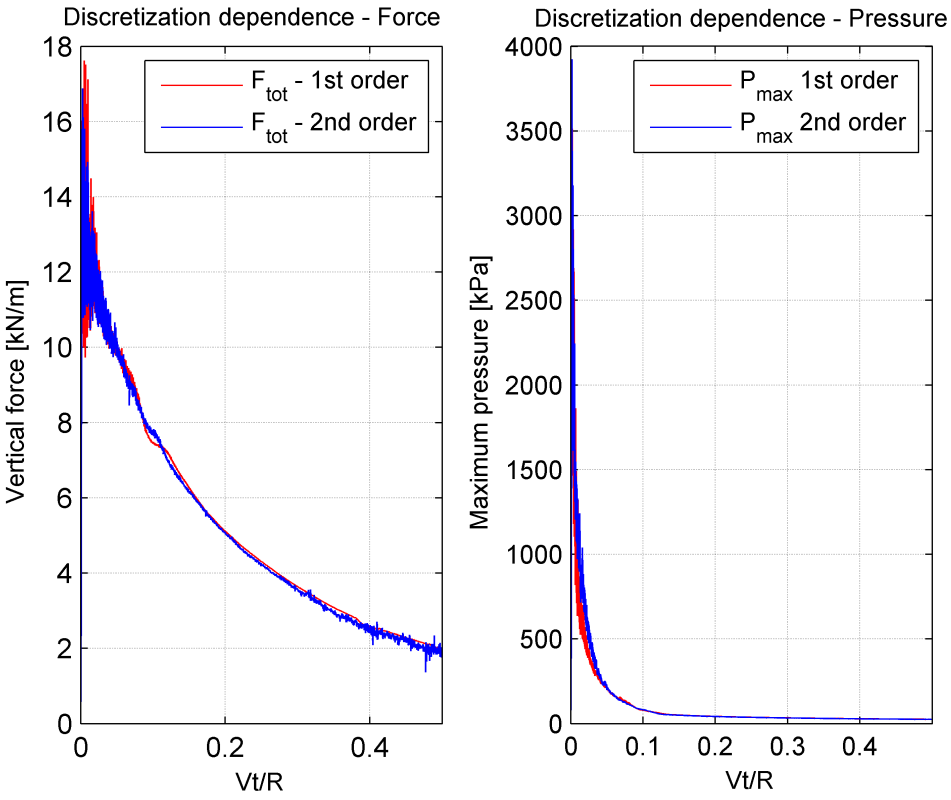

Figure 5.18: Effects discretization order of segregated flow solver and temporal discretization for turbulent flow model. 2nd order VOF model is chosen for both models to reduce "smearing" of the free surface.

Results The calculated slamming coefficients for both laminar and turbulent flow models are plotted in figure 5.19 for a coarse mesh (T0P15) and a finer mesh (T3P25). Little difference is seen in the force records, hence the laminar flow model is considered sufficient for the tested problem. The plots also show the contribution from the shear force on the total vertical force. It can be seen that this contribution is small, and accounts for only about 1% of the total vertical force. For the finer mesh, the shear force is larger compared to a coarse mesh, and the contribution is also larger for the turbulent simulations (which is to be expected).

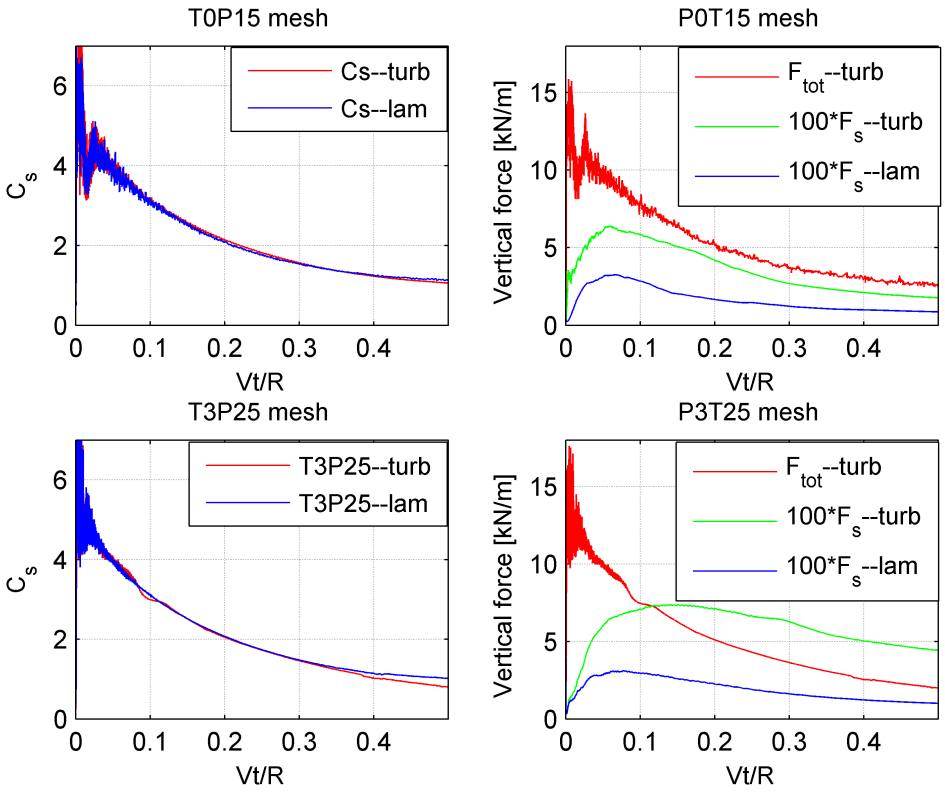

Figure 5.19: Laminar versus turbulent flow model. Calculated slamming coefficient, Cs (left) and contribution from shear force on the total vertical force (right) for mesh T0P15 (top) and T3P25 (bottom)

5.7 Inviscid flow model

By assuming inviscid flow, one neglects the viscous effects in the equations of motions. This results in the use of the Euler equations, as opposed to the Navier–

Stokes equations used for viscous flows. Approximating the flow as inviscid reduces the computational cost, since boundary layers and other viscous effects no longer has to be resolved.

Since the viscous force contribution to the vertical force is small compared to the pressure forces, there is reason to believe that an inviscid model may be sufficient for water impact problems. A simulation has therefore been performed using the inviscid flow model on the T0P15 mesh.

It has been found that choosing an inviscid flow model increases the CFL numbers during the initial phase. The reason for this is that the velocities close to the cylinder wall are larger than for viscous flow due to the lack of no-slip boundary condition.

The jets during the initial phase seen in viscous simulations are also found for the inviscid model. However, these jets do not separate from the cylinder surface for in the inviscid simulation, and instead follows along the side of the cylinder causing an unnatural flow pattern (see figure 5.20).

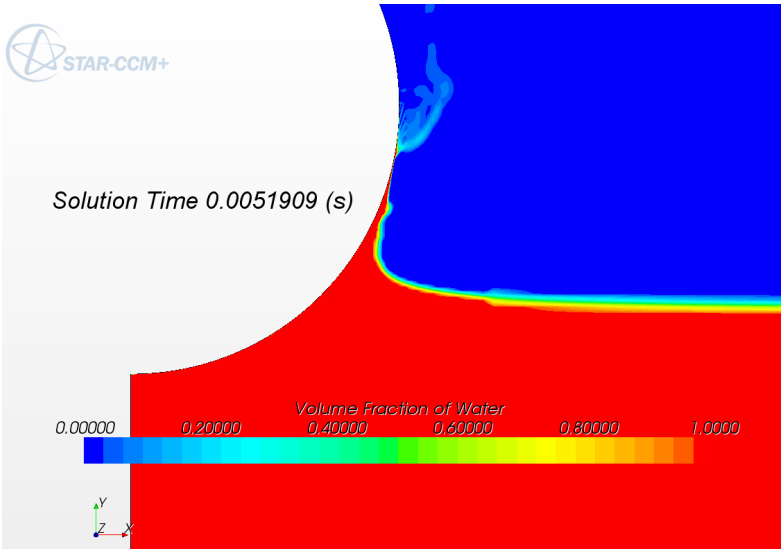

Figure 5.20: Free surface deformation for inviscid flow model at $Vt/R = 0.26$. T0P15 mesh.

The slamming coefficient for the inviscid simulation is plotted in figure 5.21, together with the results from laminar and turbulent simulations. The figure shows that the difference between the models is small during the initial phase, and increases with increased submergence. This indicates that for the initial phase, an inviscid flow model may be used with high accuracy, but for later phases of water impact, a laminar or turbulent flow model should be used.

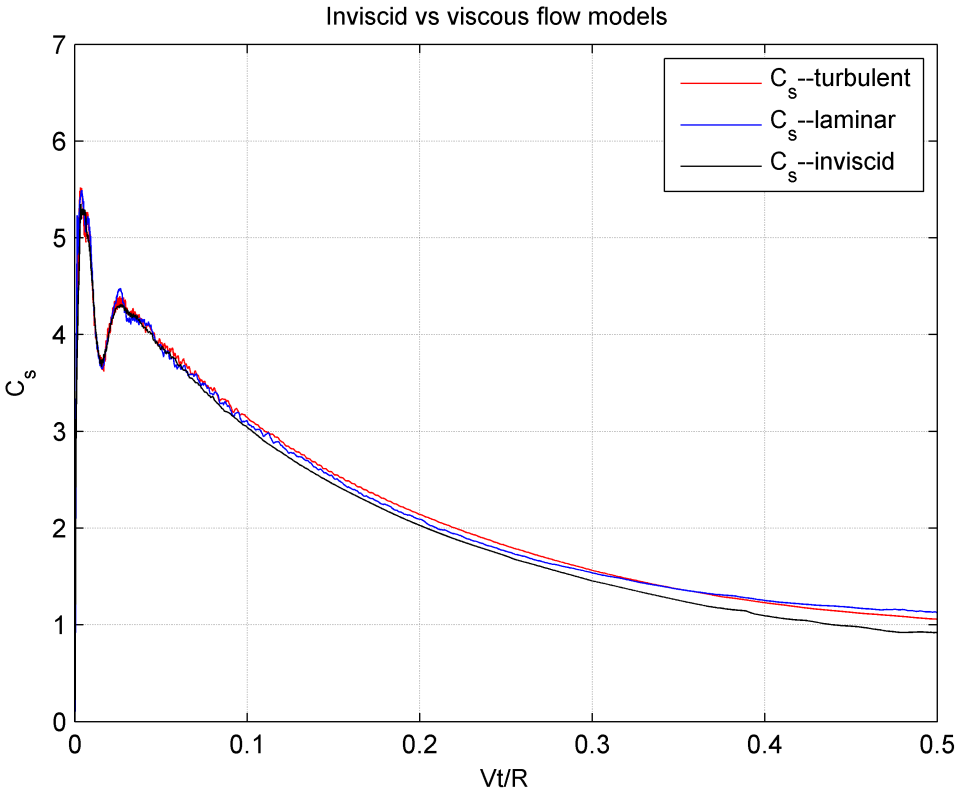

Figure 5.21: Comparison of C_s from laminar, turbulent and inviscid flow models for the T0P15 mesh.

Regarding computational efficiency, it has been found that applying an inviscid flow model reduces the CPU-time for each time step with approximately 20% compared to the turbulent flow model and up to 10% compared to a laminar flow model. Considering the need for smaller time steps for the inviscid flow model (assuming the same mesh is used), the total computational cost is actually increased compared to viscous flow models. This shows that choosing an inviscid flow model does not necessarily result in a reduction of the computational cost if the mesh is the same and created with viscous flows and ability to resolve boundary layers in mind. To increase efficiency, it is believed that choosing inviscid flow model combined with a coarser mesh close to the cylinder will give reasonable results during the initial phase. For the later phases of impact, a viscous flow model is needed to correctly predict the free surface and the forces acting on the cylinder.

Since both the initial and later phases of impact is to be studied in this thesis, as well as free surface deformations, all simulations in the next chapters are performed using viscous flow models.

5.8 Compressibility effects

During water impact of blunt bodies such as cylinders, compressibility effects for both air and water may influence the results. Air compressibiliy may be of interest if air cushions are generated and the rise pressure before the impact is to be considered. Water compressibility on the other hand, may be of interest for a short period after impact, and was studied by Hagiwara and Yuhara (1976), who showed experimentally that the maximum pressure at impact is limited by the acoustic pressure, $p_{max} = \rho C V_0$ (see section 3.1). For the problem simulated in this chapter, this means that the maximum pressure is:

$$p_{max} = \rho C V_0 = 1000 \frac{\text{kg}}{\text{m}^3} * 1500 \frac{\text{m}}{\text{s}^2} * 5 \frac{\text{m}}{\text{s}} = 7500 \text{kPa} \tag{5.6}$$

This result is supported by Korobkin and Pukhnachov (1988), who studied the influence of liquid compressibility during the initial-impact stage. The study was based on an asymptotic model as the Mach number tends to zero, and they also found that, for impact governed by the acoustic pressure, the pressure decreases at the initial impact point after a very short time, and travels with the spray root.

The propagation velocity of the spray root and other relevant velocities should also be considered when investigating the effect of compressibility. Water can

normally be considered incompressible if the Mach number is less than 0.3, i.e. if the water velocity is less than 450 m/s.

According to Korobkin and Pukhnachov (1988), the length of the time period where the velocity exceeds the local sound velocity in the fluid can be calculated as $t_* = RV/2c_0^2$. With V=5 m/s and R=0.10 m, this results in $t_* = 1.1 * 10^{-7}s$. Even with compressibility effects present for several times this period (i.e. for Mach numbers <1), the duration is less than 1 μs. In practice, this is merely of academic interest, as the impulse is small due to the short duration. Also, offshore structures are not perfectly stiff, and flexure of the body will reduce this pressure peak.

5.9 Conclusion

From the domain size study it is found that a small domain overpredicts the vertical force on the cylinder. Due to the large elements far from the cylinder, the increase in computational cost for increased domain size relatively small. The mesh size analysis indicates that the mesh size is important during the initial phase of impact, implying that a fine mesh should be used in analyses where this phase is important. The computational cost for such a mesh is high, and it is believed that simulations on a this mesh are mostly of academic interest. For practical use, a coarser mesh has been found. The use of this coarse mesh introduces some uncertainty during the initial phase, but after this the results show good agreement with results obtained on finer meshes. The decrease in computational cost is significant.

It is also found that the influence of time step is small, as long as the CFL number is less than 0.5 on the free surface, and not much more than 1 anywhere in the domain. For larger time steps, "smearing" was found on the free surface, which leads to unrealistic flow patterns.

The calculated slamming coefficient, C_s is plotted in figure 5.22, together with a selection of other methods. The most widely used model in the offshore industry is the empirical line by Campbell and Weynberg (1980), but it should be noted that this line is a based on experimental data with large uncertainties. Also seen in figure 5.22 is the line proposed by Miao (1989). We can see that this line predicts larger slamming forces during the initial phase of impact and has a steeper decay than the Campbell & Weynberg line. With a result between the two lines, the CFD simulations are believed to be close to the reality and that STAR-CCM+ can be used to predict impact loads on a 2D cylinder entering a flat free surface

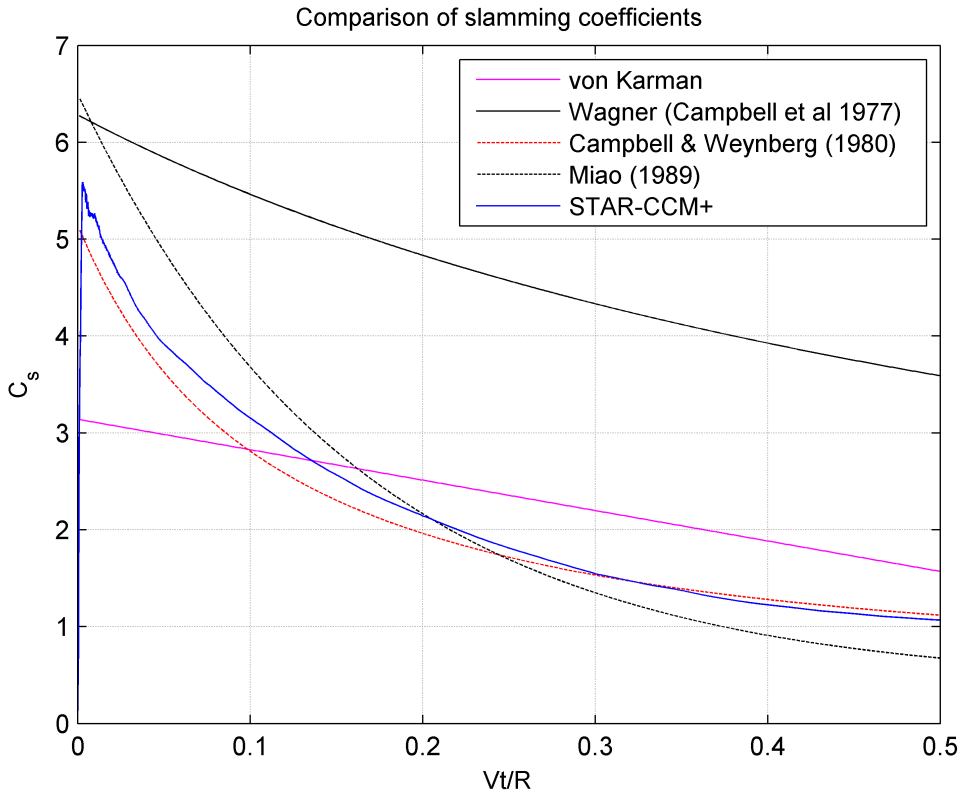

Figure 5.22: Slamming coefficient from STAR-CCM+ (smoothed, here represented by the T4P25 mesh) compared to methods by von Karman (1929), the Wagner line presented by Campbell et al. (1977), and empirical lines by Campbell and Weynberg (1980) and Miao (1989)

with constant velocity. The accuracy of the solution can not be determined from the above analyses, due to the uncertainties in the experiments. This is further treated in chapter 6, where the penetration depth of two different free falling cylinders has been investigated and compared to experimental data and other numerical methods.

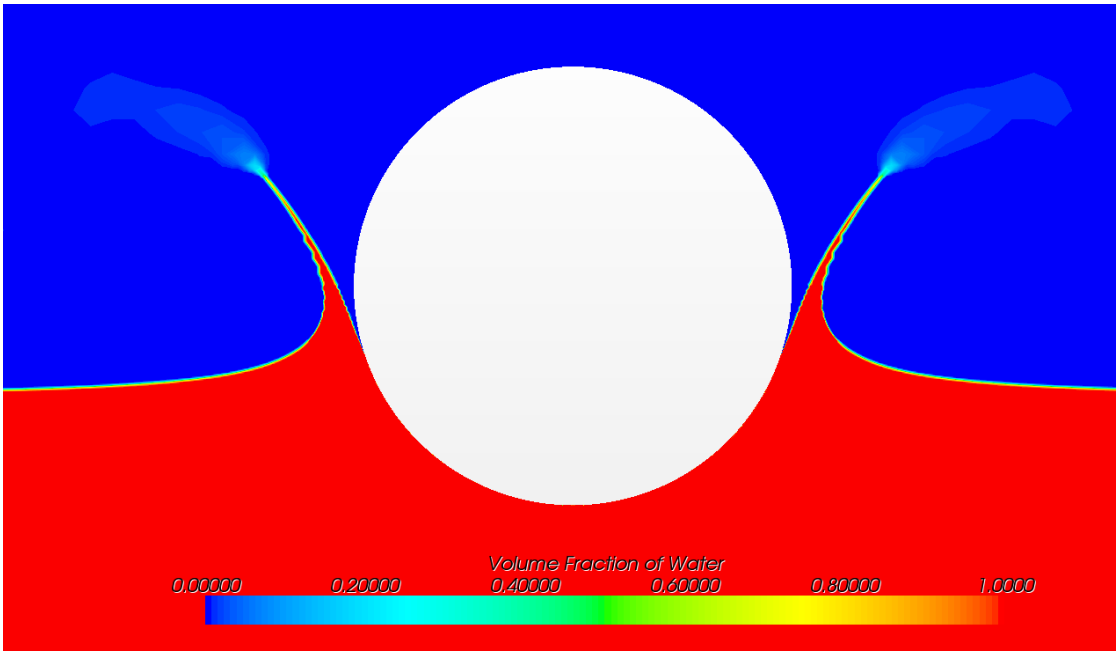

Figure 5.23: The free surface at Vt/R=0.5. Note the jets separating from the cylinder surface. Laminar flow model, T3P25 mesh, and first order discretization (second order for VOF solver).

6 Free fall drop test of 2D circular cylinder

Most experiments available for validation of CFD results are performed by measuring the time-dependent vertical force on the cylinder directly with force transducers or by integration of measured pressure. The main drawback of this method is that it is prone to errors during the experiment, such as sensor vibration, gauge slip, and vibrations in the testing rig. One example of this is the experiments presented by Campbell and Weynberg (1980), where the slamming coefficient has a dominant oscillation at about 550 Hz, and smaller vibrations at several other frequencies. Although vibrations often may be filtered out, they do cause an uncertainty in the data. It is also normal procedure to neglect effects of buoyancy and velocity variation when calculating the slamming coefficient. These and other sources of error are reflected in the fact that different experiments show different behavior for the slamming coefficient, as shown in chapter 3.

The errors due to sensor and testing rig vibration are dominant during the initial phase, whereas buoyancy and velocity reduction are more important during the later stages of impact. This means that there are often large sources of errors during the entire experiment.

When it comes to validation of CFD results, such errors introduce uncertainties regarding the accuracy of the method. In chapter 5, it was shown that STAR-CCM+ predicted slamming force close to the empirical lines by Campbell and Weynberg (1980) and Miao (1989). But since it is not known which of these lines are most correct, more simulations are needed to identify the accuracy.

The free fall drop test by Greenhow and Lin (1983) has therefore been used for further testing STAR-CCM+. In their experiments, two cylinders of different mass were dropped onto a flat free surface, capturing the position of the cylinder and deformation of the free surface using a high-speed camera. This reduces the complexity of the experiment compared to the experiments presented by Campbell and Weynberg (1980) and Miao (1989), hence the number of possible sources of errors is reduced.

6.1 Description of the analysis

To compare CFD simulations directly to experimental results, free fall simulations with a half buoyant (HB) and a neutrally buoyant (NB) cylinder have been performed. The radius of each cylinder is $R = 5.5$ cm, which is equivalent to the experiment presented by Greenhow and Lin (1983). The cylinders are dropped from a height of 0.5 m between the center of the cylinder and the free surface, and the cylinders hit the surface after approximately 0.3 s.

Motion is modeled using the dynamic fluid-body interaction (DBFI) solver in STAR-CCM+, which calculates the motion of the cylinder based on the mass, center of gravity, starting position, starting velocity, hydrodynamic forces etc. The simulation has been performed using a laminar flow model.

The mass of each cylinder is:

- Half buoyant: m=4.737 kg/m
- Neutrally buoyant: m=9.475 kg/m

The free fall experiments have also been simulated numerically by Zhu (2006) using a Constrained Interpolation Profile (CIP) CFD method, and Sun (2007) using a fully non-linear BEM method. In addition to the experimental data, the results from STAR-CCM+ are compared to these results.

6.2 Domain size and mesh

The mesh is adapted from mesh T0P15 in chapter 5, and both cylinder and mesh is scaled to 55% of its original size. This way, the non-dimensional mesh size is identical to T0P15. A refinement has been added in the area under the cylinder to ensure that the free surface is sharp and to reduce the dip seen in the simulation on coarse meshes in chapter 5. Refinement is also added at the side of the cylinder to study the shape of the cavity for comparison with photographs of the experiments. The size of the mesh at the side of the cylinder is believed to have little impact on the hydrodynamic force, thus fewer elements can be used in this area if only the force on the cylinder, and not the shape of the cavity, is of interest.Total number of cells is 39 631, an increase of about 30% from the initial P0T15 mesh.

6.3 Impact velocity

The air drag resistance in free fall for the cylinder is small, hence the computational cost can be significantly reduced by calculating the velocity of the cylinder at a given (small) elevation above the free surface, and use this as starting point for the simulation. When the bottom of the cylinder is 5 mm above the undisturbed free surface, the velocity is:

$$V = \sqrt{2 * 9.810[\mathrm{m/s^2}] * 0.440[\mathrm{m}]} = 2.938[\mathrm{m/s}] \tag{6.1}$$

The time to fall from the initial position to 5 mm above the initial free surface is:

$$t = 2.938[\mathrm{m/s}]/9.810[\mathrm{m/s^2}] = 0.300[\mathrm{s}] \tag{6.2}$$

6.4 Time step size

The time step size has been varied during the simulation to reduce computational cost. Small time steps are needed during the initial phase, typically $\Delta t = 5 * 10^{-7}$ s, increasing to $\Delta t = 1 * 10^{-5}$ s later in the simulation. All time steps have been chosen so that maximum CFL number is less than 0.5. In this chapter, no systematic study on choice of time steps size has been performed, following the analyses in chapter 5, showing that the dependence on time step size is small.

6.5 Discretization and numerical parameters

Based on the analyses performed in section 5, the first-order segregated flow solver and first-order temporal discretization has been chosen combined with second-order discretization for the VOF solver. In addition to laminar flow model, one simulation is been performed for the half-buoyant cylinder using a turbulent flow model, where a RANS $k - \epsilon$ turbulence model with *Two-Layer All y+* wall treatment is applied. 5 inner iterations and the default under-relaxation factors has given convergence for both laminar and turbulent simulations with sufficient reduction of the residuals.

6.6 Results

The main parameter in this test is the penetration depth for the bottom of the cylinder. In addition, the free surface deformation is compared to photographs

from the experiment by Greenhow and Lin (1983). Figure 6.1 shows the penetration depth versus time for both half buoyant (HB) and neutrally buoyant (NB) cylinder. The results obtained in STAR-CCM+ show relatively good agreement with CIP simulations by Zhu (2006) and nonlinear BEM results by Sun (2007). Fairly good agreement is also obtained between the numerical results and experimental data, except for the experimental penetration depth for neutrally buoyant cylinder at $t = 0.34$ s. However, Greenhow and Lin (1983) marked this measurement with a question mark in their publication as it deviates from the other data. The turbulent simulation performed for the half buoyant cylinder show deeper penetration compared to the laminar simulation, but the difference is relatively small. This is to be expected, since the simulations in chapter 5 showed a reduction in vertical force if turbulent flow model was used instead of laminar.

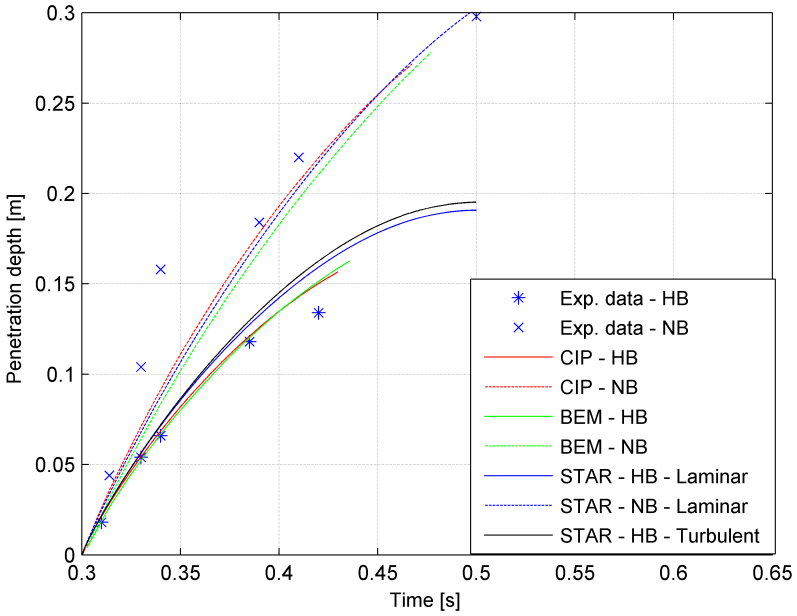

Figure 6.1: Penetration depth during water entry of half buoyant (HB) and neutrally buoyant (NB) cylinder. CFD results using STAR-CCM+ compared to experimental data by Greenhow and Lin (1983), CIP calculations by Zhu (2006) and nonlinear BEM simulations by Sun (2007). Water impact starts at time t=0.3[s]. The data point marked by a question mark was questioned in the original paper by Greenhow and Lin (1983)

Figures 6.3 and 6.4 show the free surface deformations for the two cylinders at selected time steps. The results from STAR-CCM+ show fairly good agreement with the pictures taken by Greenhow and Lin (1983), with jets thrown out from the side of the cylinder leaving the top of the cylinder dry even when $Vt > 2R$.

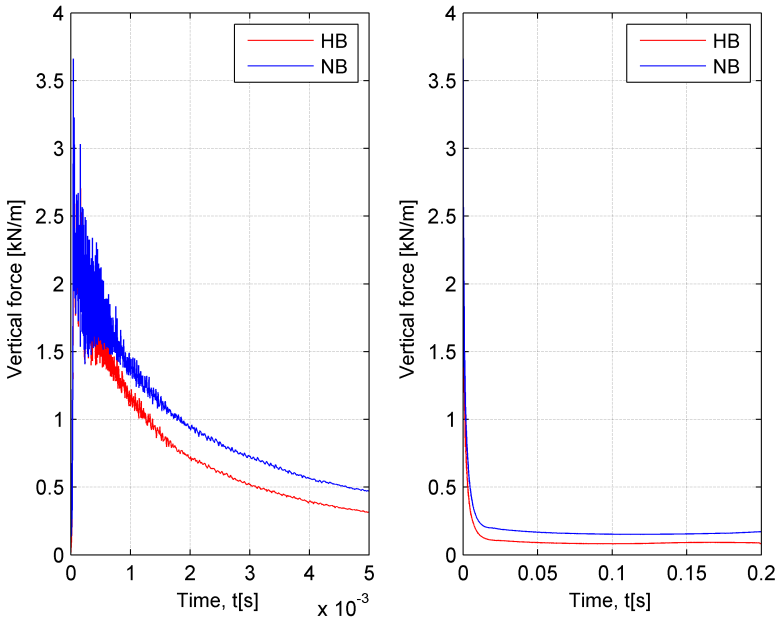

Figure 6.2: Vertical force on half buoyant (HB) and neutrally buoyant (NB) cylinder as a function of time after impact. Initial phase (left) and overview (right)

6.7 Discussion and conclusion

The above results show fairly good agreement to both numerical and experimental data, but there is a general trend that all the numerical methods estimate deeper penetration than the experiments for the half buoyant cylinder, whereas the simulations for neutrally buoyant cylinder underestimates the penetration depth. Studying the pictures in Greenhow and Lin (1983), it seems that the half buoyant cylinder impacts on the water surface at $t = 0.285$ s. If the timer is correct, this indicates that the drop height and impact velocity was lower than what is used in the numerical simulations. This may be the reason for the discrepancy in the results.

Also, in Greenhow and Lin (1983), the penetration depth plot starts with impact at $t = 0.300$ s. The difference between impact at $t = 0.285$ s and $t = 0.300$ s effectively leads to a time shift in the penetration depth plot, which may also be the reason for the discrepancy.

This uncertainty is supported by the fact that the original paper by Greenhow

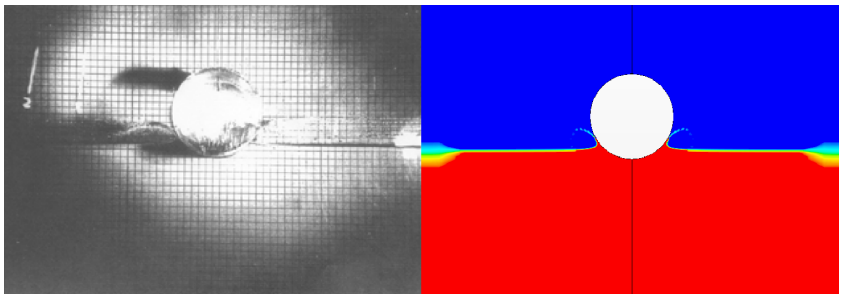

(a) t=0.305s

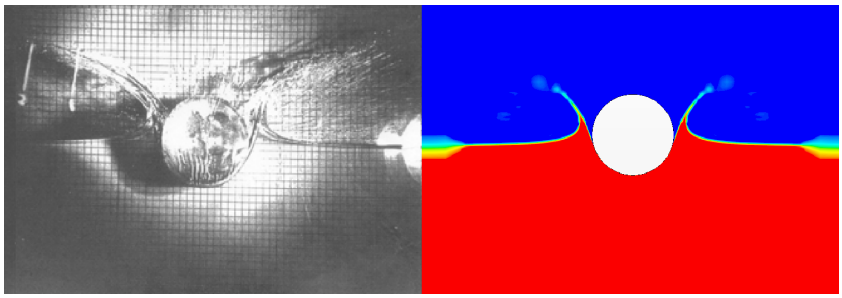

(b) t=0.330s

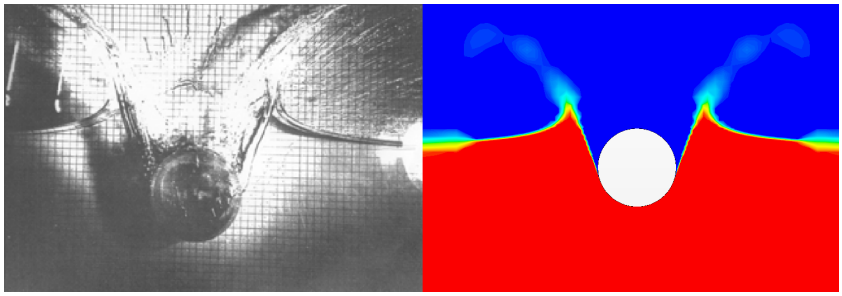

(c) t=0.385s

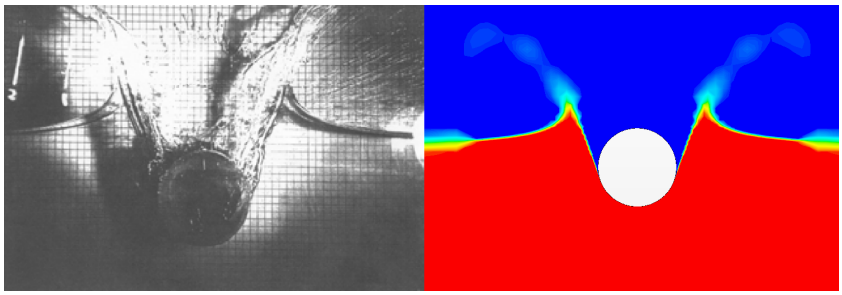

(d) t=0.420s

Figure 6.3: Free surface deformation during water entry of half buoyant cylinder. Radius R=5.5 cm. Experimental results by Greenhow and Lin (1983) (left) and STAR-CCM+ results (right) (Laminar flow model). Red areas are water, blue is air and the colors between indicates a mix of water and air.

.

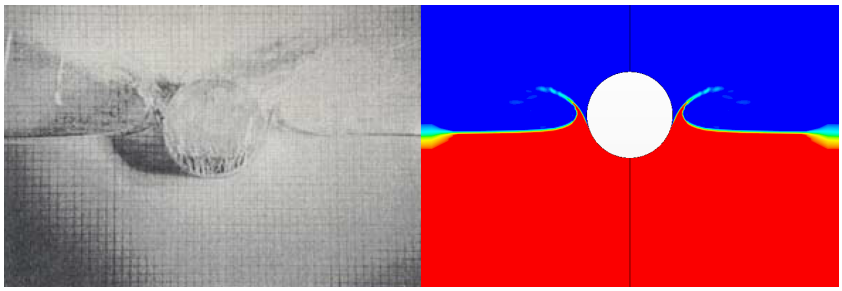

(a) t=0.315s

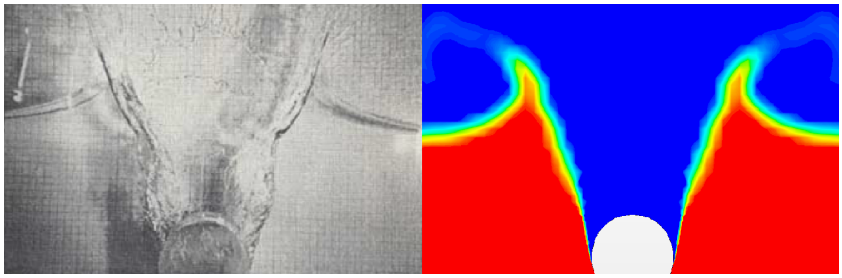

(b) t=0.410s

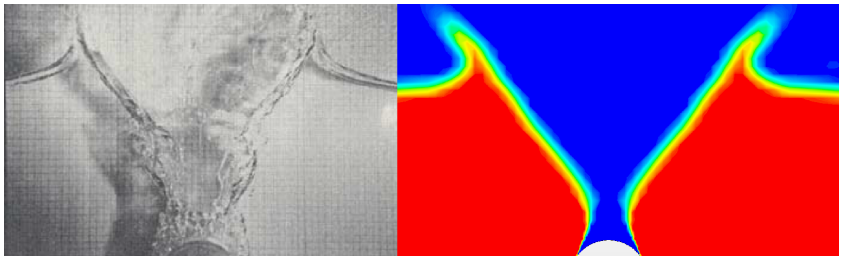

(c) t=0.500s

Figure 6.4: Free surface deformation during water entry of neutrally buoyant cylinder. Radius R=5.5 cm. Experimental results by Greenhow and Lin (1983) (left) and STAR-CCM+ results (right) (Laminar flow model). Red areas are water, blue is air and the colors between indicate a mix of water and air.

and Lin (1983) does not give any information on the drop height.[6.1] The height used in this thesis is based on the reported drop height in Zhu (2006).

To summarize, the results from STAR-CCM+ are fairly close to the experimental data and other numerical results, but possible errors regarding time of impact, drop height, and impact velocity means that no definite conclusion on the accuracy of the simulation can be drawn.

[6.1] Zhu (2006) and Vandamme et al. (2011) reports a drop height of 0.5 m from the center of cylinder, Sun (2007) reports a drop height of 0.5 m from the bottom of the cylinder.

7 Water entry of inclined cylinder

The previous chapters have focused on 2D analyses. Although 2D shapes are interesting from an academic point of view, it has been shown that for such simple geometries, the results are well predicted by empirical formulas.

The advantage of CFD comes when the geometry is complex and in all three dimensions. Examples of such problems are subsea templates being lowered trough the splash zone, water impact of free fall lifeboats and steep waves impacting on risers. In those problems, the empirical formulas and potential flow solutions are less accurate, and the two options available are model tests and numerical simulations using CFD.

3D simulations may also be used for validation of CFD results, as the force record often is smoother and more accurate for experiments where the cylinder hits the surface with an angle. One example of this is the experiments by Campbell and Weynberg (1980).

This chapter presents the simulation of an inclined cylinder with constant vertical velocity entering a flat free surface. The problem is of considerable interest for the offshore industry where platform leg cross members may be in the splash zone of incident waves, and therefore continuously entering and exiting the water. Other important applications are steep waves impacting on vertical structures such as risers or riser guide tubes. The results are compared to experimental data by Campbell and Weynberg (1980) and strip theory calculations.

7.1 Description of the analysis

As a part of their work, Campbell and Weynberg (1980) studied the water impact of an inclined cylinder impacting on a flat free surface and it was shown that the results for this experiment had less scatter than the experiments with horizontal cylinder.

The cylinder used in the experiments and the STAR-CCM+ simulation has a radius $R = 5.08$ cm and the length is 81.5 cm. Campbell and Weynberg (1980) studied impact angles between 0° and 8°, but in this thesis only the 8° impact is studied due to time constraints. The CFD results are compared to the experiments and strip theory (see Appendix B) using the non-dimensional inclined slamming coefficient;

$$C_{s\theta} = \frac{F_3}{\rho V^2 RL} \tag{7.1}$$

where F_3 is the vertical force acting on the cylinder and L is the length of the cylinder.

Campbell and Weynberg (1980) reported that the vertical velocity was not perfectly constant during the impact, with up to 5% deviation for experiments with 0° impact angle. No information is given for the inclined cylinder experiments, but the velocity was considered constant by Campbell and Weynberg (1980) when they calculated the slamming coefficients, and the influence of velocity variations on these coefficients are considered to be small. In the CFD simulation, constant vertical velocity of the cylinder V=2.60 m/s has been used, giving a Froude number of $F_N = 2.58$, which is the same as for the majority of the experiments.

The simulations with coarse meshes have been calculated on a personal computer with four cores running at 3.7 GHz and 16 GB of RAM. More time consuming simulations have been carried out on the Vilje HPC cluster at NTNU. Depending on mesh size, 16 to 144 cores have been used, all running at 2.6 GHz. Using 128 cores, a simulation with 5 million cells and 50 000 time steps can be calculated in about two days.

7.2 Domain size

The water tank used in the experiments by Campbell and Weynberg (1980) was 6 ft (1.83 m) long, 5 ft (1.52 m) wide and 4 ft (1.22 m) deep. For the CFD analyses,

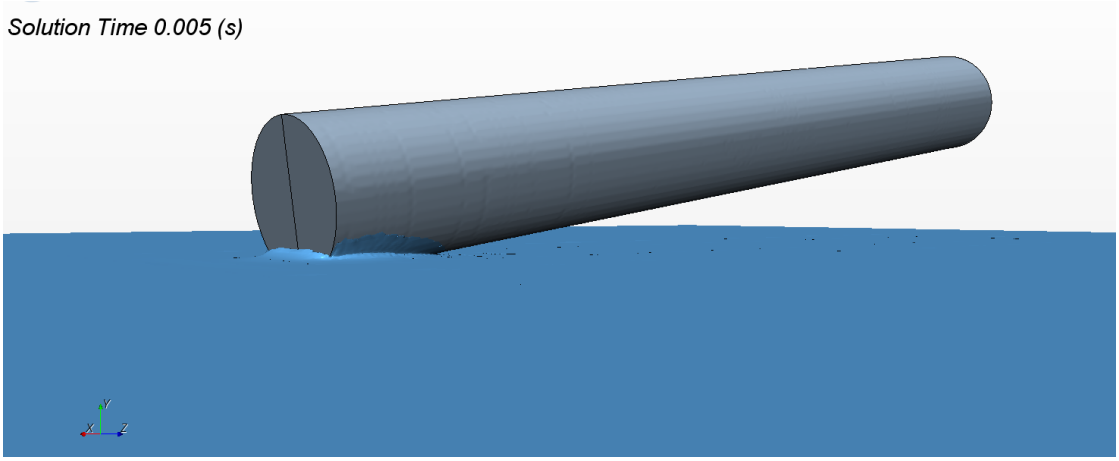

Figure 7.1: Illustration of cylinder and water surface 0.005 s after impact.

the same domain size has been used, but as there exist a symmetry plane through the cylinder center, only half the domain is modeled. No systematic testing of the domain size has been performed, but based on the analyses in section 5.1, this domain is assumed to be sufficiently large.

7.3 Mesh

The domain has been discretized using two grids, connected trough an *overset mesh interface*. All properties, such as pressure and velocities are transferred between the two regions on this interface, and there are two *regions*; one discretizing the entire domain, and a finer overlapping mesh close to the cylinder. This inner region is moving with the cylinder while the outer domain is fixed.

It is believed that a coarser mesh may be used for 3D analyses when the cylinder impacts on the water surface with an angle compared to horizontal impact as in the 2D simulations. The reason for this is that the problematic area under the cylinder now acts as a wedge in the third dimension reducing the loads during the initial phase.

Mesh size is important since a finer mesh generally gives more accurate results, but also is more computationally demanding. The increase of computational cost is partly because of the increased number of cells, and partly because of a reduction in time step size needed to keep the CFL numbers low enough. In addition, it was found by Johannessen (2012), and has also been experienced during the work on this thesis, that a finer mesh requires more inner iterations than a coarse mesh to

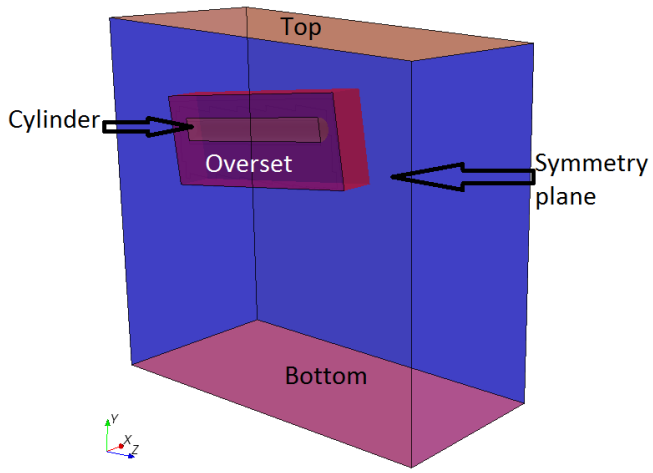

Figure 7.2: Geometry of test domain with outer domain and overset region containing the cylinder

achieve convergence.

Different mesh sizes have been tested, with time steps chosen so that the CFL number is <0.5 on the free surface and <1 everywhere in the domain. The coarsest mesh consists of approximately fifteen thousand cells, whereas the finest mesh has over five million cells.

The meshes tested have been named based on the total number of elements in the domain, see table 7.1. For two meshes having the same minimum trimmer cell size and different number of cells in total (53k versus 77k and 1805k versus 5046k), the difference is the distance from the cylinder wall to where the trimmer mesh size increases. Drawing parallels to the meshes in chapter 5, the 1805k mesh is equivalent to mesh T0P15 and 5046k resembles mesh T1P15.

The inclined slamming coefficients $C_{s\theta}$ for the different meshes are plotted as a function of non-dimensional submergence of the lower end of the cylinder in figure 7.4 together with results from experiments by Campbell and Weynberg (1980) and strip theory. It should be noted that the experiments and strip theory are correlated, since the empirical slamming coefficient used in the strip theory is partly based on these experiments (together with experiments at other impact

Mesh name	Number of cells cells	Number of prism layers	Minimum trimmer cell size [mm]
15k	14 795	0	4.00
53k	52 888	0	2.00
77k	77 428	4	2.00
116k	116 353	8	2.50
1805k	1 804 501	15	1.25
5046k	5 046 477	15	1.25

Table 7.1: Mesh sizes analyzed for 3D simulation.

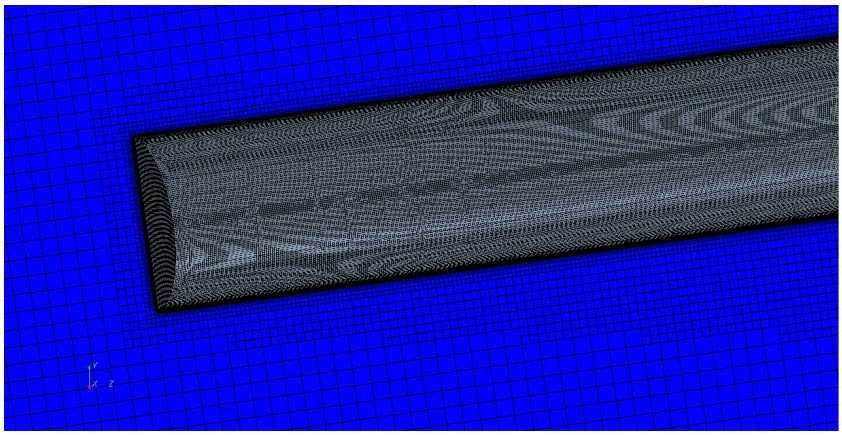

(a) 1805k

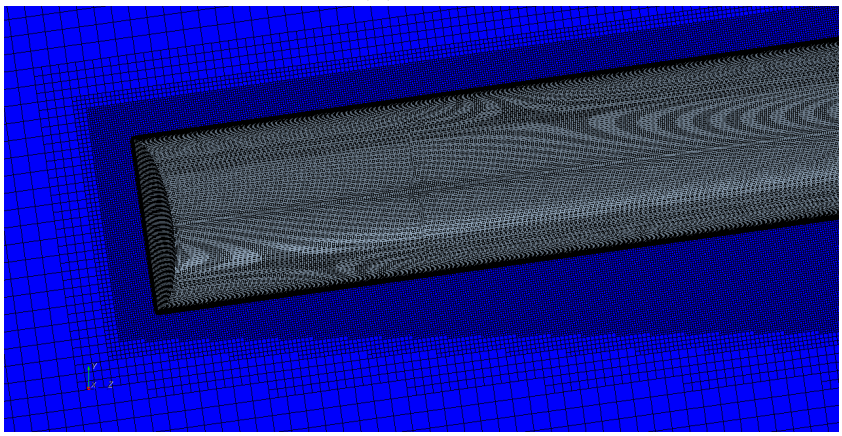

(b) 5046k

Figure 7.3: Close-up view of the mesh for on the cylinder surface and close to the cylinder.

angles from 0° to 8°). The plots show fairly good agreement with the experimental results and strip theory. The coarsest mesh tested, containing only 15 000 cells over-predicts the maximum vertical force with about 25%, but for the other meshes, the results are within ±10%. A mesh with less than 100 000 elements may be used for analyses with relatively good accuracy. For mesh 5046k, the water does not separate properly from the cylinder surface, and this is believed to be the reason for the reduction in slamming coefficient compared to mesh 1805k. This phenomena is further discussed in section 7.4.

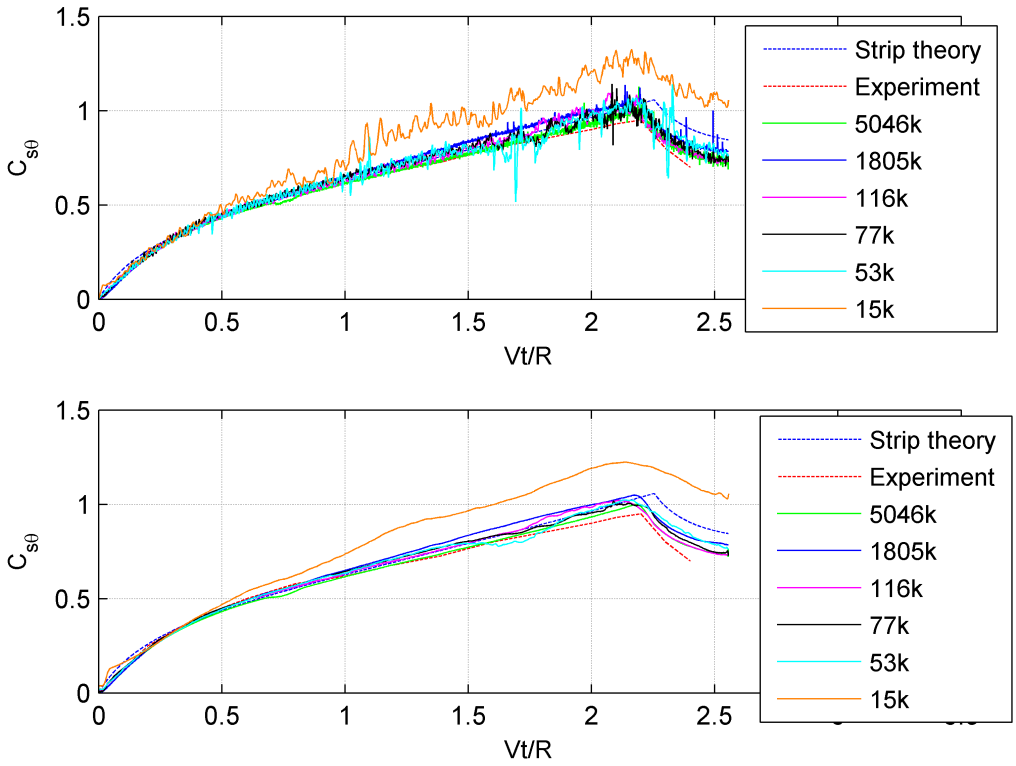

Figure 7.4: Inclined slamming $C_{s\theta}$ coefficient as a function of non-dimensional submergence Vt/R. Raw data (top) and smoothed using a moving average (bottom)

7.4 Discretization and numerical parameters

No systematic study has been performed on the influence of numerical parameters in this chapter. Instead, the recommended parameters from chapter 5 has been applied (first-order segregated flow solver and temporal discretization and second-order VOF solver). Under-relaxation factors and number of inner iterations have

been varied to achieve convergence. The number of inner iterations required for convergence is between 5 and 15 for all the simulations depending on time step size, mesh and under-relaxation factors used.

As in all CFD analyses, the setup and solution should be thoroughly inspected to determine whether the solution is physical. The main challenge for the water impact problem is found to be that water "clings" to the cylinder surface. Instead of jets forming, this results in the water closing in over the cylinder. This reduces the slamming coefficient compared to a correct simulation. No correlation between this phenomena and mesh, time step size, or convergence level has been found. The phenomena occurs for both laminar and turbulent simulations. The problem is illustrated in figure 7.5 for the 5046k mesh (3D) and the T0P15 2D mesh from chapter 5.

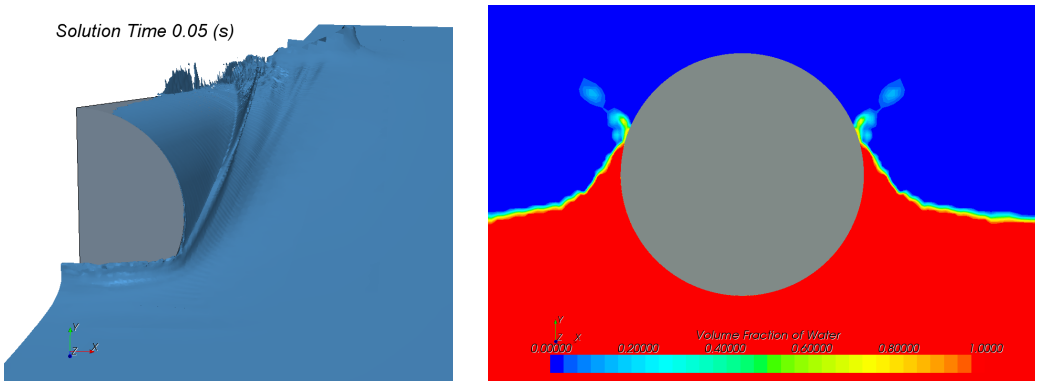

(a) 5046k 3D simulation *(b) T0P15 2D simulation*

Figure 7.5: Problems with water clinging to the cylinder surface, resulting in unphysical solutions.

7.5 Time step size

The effect of time step size has been investigated in this chapter too. Here, also time steps resulting in CFL numbers >1 have been tested. Investigating the solution at higher CFL numbers give an indication of the dissipative error introduced by the UD scheme and the stability of the solver. The mesh used for the time step size analysis is the 1805k mesh.

7.5.1 Vertical force

The inclined slamming coefficient and maximum CFL number in the domain is plotted in figure 7.6, showing that only the largest time step ($\Delta t = 5 * 10^{-5}$) results in a lower slamming coefficient. For the smaller time steps, no dependence on time step size is found. This shows that CFL numbers larger than 1 may be allowed under certain circumstances without reducing the accuracy.

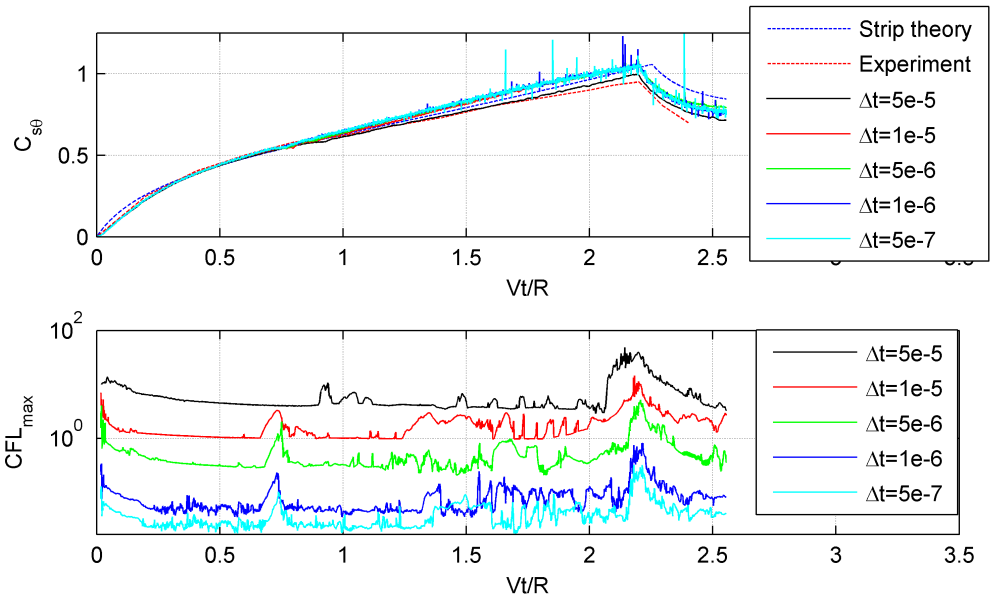

Figure 7.6: Inclined slamming coefficient and maximum CFL number in domain as a function of submergence for various time step sizes. 1805k mesh size. Logarithmic scale on the vertical axis for the CFL plot.

7.5.2 Pressure on cylinder surface

Above it was shown that a relatively coarse mesh could be used, and fairly good agreement with experimental data was shown for the total vertical hydrodynamic force even with large time steps and maximum CFL number exceeding 1. Another parameter that may be of interest is the maximum pressure on the cylinder surface, which is plotted as a function of non-dimensional submergence in figure 7.7 for various time step sizes. Studying the plot, we see that the time step size has more influence on the maximum pressure value than on the total vertical force.

The main reason for this is a "smearing" effect introduced by the larger time

steps, where the spatial pressure gradient is reduced for larger time step size. This reduces the peak value of the pressure, but the effect on total vertical force is small since the "smearing" also increases the area covered by the pressure peak.

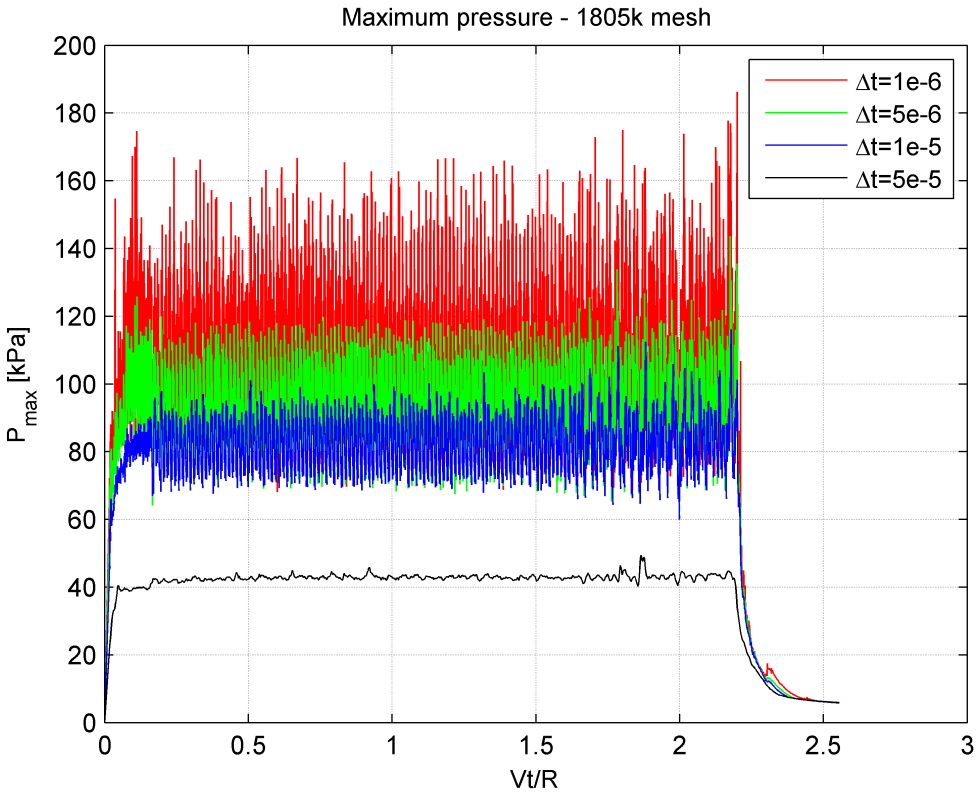

Figure 7.7: Maximum pressure on the cylinder surface as a function of non-dimensional submergence for various time step sizes.

It should also be noted how the pressure fluctuates around a mean value. The reason for this is that the mesh is not fine enough to completely resolve the pressure peak, i.e. the pressure peak covers a smaller area than one cell on the cylinder surface. The peaks in the pressure record are found when the peak coincides with the interface between two cells, and the trough occurs when the pressure peak is "hidden" within a cell. In addition, the finite time step usually means that the center of the pressure peak is not perfectly centered on the cell interface when the peaks in the plot occur, leading to different peak values for the fluctuations. This also contributes to lower average peak values for larger time steps, as large time steps reduces the probability of a peak occurring exactly at the cell boundary.

This also means that the smoothing function used extensively in this thesis

for the vertical force should not be used when studying the maximum pressure as this gives the averaged maximum pressure over a short period in time. Unless the pressure peak covers more than one cell or is maximum during the entire time covered by the smoothing function, the reported maximum pressure will be too low. Instead, the maximum pressure should be taken as the maximum value of the fluctuating pressure record.

Considering the trend of the maximum pressure record, one may see that the maximum pressure is relatively constant over a large period. This is because the pressure peak is found in the spray root propagating along the length of the cylinder, similarly as for a wedge. The relative importance of the cylindrical shape versus the angle in the third dimension can be estimated by comparing the maximum pressure coefficient C_p calculated for the cylinder with the data for wedges from Johannessen (2012) shown in table 7.2.

α [deg]	$C_{p_{\max}}$
4.0	546.3
7.5	137.7
10	80.3
15	34.8
20	18.8
25	11.0

Table 7.2: Maximum pressure coefficient C_p for wedges of deadrise angle α by Johannessen (2012)

Based on the maximum pressure plot in figure 7.7, maximum pressure on the cylinder is taken as $P_{\max} \approx 170$ kPa, giving a maximum slamming coefficient $C_{p_{\max}} \approx 50$. This is less than half the value for the 7.5° wedge analyzed by Johannessen (2012). Although considerable uncertainty exists in the maximum pressure data, this indicates a reduction in maximum pressure caused by the water also being ejected to the sides, instead of just propagating along the z-axis as it would for a wedge.

In figure 7.7 one may also see that once the entire bottom of the cylinder is below the water surface, at approximately $Vt/R = 2.2$, the maximum pressure drops significantly since there is no longer a spray root. The maximum pressure is now found over a larger area (see figure 7.8) where the smearing earlier seen is no longer influencing the maximum pressure. At this time, the vertical force is approximately 20% hydrostatic and 80% hydrodynamic.

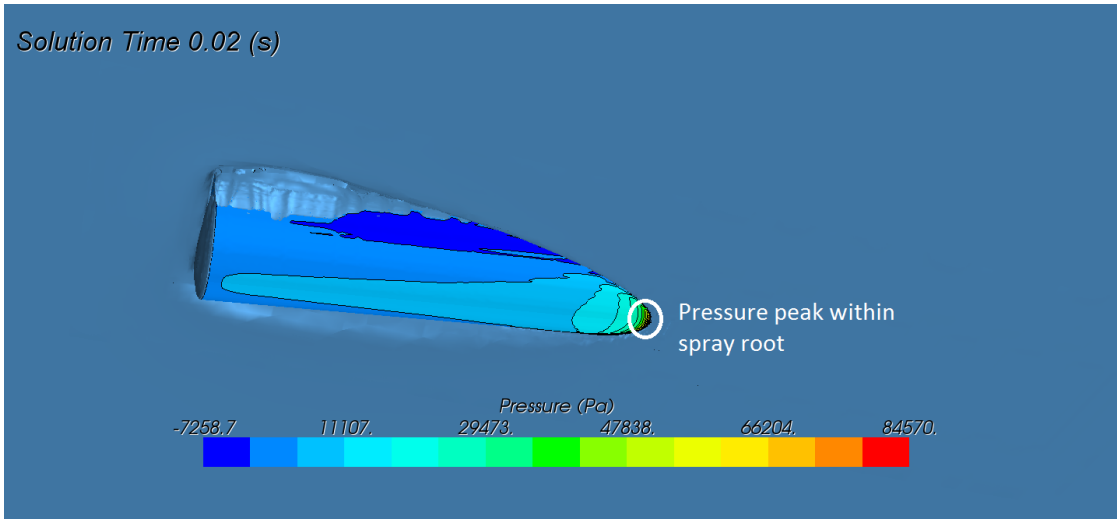

(a) $Vt/R = 1.02$, $P_{max} = 84.6\ kPa$

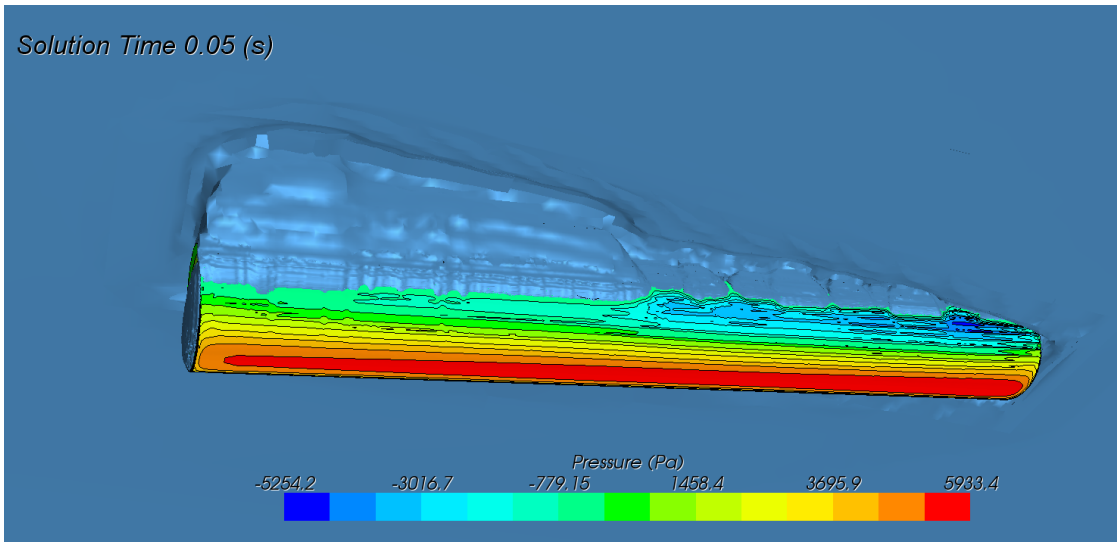

(b) $Vt/R = 2.56$, $P_{max} = 5.9\ kPa$

Figure 7.8: Pressure on cylinder surface during water entry of inclined cylinder seen from below at two different submergence.

7.6 Laminar versus turbulent flow model

In chapter 5 it was shown that for the 2D cylinder, no significant difference was found between laminar and turbulent flow model. For the 3D problem the laminar–turbulent transition along the length of the cylinder may also influence the results, and the dependence on flow model has therefore been investigated. The turbulence model applied is the same as used in chapter 5, i.e. a shear driven two-layer $k-\epsilon$ RANS model with "Two-Layer All y+" wall treatment. Figure 7.9 shows the total vertical force on the cylinder (pressure + shear), vertical shear force contribution and maximum pressure on the cylinder versus non-dimensional submergence for the 1805k mesh using time steps $\Delta t = 5 * 10^{-6}$ s. It should be noted that the smooth plot of the surface pressure in figure 7.9 is not the maximum pressure on the surface, but rather an average of the maximum pressure reported over a short time period as discussed in section 7.5.2.

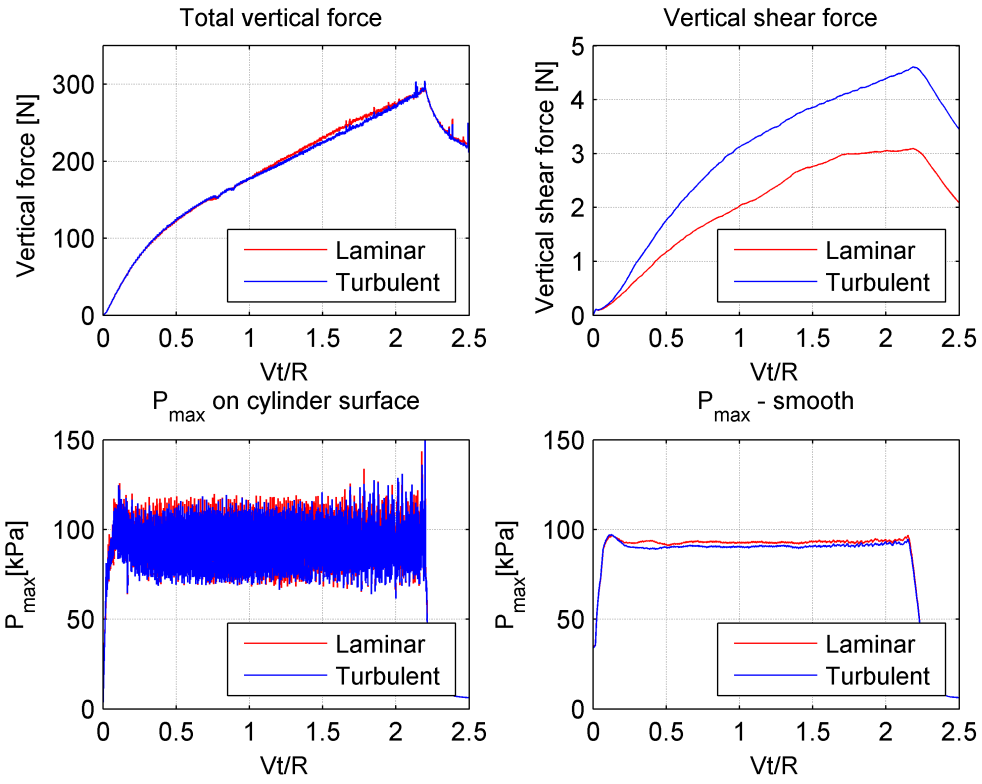

Figure 7.9: Total vertical force (shear + pressure forces), vertical component of the shear force on the cylinder, and maximum pressure on the cylinder surface (raw data and smoothed) for an inclined cylinder. 1805k mesh and $\Delta t = 5 * 10^{-6}$

From the plot, the same behavior as for the 2D analysis is seen, with larger vertical shear force for the turbulent model. But since the shear force contribution to the total force is small compared to the pressure force, the slight decrease in vertical pressure force using turbulent model versus laminar outweighs the shear force increase, and the result is a decrease in total vertical force. The difference is small, indicating that laminar flow model may be used for the 3D analyses. The laminar model gives an increase in pressure of 0-4% depending on submergence compared to the turbulent simulation. Johannessen (2012), who studied the water impact for a wedge, reported that this difference in his simulations was about 3%.

To determine if this behavior is dependent on time step size, the turbulent simulation has also been performed for time steps $\Delta t = 1 * 10^{-5}$ s, $5 * 10^{-6}$ s, $1 * 10^{-6}$ s, and $5 * 10^{-7}$ s. The calculated $C_{s\theta}$ from these simulations are plotted as a function of non-dimensional submergence together with maximum CFL numbers in figure 7.10, showing the same behavior as for laminar flow model, with negligible dependence on time step size for the vertical hydrodynamic force.

7.7 Conclusion

In this chapter, the water entry of an inclined cylinder resembling the experimental work by Campbell and Weynberg (1980) has been simulated. Studying the maximum pressure on the cylinder revealed a dependence on time step size, as large time steps introduced a "smearing" that reduces the peak the pressure. Because this "smearing" increases the area of the pressure peak, this does not result in errors for the global force analysis, and good agreement was found with experimental data and strip theory for the inclined slamming coefficient.

The maximum pressure on the cylinder surface is found in the center of the spray root propagating along the longitudinal axis of the cylinder. Considering the maximum pressure compared to a wedge it was found that the circular cross-section reduces the pressure significantly compared to an equivalent wedge.

The mesh size analysis revealed that a coarse mesh may be used for engineering purposes and that the angle between the water and the cylinder reduces the numerical problems at the bottom of the cylinder. It should be noted that there are still problems with obtaining physical results for certain meshes, with water "clinging" to the cylinder surface reducing the hydrodynamic force on the cylinder. The solution should therefore be carefully inspected after each simulation to ensure that the results are correct if highly accurate results are needed.

It was also shown that a laminar flow model predicts the loads on the cylinder

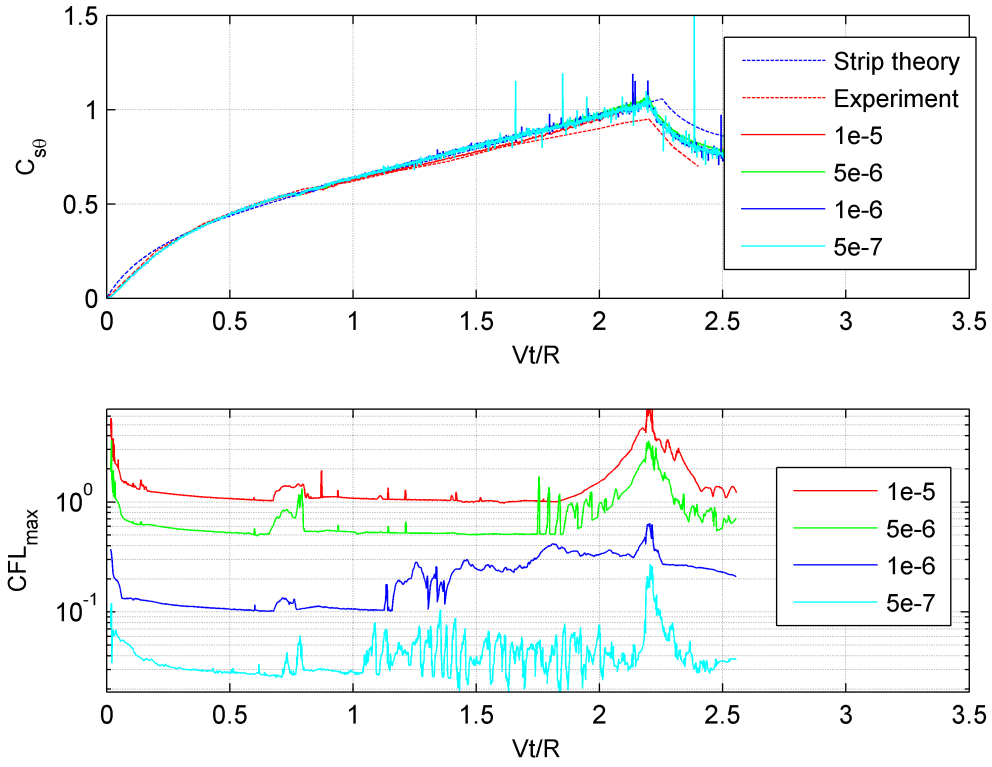

Figure 7.10: Inclined slamming coefficient and maximum CFL number in domain as a function of submergence for various time step sizes. 1805k mesh size and turbulent flow model. Logarithmic scale on the vertical axis for the CFL plot.

well. Choosing laminar flow model reduces the shear forces acting on the cylinder, but an increase of 0-4% for the pressure forces resulted in a small increase in total vertical force for a laminar flow model compared to turbulent flow.

The vertical force on the cylinder calculated by STAR-CCM+ is somewhat higher than the experimental results by Campbell and Weynberg (1980), but is considered to be within the range of possible errors in the experiments. Whether the CFD results or experimental data are most correct is not known, and more reliable experimental data are needed if the accuracy of the simulation is to be determined.

8 Conclusions

In this thesis, the potential of the CFD-software STAR-CCM+ to model water impact of both 2D and 3D cylinders have been tested for constant-velocity and free body motion cases. Results are compared with experimental, empirical and numerical results, using both laminar and turbulent flow models.

Studying numerical parameters and model setup, it has been found that second-order discretization is needed for the VOF solver.[8.1] First-order segregated flow convection scheme and time discretization scheme may be used without any significant change in calculated force. The advantage of using these first-order schemes is an increase in stability compared to higher-order schemes.

No dependence on time step size is found as long as the CFL number is less than 0.5 on the free surface and less than 1 everywhere else in the domain. For the 3D simulations, it has been found that CFL numbers greater than 1 can be allowed in certain areas with negligible effect on the vertical force. However, increasing the time step size reduces the maximum pressure on the cylinder surface due to a "smearing" of the pressure peak in the spray root.

It has also been found that a turbulent flow model increases shear forces on the cylinder surface and gives a slight reduction in pressure force compared to a laminar flow model. Pressure forces dominate the vertical force, and choosing the laminar flow model results in 0-4% higher slamming coefficient compared to the turbulent model.

It was also shown that for the problems analyzed in this thesis, compressibility of water matters for less than 1 μs, and is therefore of little practical interest. Also, in VOF-type CFD, the free surface is not perfectly sharp. The error introduced by this vastly exceeds the effects of compressibility, hence incompressible fluid models may be used for the problems studied in this thesis.

Through the work presented in this thesis, it has been shown that STAR-CCM+ can be used to simulate water entry of cylinders in two and three dimensions. Since circular cylinders are considered one of the most difficult geometry for numerical codes to calculate water impact loads on, this indicates that the STAR-CCM+ can be used for calculating such loads on most geometries.

For simple problems such as 2D cylinders on a flat free surface, it has been found that the impact force can be calculated using the empirical line by Campbell and

[8.1] The VOF solver calculates convection of the VOF scalar defining the fraction of water and air in each cell

Weynberg (1980), and in most cases performing CFD simulations on such problems is a waste of time. However, the main advantage of CFD is the ability to simulate complex flows and geometries. Based on the work presented, this is believed to be valid for water impact problems too, justifying the use of STAR-CCM+ as an attractive alternative to model tests for such simulations including complex geometries and flow patterns.

9 Further work

This thesis has shown that the CD-adapco developed CFD-software STAR-CCM+ accurately predicts the vertical forces on cylindrical bodies. Also the motion of a free-falling cylinder has been well-predicted showing the software's ability to simulate fluid-structure interaction and body motion. For the simple problems tested in this thesis, empirical formulas are available and show comparable results to those from STAR-CCM+. This means that the main advantage for CFD is to model more complicated structures, such as a rack of cylinders where the flow around one cylinder influences the inflow of its neighbors.

During the work on this thesis, it has been found that the experiments available for validation are relatively uncertain with many possible sources of errors. This indicates a need for new experiments. To reduce possible sources of errors, free-fall drop tests equivalent to the setup by Greenhow and Lin (1983) may be used. By using high-speed cameras, both the free surface deformation and the penetration depth of the cylinder can be found at each time instant. The drop height, weight of the cylinder, impact angle etc. may be varied. Based on this, accelerations of the cylinder can be found and used for calculating the vertical forces on the cylinder. End effects of the cylinder can also be studied, comparing cylinders of different length with and without end plates, and geometries such as tubular joints and more complex structures are also of interest. Following this experiment, the results should be compared to results from STAR-CCM+, including penetration depth, accelerations, forces etc.

Based on the findings in this thesis, a natural next step is to use STAR-CCM+ for calculating water impact loads on more complex structures. It was shown in chapter 7 that a mesh with only 53 000 elements give reasonable results for an inclined cylinder. For structures such as a subsea template, the required number of cells is believed to be between one and ten million, depending on the accuracy needed. At the moment, such simulations are possible to perform on a relatively small computer cluster, for which the computational time would be in the range of a few hours to about two days. This shows a practical use of CFD software of great interest to the industry. To simulate lowering of a subsea template, the geometry of the structure is needed. As long a this geometry as available from SolidWorks, Rhino3D or other CAD tools supported by STAR-CCM+, the geometry can be imported and used as a basis for the mesh. The meshing and convergence studies are the most time consuming part of such a simulation, and depends heavily on the experience level of the user. Once this model has been set up, waves, mass of structure, center of gravity, lowering velocity etc. can easily be varied, making it

possible to perform a comprehensive test program in relatively short time. Such simulations can also be compared to model or full scale tests.

Other examples of interesting problems that can be studied using CFD is wave impact on risers, guide tubes or structural members in the splash zone, and simulating water-on-deck problems for offshore platforms.

The possibilities for CFD simulations are almost unlimited, and it is believed that the use of CFD will escalate in the coming years. With an increase in computational power and more efficient codes, this will lead to more complex analyses and longer time series being studied, allowing for more realistic and accurate simulations than what have been possible until now.

References

Arhan, M. and Deleuil, G. (1978). Experimental study of the impact of horizontal cylinders on a water surface. *OTC No. 3107 - Offshore Technology Conference*.

Arman, J. and Cointe, R. (1987). Hydrodynamic impact analysis of a cylinder. *Proc. Fifth Int. Offshore Mech. and Arctic Engng. Symp*, pages 609–634.

Campbell, T., Wellicome, J., and Weynberg, P. (1977). An investigation into wave slamminng loads on cylinders (OSFLAG 2A). *Wolfson Marine Craft Unit Report No. 317 - University of Southampton*.

Campbell, T. and Weynberg, P. (1980). Measurement of parameters affecting slamming - final report. *Wolfson Marine Craft Unit Report No. 440 - University of Southampton*.

CD-adapco (2012). *STAR-CCM+ v7.06 User Manual*. CD-Adapco.

DNV (2010). *Environmental conditions and environmental loads - DNV-RP-C205*. Det Norske Veritas.

Faltinsen, O. and Chezhian, M. (2005). A generalized Wagner method for three-dimensional slamming. *J. Ship Res.*, 49(4):279–287.

Faltinsen, O., Kjærland, O., Nøttvedt, A., and Vinje, T. (1977). Water impact loads and dynamic response of horizontal circular cylinders in offshore structures. *OTC No. 2741 - Offshore Technology Conference*, 1:119–126.

Ferziger, J. and Perič, M. (2003). *Computational Methods for Fluid Dynamics - 3rd edition*. Springer.

Fletcher, C. (1991). *Computational Techniques for Fluid Dynamics - Volume 1, Second Edition*. Springer.

Greenhow, M. and Lin, W. (1983). Nonlinear free surface effects: Experiments and theory. *Report No. 83-19 Department of Ocean Engineering, MIT*.

Hagiwara, K. and Yuhara, T. (1976). Fundamental study of wave impacts loads on ship bow. *Selected papers from the J. Soc. Nav. Arch. of Japan*, 14:73 – 85.

Johannessen, S. (2012). Use of CFD to study hydrodynamic loads on free-fall lifeboats in the impact phase. Master's thesis, Norwegian University of Science and Technology - Department of Marine Technology.

Kopperstad, A. (2011). Hydrodynamiske beregninger med bølgeoverflater. Master's thesis, Norwegian University of Science and Technology - Department of Marine Technology.

Korobkin, A. (2004). Analytical models of water impact. *European Journal of Applied Mathematics*, 15:821–838.

Korobkin, A. and Pukhnachov, V. (1988). Initial stage of water impact. *Ann. Rev. Fluid. Mech.*, 20:159–185.

Larsen, E. (2012). Higher order loads for steep waves. *Project thesis - Norwegian University of Science and Technology - Department of Marine Technology.*

Logvinovich, G. (1969). *Gidrodinamika tečenij so svobodnymi granicami (Hydrodynamics of free-boundary flows).* Naukova dumka.

MARINTEK (2004). *Slam2d User Manual.* MARINTEK.

MathWorks (2012). *MATLAB R2012b User Manual.* MathWorks.

Mei, X., Liu, Y., and Yue, D. (1999). On the water impact of general two-dimensional sections. *Appl. Ocean Res.*, 21:1–15.

Miao, G. (1989). *Hydrodynamic Forces and Dynamic Responses of Circular Cylinders in Wave Zones.* PhD thesis, Norwegian Institute of Technology, NTH - Department of Marine Hydrodynamics.

Mørch, H., Enger, S., Peric, and Schreck, E. (2008). Simulation of lifeboat launching under stort conditions. *6th International Conference on CFD in Oil & Gas, Metallurgical and Process Industries, Trondheim, Norway, 10-12 June 2008.*

Patankar, S. and Spalding, D. (1972). A calculation procedure for heat, mass and momentrum transfer in three-dimensional parabolic flows. *Int. J. Heat Mass Transfer*, 15(10):1878–1806.

Ransau, S. (2008). *Lecture notes for the course: Numerical Methods in Marine Hydrodynamics.* Norwegian University of Science and Technology, Department of Marine Technology.

Sollied (1976). *Beregning av krefter på stag ved slagaktige påkjenninger.* Student project, Division of Ship Hydrodynamics, NTH, Trondheim.

Sten, R. (2012). *Dynamic simulation of deep water drilling risers with heave compensating system.* PhD thesis, Norwegian University of Science and Technology, NTNU - Department of Marine Technology.

Sun, H. (2007). *A boundary element method applied to strongly nonlinear wave-body interaction problem*. PhD thesis, Norwegian University of Science and Technology, NTNU - Department of Marine Technology.

Thies, J. and Wubs, F. (2011). Design of a parallel hybrid direct/iterative solver for CFD problems. *7th IEEE International Conference on eScience, Stockholm, Sweden, 5-8 December 2011*.

Tsimis, B. (2013). Email correspondances spring 2013.

Van Nuffel, D., Vepa, K., De Baere, I., Degrieck, J., Derouck, J., and Van Paepegem, W. (2011). Parameters affecting the pressure measurement on the surface of a rigid cylindrical body during water slamming impact. *International Workshop on Water Waves and Floating Bodies*, 26.

Vandamme, J., Zou, Q., and Reeve, D. (2011). Modeling floating object entry and exit using smoothed particle hydrodynamics. *J. Waterway, Port, Coastal, Ocean Eng.*, 137(5):213–224.

Vestbøstad, T. (2009). *A numerical study of Wave-in-deck Impact using a Two-dimensional Constrained Interpolation Profile Method*. PhD thesis, Norwegian University of Science and Technology, NTNU - Department of Marine Technology.

von Karman, T. (1929). The impact on seaplane floats during landing. *NACA TN321*.

Vorus, W. (1996). A flat cylinder theory for vessel impact and steady planing resistance. *J. Ship Res.*, 40:89–106.

Wagner, H. (1932). Über stoß- und gleitvorgänge an der oberfläche von flüssigkeiten. *ZAMM - Journal of Applied Mathematics and Mechanics / Zeitschrift für Angewandte Mathematik und Mechanik*, 12(4):193–215.

Zhao, R. and Faltinsen, O. (1993). Water entry of two-dimensional bodies. *J. Fluid Mech.*, 246:593–612.

Zhao, R., Faltinsen, O., and Aarsnes, J. (1996). Water entry of arbitrary two-dimensional sections with and without flow separation. *Twenty-First Symposium on Naval Hydrodynamics*, pages 408–423.

Zhu, X. (2006). *Application of the CIP Method to Strongly Nonlinear Wave-Body Interaction Problems*. PhD thesis, Norwegian University of Science and Technology, NTNU - Department of Marine Technology.

A Moving average plot smoothing

To increase visibility of the plots in this thesis, a moving average smoothing function has been applied during postprocessing. This smoothing function is a standard MATLAB function called *smooth*, and can be summarized as follows (MathWorks, 2012):

Let $\mathbf{yy}$ be a vector containing the smoothed average of the vector $\mathbf{y}$ using a span width of 5 elements, the values of $\mathbf{yy}$ are:

$$\mathbf{yy}(1) = \mathbf{y}(1) \tag{A.1a}$$

$$\mathbf{yy}(2) = (\mathbf{y}(1) + \mathbf{y}(2) + \mathbf{y}(3))/3 \tag{A.1b}$$

$$\mathbf{yy}(3) = (\mathbf{y}(1) + \mathbf{y}(2) + \mathbf{y}(3) + \mathbf{y}(4) + \mathbf{y}(5))/5 \tag{A.1c}$$

$$\mathbf{yy}(4) = (\mathbf{y}(2) + \mathbf{y}(3) + \mathbf{y}(4) + \mathbf{y}(5) + \mathbf{y}(6))/5 \tag{A.1d}$$

$$\dots$$

In this thesis, the span width has been varied to smooth the plot without loosing significant effects. Typical smoothing span width is from 11 to 251 (only uneven numbers can be used).

B Strip theory of inclined impact

Consider a cylinder slamming into water with an impact angle θ normal to the water surface. Assume that the vertical force component on a strip element of the cylinder of width dx can be calculated and is unaffected by the axial velocity component ($V \sin\theta \approx 0$). For simplicity, assume that the vertical velocity is constant, all strips are of same thickness, and θ is small, so that $V \cos\theta \approx V$.

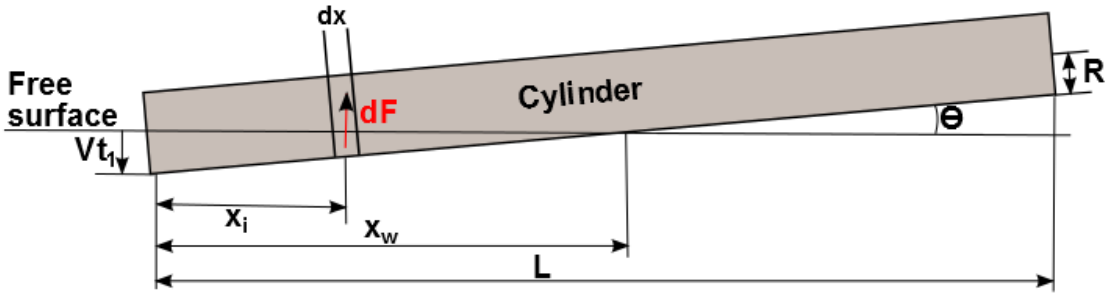

Figure B.1: Inclined water impact definitions and geometry

Let x_w be the wetted length of the cylinder, and t_1 the time after the bottom of the cylinder first hits the water surface. ($x_l = 0$ when $t_1 = 0$). Let the first strip be at the lower end of the cylinder, and x_i be the horizontal distance from the lower end of the cylinder to the center of strip i. See figure B.1. The non-dimensional submergence of the lower end of the cylinder is then $S = Vt_l/R$. The vertical slamming force acting on strip i is:

$$dF_i = \rho V^2 C_s(t_i) R dx \tag{B.1}$$

where t_i is the local time from start of impact on element i;

$$t_i = t_1 - \frac{x_i}{V} \tan\theta \tag{B.2}$$

Inserting the slamming coefficient proposed by Campbell and Weynberg (1980) for each strip,

$$C_s(t_i) = \frac{5.15}{1 + 9.5Vt_i/R} + 0.275Vt_i/R \tag{B.3}$$

gives the following vertical slamming force on the cylinder:

$$F = \rho V^2 R \sum_{i=1}^{n} [\frac{5.15}{1 + 9.5 V t_i / R} + 0.275 V t_i / R] \tag{B.4}$$

where n is number of strips between x_1 and x_w: Normalizing with respect to V and L, the average slamming coefficient for inclined impact is:

$$C_{s\theta} = \frac{F}{\rho V^2 R L} = \frac{1}{L} \sum_{i=1}^{n} [\frac{5.15}{1 + 9.5 V t_i / R} + 0.275 V t_i / R] dx \tag{B.5}$$

If instead the slamming coefficient presented by Miao (1989) is used, the following inclined impact slamming coefficient is obtained:

$$C_{s\theta} = \frac{F}{\rho V^2 R L} = \frac{1}{L} \sum_{i=1}^{n} [6.1 e^{-6.2 V t / R} + 0.4] dx \tag{B.6}$$